Title
Experimental Beam Studies of Plasma-generated Species Interaction with Polymeric Materials and Biomolecules

Author
Chung, Ting-Ying

Publication Date
2012

Peer reviewed|Thesis/dissertation

Experimental Beam Studies of Plasma-generated Species Interaction with Polymeric Materials and Biomolecules

by

Ting-Ying Chung

A dissertation submitted in partial satisfaction of the

requirements for the degree of

Doctor of Philosophy

in

Chemical Engineering

in the

Graduate Division

of the

University of California, Berkeley

Committee in charge:

Professor David B. Graves, Chair
Professor Jeffrey A. Reimer
Professor Rachel A. Segalman
Professor Michael A. Lieberman

Fall 2012

Experimental Beam Studies of Plasma-generated Species Interaction with Polymeric Materials and Biomolecules

by

Ting-Ying Chung

Abstract

Experimental Beam Studies of Plasma-generated Species Interaction with Polymeric Materials and Biomolecules

by

Ting-Ying Chung

Doctor of Philosophy in Chemical Engineering

University of California, Berkeley

Professor David B. Graves, Chair

Low temperature plasma-based processes are used extensively in many modern technologies. It is thus very important to understand plasma and surface interactions in order to improve plasma processes and design of functional materials. Applying a high vacuum beam system, this dissertation studies the fundamental mechanisms of plasma species-induced modification of materials for two critical applications: manufacturing of semiconductor devices and surface deactivation of infectious biomolecules.

Manufacturing of integrated circuits relies on well-controlled film patterning technology. This is currently achieved by photolithography followed with plasma etch. While critical dimension control is acknowledged to be a major challenge for future miniaturization of transistors and other functionalities, degradation and roughening of methacrylate-based 193 nm photoresist (PR) during plasma etch processes result in poor pattern transfer and decreased device performance. The first part of this dissertation addresses the effects of ion bombardment, vacuum ultraviolet (VUV) irradiation, electron exposure, and moderate substrate heating in 193 nm PR surface roughening.

150 eV Ar ion bombardment results in physical sputtering and formation of a carbon-rich layer at the PR surface. The thickness of this surface layer is about 2 nm. This ion-modified layer is expected to bear an intrinsic compressive stress, roughly a few GPa. In contrast, 147 nm VUV irradiation and 1 keV electron exposure both modify the PR film up to the penetration depth, ~100 nm. Enhanced PR surface roughening is only observed when a simultaneous exposure provides a combination of an ion-modified surface layer on top of a scissioned/softened bulk layer, either resulting from VUV irradiation or low fluence electron (< 1 mC·cm^{-2}) exposure. 2-methyl-2-adamantyl methacrylate, the leaving group of 193 nm PR, is especially sensitive to VUV exposure. The adamantyl leaving group is shown to be one of the main photolysis products. The loss and detachment of bulky adamantyl groups are highly correlated to the surface roughening of processed PR. These phenomena can be qualitatively explained by a bi-layer wrinkling mechanism. The results demonstrate that PR structure can couple to plasma etch processes and strongly alter the post-etch morphology.

The second part of this dissertation is motivated by the insufficiency of conventional sterilization methods against bacterial and protein residues. Such residues on the surface of medical instruments increase the risk of healthcare-associated infections for patients. Low temperature plasmas are promising alternative sterilization/deactivation methods. A thorough understanding of plasma and biological target interactions is required to align applications with scientific principles. Lipid A, the immune-stimulating region of lipopolysaccharide, is chosen to be the model molecule. Using a surface-sensitive human whole blood-based assay, the present study shows that VUV photons, oxygen and deuterium radicals can cause deactivation of lipid A film through different mechanisms. Similar to 193 nm PR studies, VUV photons are able to induce bulk modification of lipid A film up to the penetration depth of photons, ~200 nm. VUV photons primarily cleave ester linkages and lead to desorption of aliphatic chains. Loss of phosphate groups and the glucosamine backbone is also observed. In contrast, radicals react at the lipid A film surface, form volatile products, and lead to slow chemical etching. The etch yield of radicals is one order of magnitude lower than that caused by VUV-induced photolysis. In spite of its low etch yield, radical exposure strongly modifies lipid A film surface. This work contributes to the fundamental understanding of plasma interaction with biomolecules. The principle of this study is also relevant to the broader scope of plasma applications on biological targets, including cells and tissues, in the rapidly growing field of plasma medicine.

To my parents and Yi-Fang

Table of Content

List of Figures

Acknowledgements

I can only find myself extremely grateful.

First and foremost, I would like to thank my advisor, Prof. David Graves for his support, guidance, and encouragement in the past few years. Dave gives me the freedom to explore, saves me from my mental blocks, and always shows great confidence and interests in my results, whether they are good, bad, or unexpected. His profound knowledge and enthusiasm in learning new disciplines set the highest standard for a great scholar. I am extremely fortunate to study with Dave at Berkeley.

There are so many people who have helped me steer through this adventure. I would like to thank Dr. Dustin Nest for teaching me everything about the beam system and working with me during my first 2 years in Graves lab. His delightful personality made the learning and training so much fun. I would also like to thank Dr. John Coburn, Dr. Harold Winters, and Dr. David Fraser for sharing their experience and providing suggestions in experiments. Thanks to Dr. Pei-Lin Cheng for teaching me the fundamentals of biological experiments and helping me with my first successful human whole blood test! I would also like to thank Dr. Tony Iavarone, Dr. Suet Yi Liu, and Dr. Musahid Ahmed for assisting mass spectrometry measurements. These results are of critical importance for my work. Friends throughout the college of chemistry are extremely generous. I would like to thank Dr. Jeremy Niskala, Alan Yiu, Kierston Shill, and other members of Clark, Segalman, Balsara, and Francis group for sharing research equipment with me. Without their help, this work would not be possible. I am also grateful for the effort from Prof. Gottlieb Oehrlein, Prof. Joonil Seog, Prof. Jhih-Wei Chu, Dr. Eric Hudson, Dr. Robert Bruce, Dr. Florian Weilnboeck, Elliot Bartis, Dr. Deyan Wang, and Dr. Mingqi Li, my collaborators over the years. Thank Prof. Jeffrey Reimer, Prof. Rachel Segalman, and Prof. Michael Lieberman for being my dissertation committee members and their input in completing this dissertation.

The past and present Graves group members have made the time I spent two floors underground unforgettable. Thanks to Dr. Monica Titus and Joe Lee for proof reading everything for me! I cannot possibly list friends I met in the Bay Area and old friends back in Taiwan. No words can be used to express my appreciation for having each and every one of you being a part of my ongoing journey.

Last, but not least, I would like to thank my parents for their enormous support and love. I certainly miss home here in a foreign country, and I can only keep my head up during those hard times because I know they will always be there for me. Finally, I would like to dedicate my special thanks to Yi-Fang for her love and encouragement. I am truly blessed to have her in my life.

Chapter 1
Introduction

1.1 Plasma-surface Interactions

Low temperature plasmas are used extensively in many modern technologies, including etching, plasma-enhanced chemical vapor deposition, and surface treatment, to name a few. Because of the wide applications, it is extremely important to understand plasma and surface interactions in order to improve plasma processes and design of functional materials.

The plasma addressed in this dissertation is an electrically driven, weakly ionized discharge.[1] The applied power is used to preferentially energize mobile electrons. Electrons bearing enough energy can ionize or dissociate parent molecules to create ions, radicals, and excited species. These excited states can return to lower energy states by emitting photons. Plasmas can thus emit photons with various wavelengths, determined by the plasma gas chemistry. The energetic electrons are heated to well above room temperature (T_e ~1-10 eV) and are not in thermal equilibrium with the ions, radicals, or background gases. Those heavy species exchange energy more efficiently through collisions and thus remain at near room temperature. The degree of ionization in a plasma is defined as

$$x_{iz} = \frac{n_i}{n_g + n_i} \tag{1.1}$$

where n_g is the neutral gas density and n_i is the ion number density. x_{iz} is much less than 1 for a weakly ionized plasma.

A plasma is quasi-neutral, namely $n_i \sim n_e$ (n_e is the electron number density), except at the plasma-surface interfaces in what is known as the "sheath". Within the sheath, mobile electrons are rapidly lost to the walls initially and a net positive charge density is built up. This leads to a positive potential profile (Φ) within the plasma bulk that drops rapidly to zero near walls. The sheath acts as a potential barrier to reflect electrons traveling to the walls back to the plasma bulk. On the other hand, ions accelerate through the sheath and impact the surface with the acquired energy. The ion energy can be further controlled by an applied bias on the surface. Lastly, neutral species such as radicals diffuse towards the surface. The unique processing capability of

plasmas comes from these energetic and reactive species, which impact the material simultaneously.

This dissertation will address two applications of low temperature plasmas. The first focus is the roughening of 193 nm photoresist material in plasma etch processes, one of the issues challenging the semiconductor industry to further scale down the size of devices. The second focus is plasma deactivation of virulent biomolecules for infection control in healthcare facilities.

1.2 The Manufacturing of Integrated Circuits

In the past 50 years, the semiconductor industry has achieved a rapid pace of improvement. The continuous scaling of transistor size has followed Moore's law, named after Intel's co-founder Gordon E. Moore's observation: the number of transistors on a chip will double approximately every two years.[2] Last year (2011), Intel announced its new generation of 22 nm 3-D Tri-Gate transistor technology, which is the first 22 nm node technology entering high volume manufacturing. It is also the first time in history that the silicon channel of a transistor is raised to the third dimension. The gate electrode is wrapped around the channel to provide a better control and lead to a steep sub-threshold slope that reduces leakage current and threshold voltage. The minimum feature size changes from the gate width to the channel fin width, ~8 nm.[3] More importantly, the miniaturization of transistors and other functionalities achieves higher performance with a lower cost per function and lower power consumption per transistor. This enables broader applications, including high-end servers for cloud computing, personal desktops, laptops, tablets, and mobile devices.

Manufacturing of integrated circuits relies on well-controlled film patterning technology. This is currently achieved by photolithography followed with plasma etch. A summary is illustrated in Figure 1.1. For example, to make a trench into a dielectric film, a thin layer of organic photoresist (PR) is coated on the film. Radiation is projected through a mask and changes the chemical structure of exposed PR. Exposed areas are chemically altered by radiation and then developed by an aqueous base solution. Following development, anisotropic etching is carried out with plasma processing. During plasma etch, the pristine PR polymer acts as a mask to protect the material underneath. Different gas chemistries have to be carefully chosen to obtain a desired selectivity of film over PR. Finally, the remaining PR is removed. Photolithography and plasma etch are indispensable steps in device manufacturing because they are required for every mask level.

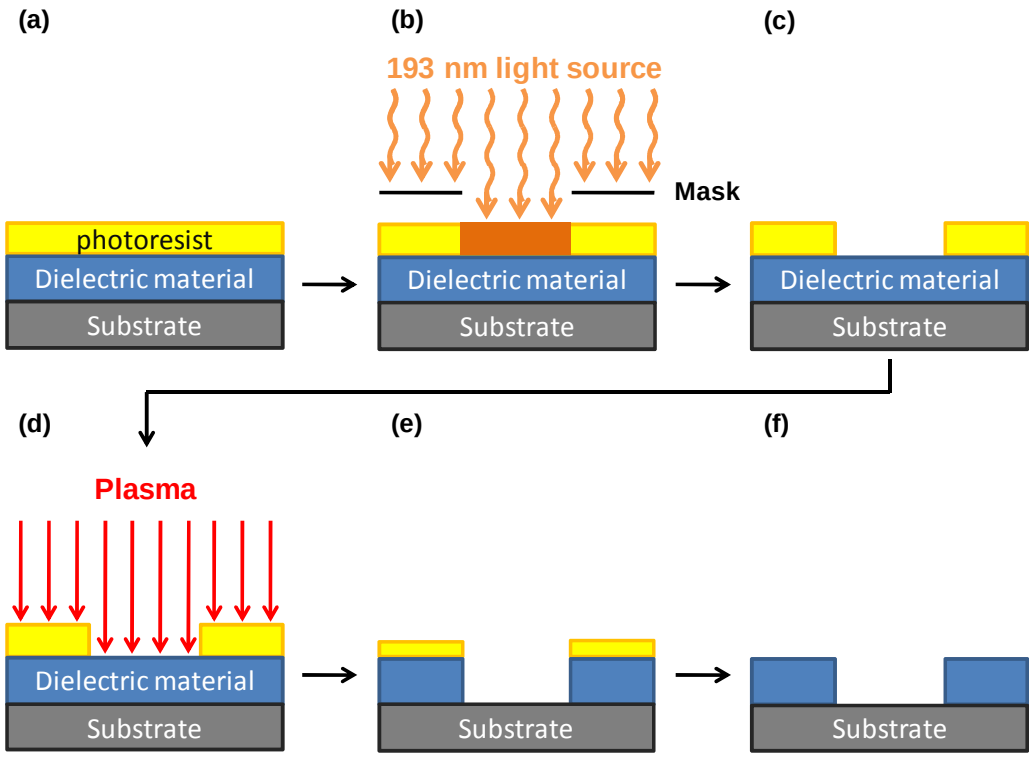

Figure 1.1 Pattern transfer using photolithography and plasma etch. (a) Coating of photoresist. (b) Light exposure through a mask. (c) Photoresist development. (d) Anisotropic etching using plasma processing. (e) Removal of photoresist. (f) A trench patterned into the dielectric film.

1.2.1 Photolithography

Key advancements in photolithography, mainly the light source and PR materials, have allowed the semiconductor industry to fabricate devices now approaching the few nanometers scale. Currently, 193 nm immersion lithography and 193 nm PR are the work horses for the industry.

The following scaling equation describes the resolution of an optical projection imaging system, where there is a 4:1 or 5:1 optical reduction of the mask features to imaging feature sizes:[4]

$$W = k_1 \frac{\lambda}{\sin\theta} = k_1 \frac{\lambda_0}{n \sin\theta} = k_1 \frac{\lambda_0}{NA} \tag{1.2}$$

where W is the resolution given in the size of a feature or a half pitch, λ is the wavelength of light in the medium of concern, θ is the aperture angle, k_1 is a proportional constant ranging from 0.25 to 1, depending on overall process capability, λ_0 is the wavelength of light in vacuum, n is the refractive index of the medium between the last element of the imaging lens and the surface of the PR, and NA is the numerical aperture of the imaging lens.

From the aspect of optical imaging, one can either decrease the wavelength of incident light or increase the numerical aperture to achieve a smaller feature size. The reduction of exposure wavelength was accomplished by changing the light source from the mercury arc lamp (for 436 nm g-line and 365 nm i-line), the KrF excimer laser (for 248 nm), to the current 193 nm ArF excimer laser.[5] The attempted transition to 157 nm F_2 excimer laser failed due to the stringent optical requirement for a CaF_2 projection lens. On the other hand, liquid immersion lithography by applying a high refractive index medium, such as ultrapure water (refractive index = 1.436 at 193 nm) between the last lens element and the PR surface, reduces the effective wavelength to 193/1.436 ~134 nm in ultrapure water. Figure 1.2 illustrates the schematic of an immersion projection system.

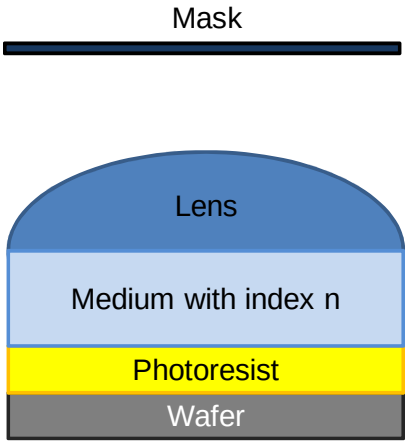

Figure 1.2 Schematic of an immersion projection system.

Furthermore, compared to a dry system (refractive index of air = 1), an immersion system also improves the depth of focus (DOF), another figure of merit of photolithography. The DOF scaling equation is given here:[4]

$$DOF = k_3 \frac{\lambda}{\sin^2\left(\frac{\theta}{2}\right)} = k_3 \frac{n\lambda_0}{NHA^2} \tag{1.3}$$

where *NHA* is the numerical half aperture $n \cdot \sin(\theta/2)$ and k_3 is the DOF scaling coefficient. An increase of the refractive index of the medium also increases the DOF of an immersion system over a dry system.

Along with the change of exposure wavelength, a major material development has been made in PRs. PR materials must fulfill stringent requirements, such as high sensitivity, high transparency (low absorption) at exposure wavelength, and good resistance to plasma etch processes. A transition of exposure wavelength often requires a transition in PR chemical structure, from diazonaphthoquinone (DNQ)-based PRs for g-line/i-line, polystyrene-based PRs for 248 nm to methacrylate-based PRs for current 193 nm exposure. [6]

The chemical amplification mechanism has been the pivotal foundation and implemented in both 248 and 193 nm PRs to increase their sensitivity. Chemical amplification is accomplished by employing the photoacid generator (PAG), such as triphenyl sulfonium perfluorobutylsulfonate, which produces strong acids upon irradiation that promote catalytic or chain reaction. Details of chemical amplification can be found in several review articles and book sections.[6, 7] One of the main chemical amplification mechanisms is deprotection of acid-labile protecting groups by photogenerated acids. This creates base-soluble acidic functionalities such as phenols and carboxylic acids and increases the solubility of polymer in an aqueous base developer. 2-methyl-2-adamantyl methacrylate is a commonly used leaving group in 193 nm PR.[8] Its chemical structure and deprotection mechanism are shown in Figure 1.3. Upon light irradiation, photogenerated acids cleave the adamantyl group, generating an exocyclic double bond on this pendant group and changing the ester linkage to a carboxylic group. The exposed area can then be removed by an aqueous base developer.

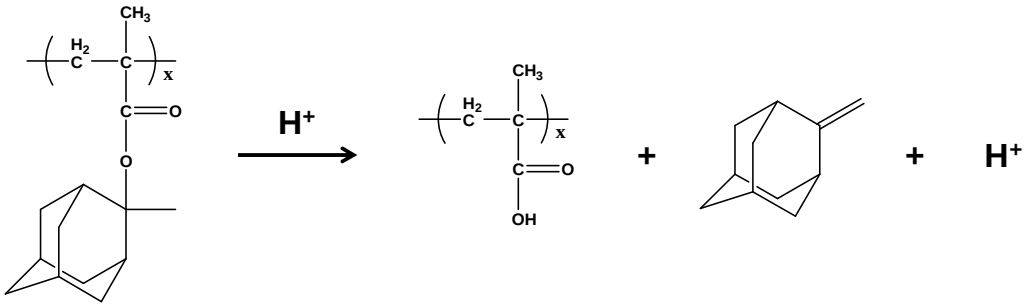

Figure 1.3 Deprotection mechanism of 2-methyl-2-adamantyl methacrylate by photogenerated acids.

Currently, 193 nm immersion lithography and 193 nm PR are used in high volume manufacturing to fabricate state-of-the-art devices. After development, 193 nm PR acts as a mask material in the following plasma etch steps. Thus, its interaction with plasmas is of critical importance to realize future generations of devices.

1.2.2 Plasma Etch

Plasma etch has been an indispensable process of integrated circuit fabrication since early 1970s because of its ability to provide anisotropic etch profile with desired selectivity and uniformity.[1, 9] Applications of new materials and new device architecture (ie. non-planar transistor) along with the continuous scaling of device dimensions all challenge plasma etch processes.

Roughening of PR can be introduced in lithography steps and during plasma etch.[10-15] PR degradation during plasma etch can lead to sidewall striations, collapse of line features, surface roughness and line width roughness (LWR), as the scanning electron microscopy (SEM) images shown in Figure 1.4. LWR is defined as the 3σ standard deviation of the pattern width. It is noted that even without complex plasma chemistry, inert gas plasmas, such as Ar, can cause high levels of PR roughening (Figure 1.4c).[15]

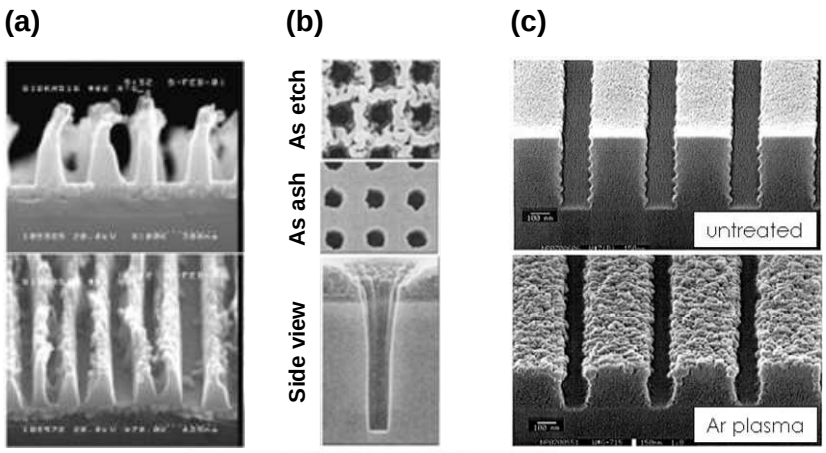

Figure 1.4 (a) Collapse of photoresist after $CF_4/CHF_3/O_2/Ar$ hardmask etch, side view and tilt view.[11] (b) Via-hole top view after etching, top view after ashing, and side view after etching. The etch chemistry was $Ar/C_4F_6/O_2/CO$.[13] (c) Photoresist surface roughness on patterns before and after pure Ar plasma etch.[15]

Furthermore, PR roughening is known to transfer to underlying layers during plasma etch.[12, 16] Figure 1.5 shows the AFM image of patterned 248 nm PR stack sidewall after plasma etch. The etch chemistry was N_2/H_2 for anti-reflective coating and CF_4/CHF_3 for SiO_2. After plasma etch, the sidewall roughness of the PR layer propagates to the underlying multilayer stack, forming excessive striations. This directly impacts the pattern profiles and results in variation in critical dimension (CD) control and decreased device performance, such as effects on both the off-state leakage and the drive current.[17] According to the International Technology Roadmap for Semiconductors (ITRS), by 2016, the physical gate length will be 15.3 nm and gate length control (3σ) must be within 1.84 nm.[18] CD control is acknowledged to be a major challenge for future integrated circuit manufacturing. Current goals of the semiconductor industry are to reduce roughness developed during device patterning to less than 2 nm (3σ).

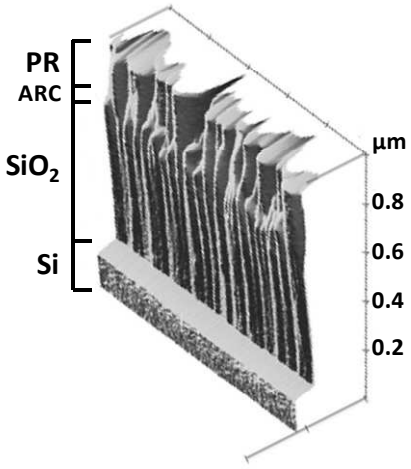

Figure 1.5 Sidewall roughness propagation on 248 nm PR after plasma etch. Adapted from reference [12].

Compared to previous 248 nm PR, methacrylate-based 193 nm PR suffers from low plasma etch resistance, more severe degradation and a higher tendency to roughen, which is generally attributed to its high oxygen content.[19] While the problem becomes more and more important because of the shrinkage of device dimensions, the underlying mechanism is poorly understood. The first part of this dissertation will discuss the surface roughening of 193 nm PR and provide a scientific principle to qualitatively explain this phenomenon.

1.3 Surface Sterilization/Deactivation by Low Temperature Plasmas

Healthcare-associated infections (HAIs) are major challenges to patient safety and impose significant burdens on the healthcare system. While receiving medical treatment, patients obtain HAIs that lead to extended hospital stays and increased medical costs, and are a significant cause of morbidity and mortality. In USA, it was estimated that a total of 1.7 million cases of HAIs occurred (4.5 per 100 admissions), and almost 99,000 deaths resulted from or were associated with HAIs in 2002.[20] Similar prevalence was also reported in Europe.[21] Moreover, HAI is the sixth leading cause of death for the total population in USA.[22] The overall annual direct medical costs of HAIs to US hospitals is estimated to range from $28.4 to $33.8 billion, adjusted to 2007 dollars.[23] Risk factors of HAIs include contamination on the hands of healthcare workers, the medical equipment, and the environmental surfaces within healthcare facilities.[24, 25]

In USA, millions of surgical procedures are performed each year, involving contact of patients' sterile tissues and mucous membranes with medical instruments. Proper removal of infectious organisms and/or biomolecules is essential to prevent infections and disease transmission. Medical device reprocessing procedures require cleaning before disinfection or sterilization. Disinfection refers to reducing infecting vegetative bacteria to a very low level but not necessarily killing all bacterial spores. On the other hand, sterilization includes eliminating bacterial spores. Cleaning is normally accomplished manually or mechanically using water with detergents or enzymatic products to remove visible soil (e.g. organic and inorganic material). High-level disinfection is the minimal requirement for semi-critical items in contact with mucous membranes or non-intact skin, such as some endoscopes. It is conducted by using chemical disinfectants such as hydrogen peroxide and glutaraldehyde. For critical items that are in contact with sterile tissues or the vascular system, sterilization is of crucial importance. It is typically achieved by steam sterilization for heat-resistant items; for heat-sensitive items, low temperature processes are required, such as ethylene oxide or peracetic acid.[24] Improper reprocessing of reusable medical devices can result in harmful consequences. Several recent outbreaks of HAIs are directly related to contaminated endoscopes and surgical instruments.[26-29] Moreover, studies have shown protein and bacterial residues on reprocessed, ready-for-use instruments.[30-33] Baxter et al. found that there was no significant correlation between overall instrument complexity and protein soiling, which would compromise the effectiveness of sterilization processes. The protein contamination also increases the potential risks of medical care related transmission of Creutzfeldt-Jacob diseases (CJD). On the other hand, the concern of bacterial residues is primarily related to bacterial pyrogens, for example, lipopolysaccharide (LPS, also known as an endotoxin). LPS is the major component of the outer membrane of Gram-negative bacteria. The presence of LPS in host blood circulation could result in a generalized sepsis syndrome including fever, hypotension, respiratory dysfunction and may lead to multiple organ

failure and death.[34] The dilemma emerges: intricate modern instruments are often heat sensitive and difficult to clean, while bacterial endotoxins and prion proteins are particularly resistant to conventional sterilization procedures.[35, 36]

Low temperature plasmas appear to provide attractive options for sterilization and deactivation of virulent biomolecules. The advantages of plasma processes over conventional procedures are: first, the plasma discharge is maintained at an ambient or moderate temperature, which is ideal for heat-sensitive instruments; second, the plasma discharge can be sustained from pure or mixtures of nontoxic gases, such as argon, oxygen, and hydrogen, which are relatively safe both to the environment and personnel. Moreover, the effects of plasmas on bacterial spores, proteins, and bacterial endotoxins have been demonstrated.[37-39] Figure 1.6 shows the SEM images of *Bacillus subtilis* spores before and after 15 min of plasma exposures.[40] O_2 plasma caused some etching and reduction of the spore size (Figure 1.6b). O_2/CF_4 plasma caused strong etching and reached more than a 5 log reduction of spores (Figure 1.6c).

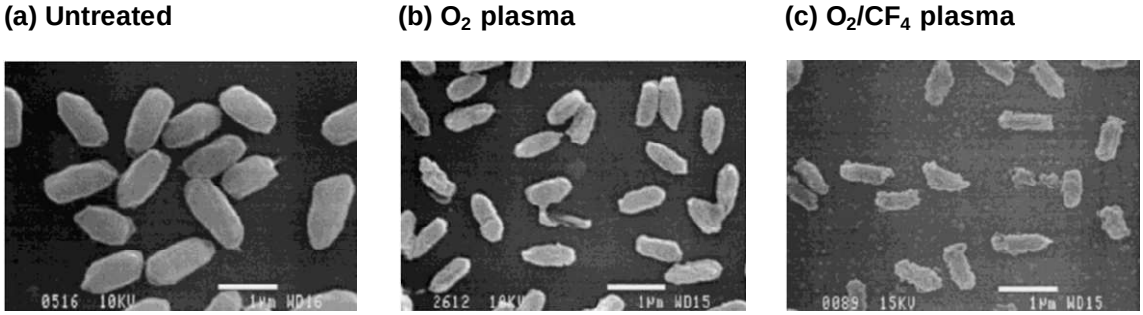

Figure 1.6 SEM images of *Bacillus subtilis* spores (a) untreated (b) after 15 min of O_2 plasma exposure (c) after 15 min of O_2/CF_4 plasma exposure. Adapted from reference [40].

Furthermore, it is often found that plasma conditions have to be optimized towards different biological targets. For example, plasma-generated UV photon flux must be optimized in order to reduce surface-resident bacterial spores at least 4 orders of magnitude. Under the condition where layers or stacks of spores are present, plasma-generated UV must be accompanied with energetic ions and reactive radical species impacting the surface simultaneously to achieve high etch rates. Hydrogen peroxide plasma-incorporated sterilization was patented in 1987 and marketed in the US in 1993.[24] Studies have shown that in the commercial STERRAD® system, the sporicidal effect is due to hydrogen peroxide vapor, and the plasma phase is used to decompose toxic residues.[41] It has been suggested to designate these processes as “plasma-assisted”.[42] Nevertheless, it is widely accepted that plasma-generated energetic and reactive species are responsible for plasma-induced sterilization/deactivation; however, how these species act alone or synergistically on biomolecules is not completely understood. We chose lipid A (*Salmonella minnesota* Re 595 mutant), the primary immune-stimulating region of LPS, as our model biomolecule to study the mechanism of plasma-induced structural modification and bioactivity alteration. The principles in this study are also relevant to all applications of atmospheric pressure plasmas to biological systems in the rapidly growing field of plasma medicine, including sterilization, therapeutic effects for wound healing, treatment for skin diseases and cancers.[43-49].

1.4 Beam System Approach

In spite of its technological importance, studying plasma-surface interactions in a plasma chamber is often difficult. As shown in Figure 1.7a, in addition to the charged and excited species generated in a plasma, reaction products can become part of the discharge and change the plasma chemistry. These products may form new species and consequently react with the substrate as ions or radicals. Furthermore, it is often difficult to independently control the various species generated in a plasma, making interpretation of results very challenging. To study individual species effect in a plasma reactor, mask structures are usually involved to select species impacting the samples. For example, optical windows with different cut-off wavelengths can filter photons with different energies.[50, 51] Radicals can diffuse into the gap between the mask structures and react with samples.[52] Inevitably, these techniques decrease the species flux and require extra efforts to estimate the flux of interest impacting the samples. Furthermore, studies of pure ion effect have not yet been achieved in plasma reactors.

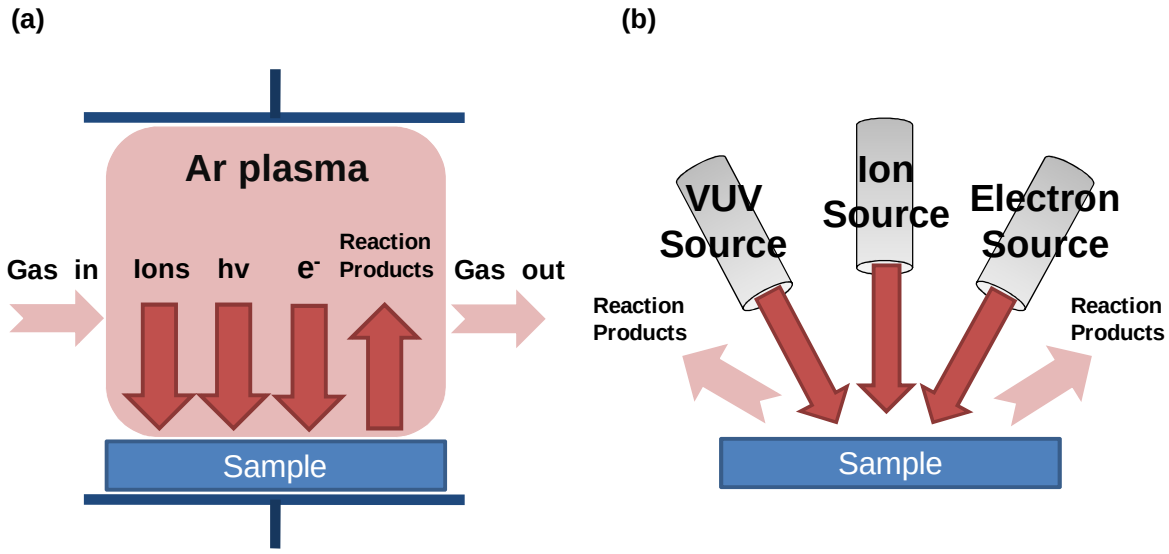

Figure 1.7 (a) Plasma species impact the sample in a plasma reactor. Reaction products can become part of the plasma discharge. Characterization of plasma-surface interactions is inherently difficult. (b) Beam sources in a vacuum beam system allow for studies being conducted in a well-controlled environment.

In contrast, a vacuum beam system, illustrated in Figure 1.7b, can be equipped with well-characterized and independently controlled beam sources. It thus provides the ability to decouple the effects of various species in a well-controlled environment. Species flux can be directly characterized at the sample position. Different sources can be used separately to study their individual effects on the material of interest. The combination of sources can further be used to mimic relevant plasma conditions.

Various studies have shown the ability of a vacuum beam system to provide valuable insights into plasma-material interactions. Coburn and Winters demonstrated that Si etch rate with simultaneous 450 eV Ar ions and XeF_2 molecules is about 8 times higher than the sum of the etch rate for individual species.[53] Kota et al. found the increased etch selectivity of $WSi_{1.66}$

over poly-Si under the presence of oxygen ions and chlorine atoms.[54] Greer et al. studied the effects of Ar ions, neutral deuterium and fluorine atoms on the etch yield of i-line and g-line PRs.[55] They showed that the etch yield transitioned from physical sputtering to chemical sputtering with an increase of F/Ar^+ flux ratio. Chang et al. characterized SiO_2 etch under high-density chlorine plasma conditions. They found that atomic chlorine enhanced the etch yield of Ar ion by a factor of 3-4.[56]

The drawbacks of a vacuum beam system include the difficulties of generating/including all plasma species and low species flux compared to a plasma reactor. One has to pay extra attention to choose representative species, control the ratio of various species or match the total fluence of species to a plasma experiment. Fundamental plasma-surface interactions can thus be studied by carefully compared the results obtained from a vacuum beam system and a plasma reactor.

1.5 Dissertation Outline

The goal of this dissertation work is to understand the fundamental mechanisms of plasma-generated species interaction with organic materials and resulting modifications. A vacuum beam system is used to study the effects of plasma species in relevant plasma conditions. Chapter 2 will provide details of the vacuum beam system, the operation principles and diagnostics of various beam sources used in this study. Chapter 3 will address the materials, analysis tools and characterization assays. The first focus, roughening of 193 nm PR will be presented in Chapter 4 and 5. Chapter 4 will focus on the individual effect of ions, VUV photons and electrons, and their combination in 193 nm PR roughening. Chapter 5 will be devoted to 193 nm PR-associated homopolymers. The critical role of 2-methyl-2-adamantyl leaving group in PR surface roughening will be demonstrated and a bi-layer wrinkling mechanism will be discussed. The second focus, plasma deactivation of virulent biomolecules will be conveyed in Chapter 6. The chemical modification and decreased endotoxic activity of lipid A after VUV photon, oxygen radical, and deuterium radical processes will be presented.

Chapter 2

The Vacuum Beam System and Source Diagnostics

2.1 Abstract

This chapter will introduce the vacuum beam system used in this study. Various beam sources, including an ion gun, a VUV lamp source, an electron gun, and a radical source were mounted on the beam system to study fundamental plasma-material interactions. The operation principle and characterization of these beam sources will also be presented in the following sections.

2.2 The Vacuum Beam System

The vacuum beam system was designed to study mechanisms of plasma-surface interactions by formal graduate student Yoshie Kimura, and modified and used by formal graduate student Dustin Nest. The schematic of the system is shown in Figure 2.1. The flanges are numbered following Yoshie Kimura's notation. Details along with additional capability beyond the studies presented here can be found in the dissertations of Yoshie Kimura and Dustin Nest. [57, 58]

A base pressure of 1.5×10^{-8} Torr was maintained with a 2000 $L\cdot s^{-1}$ turbo pump (STP-H2000C, SEIKO SEIKI), backed by a mechanical roughing pump. The main chamber pressure was monitored with an ion gauge (MDC Vacuum Products, Hayward, CA, USA). A magnetically-coupled load-lock transfer arm (Transfer Engineering and Manufacturing, Inc., Fremont, CA, USA) was designed to load samples without breaking the vacuum of the main chamber. The transfer arm was pumped down with a 300 $L\cdot s^{-1}$ turbo pump (TV 301 Navigator, Varian, Inc., now Agilent Technologies, Santa Clara, CA, USA), backed by a second mechanical roughing pump. The pressure of the transfer arm chamber was monitored with a second ion gauge (MDC Vacuum Products).

A 1.5 cm × 2 cm piece of Si-wafer sample was attached to a copper block by thermal paste and secured to the sample holder. The sample holder could be translated into the chamber

through the transfer arm system and set on a rotational dock. With the aid of the rotational/translational sample dock, samples could be rotated to face the beam source, or translated out of the chamber center to allow for characterization of different beam sources. An external water bath was connected to the dock to control the sample temperature. The temperature of the underside of the copper block was monitored with a thermocouple (type K, OMEGA Engineering, Inc., Stamford, CT, USA).

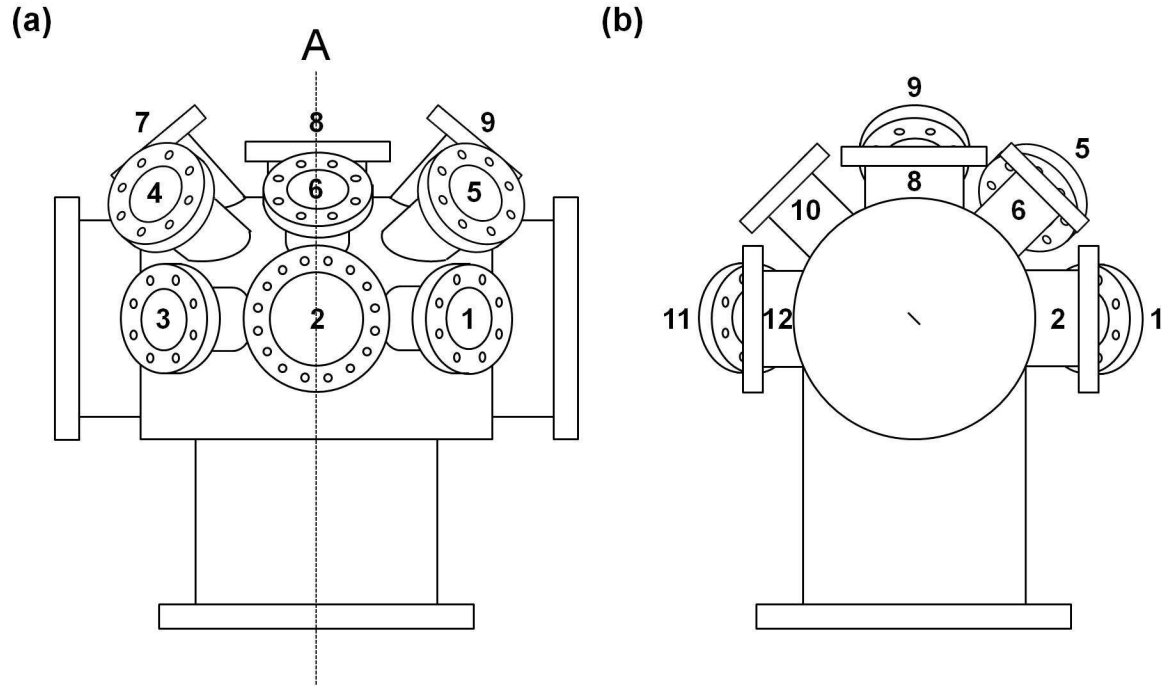

Figure 2.1 (a) Side view of the main chamber (b) cross section view of the main chamber at plane A labeled in (a). Dimensions of each flange can be found in the dissertation of Yoshi Kimura.[57]

2.3 Ion Source

A Kaufman-type ion gun (1 cm ion source, Commonwealth Scientific Corporation) was used in this study to generate 150 eV Ar ions. The ion gun was mounted on flange 6. Ar gas was fed into the discharge chamber of the ion gun, raising the main chamber base pressure to about 1×10^{-4} Torr. The cathode was a three-turn filament made of 0.013 cm diameter tungsten wire, which had to be replaced regularly to maintain steady operation. A discharge between the anode and the cathode generated positive ions which bore the effective anode potential (150 V). The discharge voltage was set to 40 V to minimize the production of doubly charged ions. Ions were extracted from the discharge chamber by the negatively biased accelerator grid through the screen grid. When the ion beam was directed to an electrically insulated sample, such as polymers, an external neutralizer made of 0.025 cm diameter tungsten wire was used at ~ -5 V with ~6 A of current. The neutralizer provided low energy electrons and thus prevented sample charging.

All ion beam experiments were conducted at normal incidence to the sample surface as in typical plasma conditions. The ion current at the sample position was measured with a Faraday cup (aperture size ~4.55×10^{-4} cm^2) mounted on flange 10 and connected to a picoammeter (Keithley Instruments, Inc., Cleveland, OH, USA). In this study, an ion current of 2.8×10^{14} $ions\cdot cm^{-2}\cdot s^{-1}$ (±10%) was used and a 1 h exposure resulted in an ion fluence of 1.0×10^{18} $ions\cdot cm^{-2}$ (±10%).

2.4 Vacuum Ultraviolet Photon Source

A high intensity 147 nm VUV emission line was generated with a closed-volume Xe lamp source (Resonance Ltd., Barrie, ON, Canada). In the photoresist studies, the VUV source was mounted on flange 2; in the lipid A deactivation study, the VUV source was mounted on flange 6. The lamp assembly has an internal RF exciter to power the Xe discharge and is sealed with a MgF_2 window (cut-off wavelength, λ_c = 112 nm). Because of fixed gas chemistry, gas pressure, and input power, the photon emission from the lamp source is unchangeable. The photon flux at the sample position can only be adjusted by changing the working distance.

With the VUV source mounted on flange 2, absolute calibration of the VUV photon flux was conducted by a NIST-calibrated CsI diode (Resonance Ltd.). At a working distance of 4.4 cm, the photon flux was 1.9×10^{14} $photons\cdot cm^{-2}\cdot s^{-1}$. Thus, the photon flux irradiating on the sample surface was ~1.34×10^{14} $photons\cdot cm^{-2}\cdot s^{-1}$, corrected by an incidence angle of 45° to the surface normal. VUV spectra were obtained by a VUV spectrometer (Resonance Ltd.) mounted on flange 12 to monitor the stability of the source, as shown in Figure 2.2. Detailed description of photon flux characterization and the use of VUV spectrometer can be found in the dissertations of Dustin Nest and Monica Titus. [58, 59]

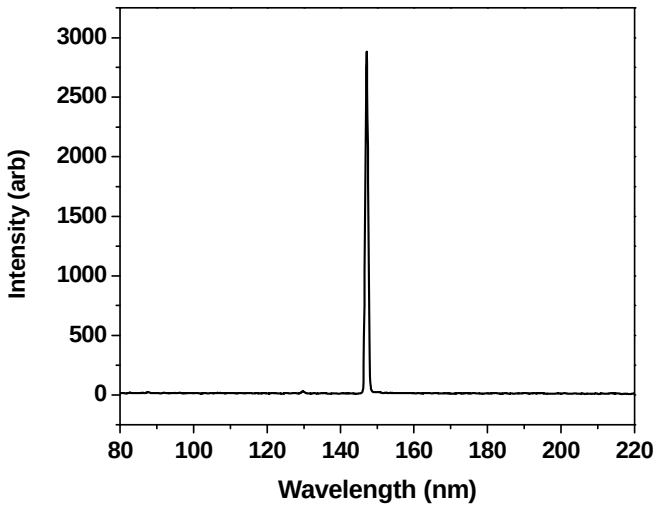

Figure 2.2 VUV spectrum obtained from the Resonance Ltd. Xe source. It shows a nearly monotonic emission line at 147 nm.

2.5 Electron Source

A uniform flood beam of electrons was generated with an electron gun (EFG-7, Kimball Physics, Wilton, NH, USA) mounted on flange 9. The electron beam is produced and controlled by the following elements: triode, focus, and deflection. The triode is composed of three elements in the following sequence: cathode, grid, and grounded anode. The cathode is a thermionic emitter, consisting of a tantalum disc mounted on a hairpin filament wire. The disc emits electrons when the filament wire is heated by the voltage source. The electrons are then accelerated to full kinetic energy by the triode's electric field. The divergence of the beam can be controlled by the focusing lens. The position of the beam can be adjusted by the cylindrical 4-pole deflector.

In this study, a 1 keV electron beam was used. The electron current at the sample position was measured with a home-built Faraday cup (aperture size ~19.6×10^{-4} cm^2) mounted on flange 7 and connected to a picoammeter (Keithley Instruments, Inc.). For electron-only experiments, electrons impacted the surface with an incident angle of 40° with respect to surface normal. For experiments with other beam sources, the incident angle was 57° to surface normal.

2.6 Radical Source

Oxygen and deuterium radicals were generated by a thermal gas cracker (TC-50, Oxford Applied Research, Witney, Oxfordshire, UK). In the lipid A deactivation study, the source was mounted on flange 2. There are plasma-based radical sources available, which provide a higher radical flux. However, those sources inherently generate UV/VUV and metastable species, and thus make them unsuitable in this study.

The parent molecules were fed through a catalytic capillary by a mass flow controller. The mass flow controller was not calibrated so the absolute gas flow rate was unknown, but estimated to be roughly a few tenths of 1 sccm. The gas flow increased the chamber base pressure to ~1×10^{-6} Torr. The capillary was heated by electrons thermally emitted from a heated filament. Molecules encountering the wall of the hot capillary were thermally dissociated. The source was operated at a power of 60 W for both oxygen and deuterium. At a power of 60 W, the tube temperature estimated by the vendor was roughly 1000 °C. The capillary was mounted in a directly water-cooled socket to prevent the samples from radiative heating. A manual shutter was placed in front of the capillary tube to shield or expose samples to direct radical beams.

The characterization of the radical beam was conducted by threshold ionization mass spectrometry, which will be presented in details in the following section.

2.7 Threshold Ionization Mass Spectrometry

Threshold ionization mass spectrometry (TIMS), also called appearance potential mass spectrometry (APMS), has been successfully applied in this lab previously. This study mainly follows the procedure published by Singh et al.[60]

A quadrupole mass spectrometer (PIC 300 quadrupole mass spectrometer, Hiden Analytical, Warrington, UK) was positioned on a translator on flange 8. The probe unit of the mass spectrometer consists of an ion counting channeltron detector, a quadrupole mass analyzer, and an ionizer, which is an electron bombardment source to create ions from neutral molecules.

The ionizer and quadrupole assembly was translated down, placing the ionizer at the sample position. The mass spectrometer signal is independent of the neutral velocity and is directly proportional to the neutral number density in the ionizer.[60] Figure 2.3 illustrates the relative positions of the ionizer/quadrupole assembly, the thermal cracker, and the manual shutter. When the shutter was open, the ionizer was in direct line-of-sight of the radical beam. Under this condition, the signal obtained by the mass spectrometer was proportional to the sum of beam and background radical number density. When the shutter blocked the beam, the signal acquired by the mass spectrometer was only proportional to the background radical number density. The signal proportional to the beam component could thus be obtained by subtracting the shutter-blocked signal from the shutter-open signal.

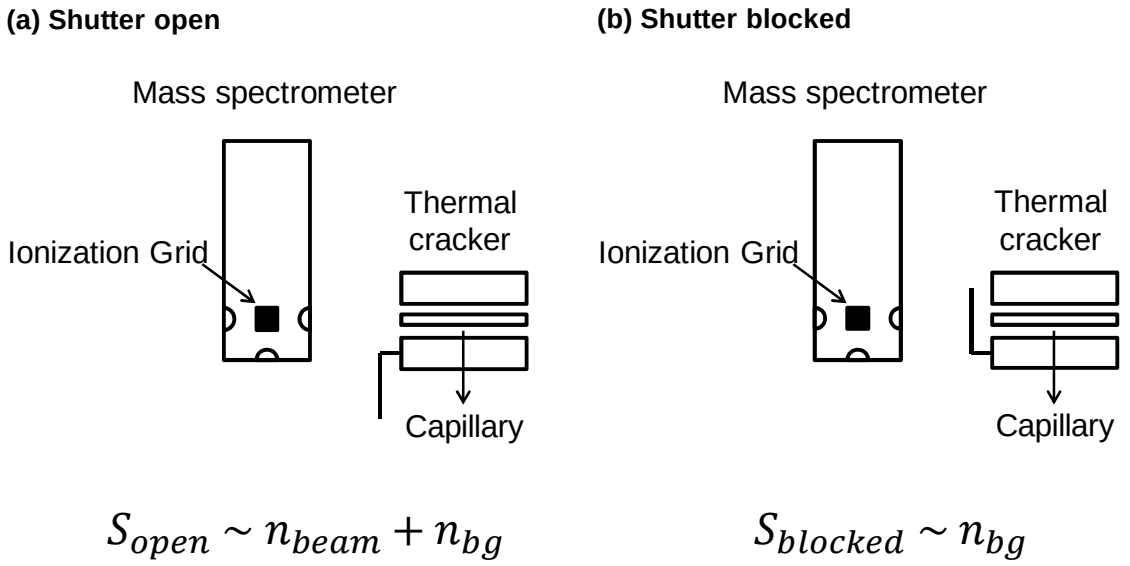

Figure 2.3 Relative positions of the ionizer/quadrupole assembly, the thermal cracker, and the manual shutter. (a) Shutter open; the mass spectrometer signal is proportional to the sum of beam and background (bg) radical number density; (b) Shutter blocked; the mass spectrometer signal is only proportional to the background radical number density.

TIMS utilizes the energy difference between the direct ionization threshold of a radical and the dissociation ionization of a parent molecule. By sweeping the ionizing electron energy from 10 to 25 eV, the oxygen and deuterium radical signals were monitored at m/z = 16 and 2, respectively. Ar was used as a reference gas to calibrate the electron energy scale and calculate the absolute oxygen or deuterium radical flux at the sample position. Ar gas flow was fed through the same capillary tube with the shutter blocked and 0 W source power. Under this condition, the Ar signal was proportional to the Ar number density in the vacuum chamber, where its pressure was monitored by an ionization gauge.

Figure 2.4 shows the measured oxygen radical beam signal from the thermal cracker, with the shutter blocked (○) and open (■), respectively. The source power was 60 W. The signal above ~19 eV is due to the dissociation of O_2 parent molecules.[61] The Ar signal (Δ) was conducted in a separate measurement with an Ar pressure of 1.2×10^{-6} Torr and shutter blocked. The energy scale was calibrated using the Ar^+ threshold, ~15.8 eV.[62, 63] The solid lines are the linear fits to the signals. The curvature of the signal near the threshold is possibly due to the spread in electron energy.

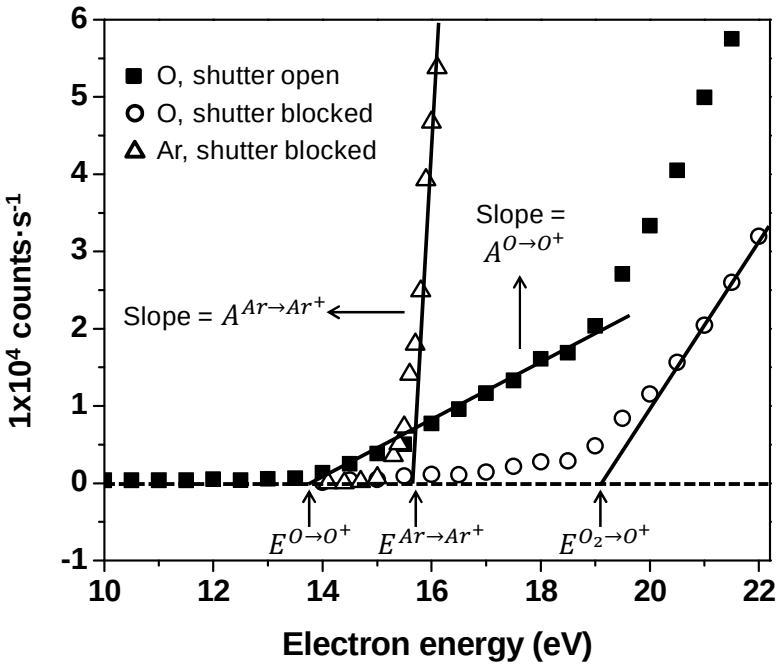

Figure 2.4 Measured oxygen signal with shutter open (■) and blocked (○).The Ar signal (Δ) was conducted in a separate measurement with an Ar pressure of 1.2×10^{-6} Torr and shutter blocked. The solid lines are the linear fits to the signals.

The absolute radical number densities of the beam and background component were calculated by the following equations:[60]

$$\frac{n_X^{beam}}{n_{Ar}^{bg}} = \left(\frac{A_{beam}^{X\rightarrow X^+}}{A^{Ar\rightarrow Ar^+}}\right)\left(\frac{\lambda^{Ar\rightarrow Ar^+}}{\lambda^{X\rightarrow X^+}}\right)\left[\frac{t\left(m_{Ar^+}\right)\cdot\theta\left(m_{Ar^+}\right)}{t\left(m_{X^+}\right)\cdot\theta\left(m_{X^+}\right)}\right] \tag{2.1}$$

$$\frac{n_X^{bg}}{n_{Ar}^{bg}} = \left(\frac{A_{bg}^{X\rightarrow X^+}}{A^{Ar\rightarrow Ar^+}}\right)\left(\frac{\lambda^{Ar\rightarrow Ar^+}}{\lambda^{X\rightarrow X^+}}\right)\left[\frac{t\left(m_{Ar^+}\right)\cdot\theta\left(m_{Ar^+}\right)}{t\left(m_{X^+}\right)\cdot\theta\left(m_{X^+}\right)}\right] \tag{2.2}$$

n_X^{beam}	The beam number density of radical in the ionizer
n_X^{bg}	The background number density of radical in the ionizer
n_{Ar}^{bg}	The number density of Ar in the ionizer (with shutter blocked)
$A^{X\to X^+}$ and $A^{Ar\to Ar^+}$	The slopes of the linear fits to the radical signal and Ar^+ reference signal
$\lambda^{X\to X^+}$ and $\lambda^{Ar\to Ar^+}$	The slopes of the linear fits of the cross sections of radical and Ar direct ionization
t	Mass to charge ratio (m/z) dependent transmission efficiency of the quadrupole mass filter; here z = 1
θ	Mass to charge ratio (m/z) dependent detection coefficient of the channeltron detector; here z = 1

The product of the transmission efficiency and detection coefficient in our mass spectrometer was equal to $m^{-0.81}$.[60] n_{Ar}^{bg} was calculated from the Ar pressure in the chamber with the ideal gas law. $A^{X\to X^+}$ and $A^{Ar\to Ar^+}$ were measured by TIMS. $\lambda^{X\to X^+}$ and $\lambda^{Ar\to Ar^+}$ were calculated from linear fits of published cross sections.[64-66] We assumed the extraction efficiency of ions from the ionizer was the same at different species temperatures. As a result, the absolute number density of radicals could be calculated.

The calculated number density of radicals at the sample position is shown in Figure 2.5. For oxygen and deuterium radicals, measurements were conducted at various source powers and two different parent gas flow rates. The mass flow controller was not calibrated so the absolute gas flow rate was unknown, but the resulting main chamber pressure is reported here. For oxygen radical measurements, the main chamber pressure was 1×10^{-6} Torr for the high flow rate condition and 6.4×10^{-7} Torr for the low flow rate condition. For deuterium radical measurements, the main chamber pressure was 1×10^{-6} Torr for the high flow rate condition and 6.8×10^{-7} Torr for the low flow rate condition.

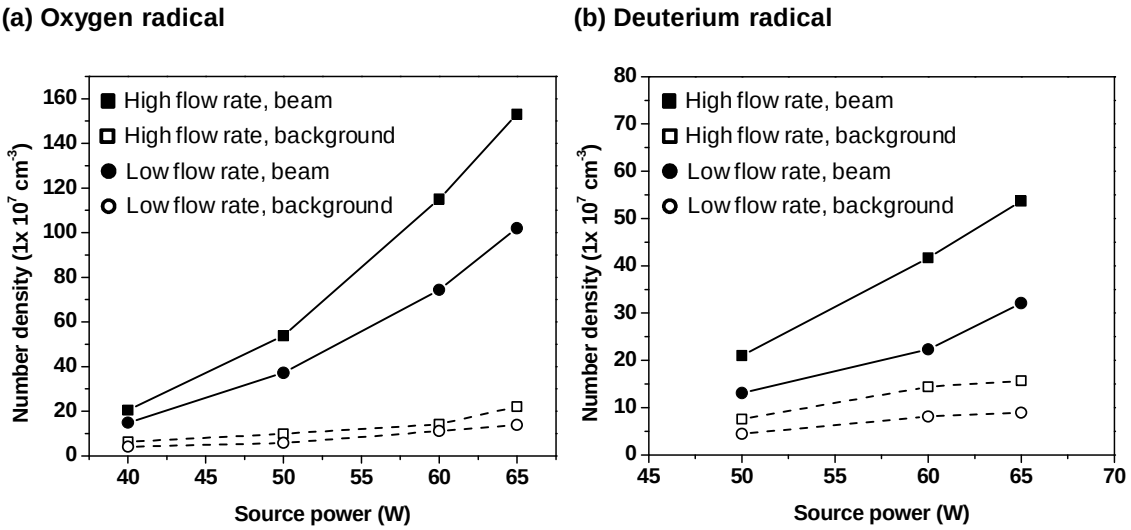

Figure 2.5 (a) Calculated beam and background number density of oxygen radical at various source powers. The main chamber pressure was 1×10^{-6} Torr for the high flow rate condition and 6.4×10^{-7} Torr for the low flow rate condition. (b) Calculated beam and background number density of deuterium radical at various source powers. The main chamber pressure was 1×10^{-6} Torr for the high flow rate condition and 6.8×10^{-7} Torr for the low flow rate condition.

The beam component had an incident angle of 45° to sample surface normal. The radical flux at the sample position could then be obtained by the following equations:

$$\Gamma_X^{beam} = n_X^{beam} \cdot \bar{v}_X^{beam} \cdot \cos(45°) = 0.71 n_X^{beam} \sqrt{\frac{8k_B T_{beam}}{\pi m_X}} \tag{2.3}$$

$$\Gamma_X^{bg} = \frac{1}{4} \cdot n_X^{bg} \cdot \bar{v}_X^{bg} = 0.25 n_X^{bg} \sqrt{\frac{8k_B T_{bg}}{\pi m_X}} \tag{2.4}$$

Γ_X^{beam} and Γ_X^{bg}	The flux of beam and background component of species X
$\bar{v}_X^{beam}$ and $\bar{v}_X^{bg}$	The mean speed of beam and background component of species X
k_B	Boltzmann constant
m_X	The mass of species X
T_{beam}	The temperature of the beam component. We assumed the beam component was thermalized with the capillary tube, which was ~1300 K at an operation power of 60 W.
T_{bg}	The temperature of the background component. We assumed the background component was thermalized with chamber walls, which were at room temperature.

The total flux received at sample surface was the summation of the beam component and the background component:

$$\Gamma_X^{tot} = \Gamma_X^{beam} + \Gamma_X^{bg} \tag{2.5}$$

The beam component was usually 30-fold higher than the background component. At 60 W source power, the typical oxygen radical flux was ~7.5×10^{13} oxygen·cm^{-2}·s^{-1} (±10%), and the typical deuterium radical flux was ~4.6×10^{13} deuterium·cm^{-2}·s^{-1} (±10%). The choice of deuterium instead of hydrogen was due to the limitation of our mass spectrometer: the parent H_2 signal (m/z = 2) masked the atomic H signal (m/z = 1). This was not a problem in the case of deuterium, where the parent D_2 signal (m/z = 4) is 2 amu apart from the atomic D signal (m/z = 2). The kinetic energy of the radicals was ~0.11 eV at a temperature of ~1300 K.

Chapter 3
Materials and Characterization

3.1 Abstract

Present studies of photoresist material surface roughening were conducted with 193 nm photoresist and associated homopolymers. Studies of endotoxic biomolecule deactivation were carried out with lipid A from *Salmonella minnesota* Re 595 and synthetic monophosphoryl lipid A. The chemical structures of these materials will be presented in this chapter. The analysis tools, including quartz crystal microbalance (QCM), transmission Fourier transform infrared (FTIR) spectroscopy, atomic force microscopy (AFM), in situ mass spectrometry, quadrupole time-of-flight (Q-ToF) mass spectrometry equipped with an electrospray ionization (ESI) source, and time-of-flight secondary ion mass spectrometry (ToF-SIMS) will also be introduced here. Lastly, the protocol of human whole blood tests for endotoxic activity determination will be described.

3.2 Photoresist Polymers: 193 nm PR and Associated Homopolymers

Chemical structures of the photoresist (PR) materials are shown in Figure 3.1. As presented in Figure 3.1a, the 193 nm PR is a random terpolymer consisting of 2-methyl-2-adamantyl methacrylate (MAMA) in the leaving group, α-gamma butyrolactone methacrylate (α-GBLMA) in the lactone group and a R-functionalized adamantyl methacrylate (RAMA) polar group for adhesion. The molar ratio of MAMA/α-GBLMA/RAMA is 40/40/20. In this commercial PR, the three side-groups could complicate the analysis of roughening mechanisms. We therefore chose two homopolymers, p-MAMA (Figure 3.1b, T_g was unable to be determined before decomposition) and p-RAMA (Figure 3.1c, T_g ~228 °C), to better understand the role of the side group composition in plasma-induced PR surface roughening.

The polymer samples were provided by the Dow Chemical Company with a film thickness of 250 nm on silicon wafers. The polymers did not contain photoacid generators and base quenchers. After beam exposures, these samples were characterized by ex situ transmission Fourier transform infrared (FTIR) spectroscopy for film bulk chemical modification. The surface morphology was imaged with atomic force microscopy (AFM). In situ mass spectrometry was also used to determine the photolysis products resulting from vacuum ultraviolet (VUV) exposures.

Besides polymer films, polymer solution (in propylene glycol monomethyl ether acetate, PGMEA) was also supplied by the Dow Chemical Company. The solution was used to spin-coat quartz crystal microbalance (QCM) sensors for etch yield measurements. The coating parameters to obtain a 250 nm film were also provided by Dow (spin speed: ~2850 rpm; spin time: 30 s; soft bake: 120 °C/60 s).

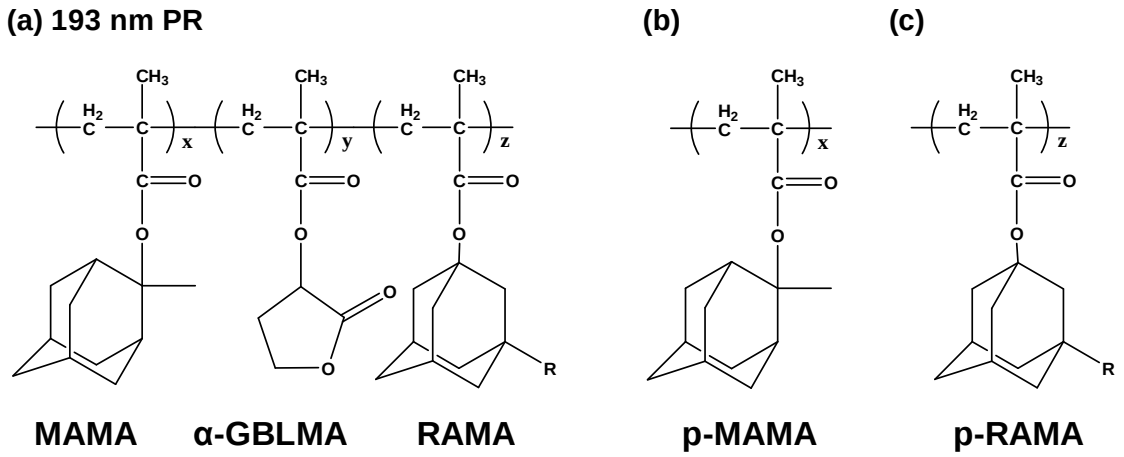

Figure 3.1 Chemical structure of polymers used in this study. (a) 193 nm PR consisting of MAMA (leaving group), α-GBLMA (lactone group), and RAMA (polar group). (b) p-MAMA. (c) p-RAMA.

3.3 Lipid A

The chemical structure of *Salmonella minnesota* Re 595 Lipid A (Sigma-Aldrich, St. Louis, MO, USA) is shown in Figure 3.2a. It consists of a β(1-6)-linked D-glucosamine disaccharide carrying two phosphoryl groups at positions 1 and 4'. This hydrophilic backbone is attached to four acyl chains by ester (positions 3 and 3') and amide linkages (positions 2 and 2').[67] In the case of *Salmonella minnesota* Re 595 mutant, these residues are saturated (*R*)-3-hydroxytetradecanoic acids. Additionally, the hydroxyl groups on two of these residues (positions 2' and 3') are further substituted with saturated dodecanoic and tetradecanoic acid, respectively.[68] The diphosphoryl lipid A, obtained by hydrolysis of Re mutant lipopolysaccharide (LPS), is a mixture with various non-stoichiometric substitutions and molecular masses. Non-stoichiometric substitutions, including 4-amino-4-deoxy-L-arabinose (L-Ara4N), phosphorylethanolamine (pEtN), hexadecanoic acid, and (*S*)-2-hydroxytetradecanoic acid, are shown with dashed bonds. The chemical structure of synthetic monophosphoryl lipid A (Avanti Polar Lipids, Alabaster, AL, USA) is shown in Figure 3.2b. This molecule carries a phosphoryl group at position 4', and all the acyl residues are tetradecanoic acids. In contrast to extracted diphosphoryl lipid A, the synthetic monophosphoryl lipid A has a well-defined molecular mass and structure.

Lipid A was dissolved in a 74:23:3 chloroform:methanol:water solution and diluted to desired concentrations. Lipid A film was prepared by spotting 10 μl of lipid A solution on

UV/ozone-cleaned silicon substrate and dried overnight. Unless otherwise specified, samples were prepared with a 1 mg·ml^{-1} stock solution. Besides ex situ FTIR, AFM, in situ mass spectrometry and QCM applied in PR studies, lipid A samples were also analyzed by quadrupole time-of-flight (Q-ToF) mass spectrometry equipped with an electrospray ionization (ESI) source, and time-of-flight secondary ion mass spectrometry (ToF-SIMS) to obtain further information regarding to its structural change after beam exposures. The alteration of lipid A's endotoxic activity was assessed by human whole blood-based tests. The analysis tools will be described in detail in the following sections.

(a) Lipid A (*Salmonella minnesota* Re 595) **(b) Synthetic monophosphoryl lipid A**

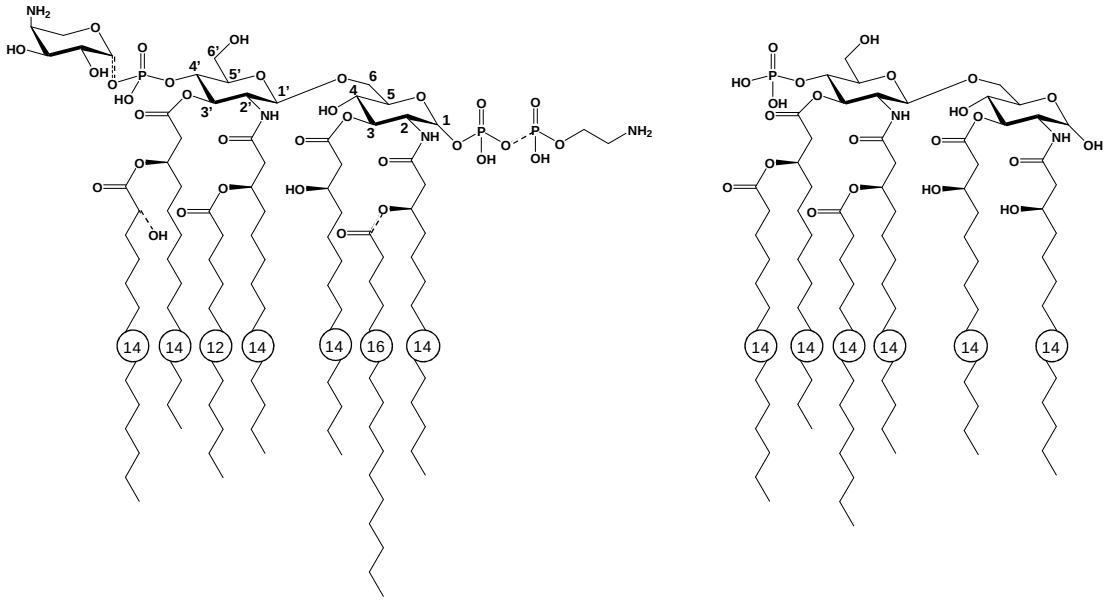

Figure 3.2 Chemical structure of (a) *Salmonella minnesota* Re 595 Lipid A, (b) synthetic monophosphoryl lipid A.

3.4 Quartz Crystal Microbalance

The sample holder of the beam system can accommodate a quartz crystal microbalance (QCM) holder. An electric feedthrough interconnects the QCM sensor (gold electrode, 6 MHz, INFICON, East Syracuse, NY, USA) and the crystal oscillator/thickness monitor (TM-400, Maxtek, Santa Fe Springs, CA, USA), which sits under ambient pressure. The unloaded QCM sensor is excited by the oscillator into thickness-shear mode at its resonance frequency, ~6 MHz. The oscillation frequency increases when material is removed from the crystal and decreases when material is deposited on it. Thus, the change of oscillation frequency monitors the in situ material removal or deposition. A frequency change of 0.1 Hz corresponds to a mass change of 1.23×10^{-9} g·cm^{-2}. In the absence of any processes, the drift of oscillation frequency was about 3 Hz per hour in our system, making the measurement uncertainty about 8.3×10^{-4} Hz·s^{-1}.

The 193 nm PR was spun-coat onto QCM sensors to obtain a film thickness ~250 nm. In the case of lipid A, 30 ml of 1 mg·ml^{-1} lipid A solution was spotted on each sensor. The sensors were dried overnight. The estimated surface coverage of lipid A on a sensor was about 50%. All QCM measurements were conducted at room temperature.

3.5 Transmission Fourier Transform Infrared Spectroscopy

Photoresist polymers and lipid A films were characterized with ex situ FTIR spectroscopy (Excalibur FTS-3000, Digilab, now Agilent Technologies, Santa Clara, CA, USA). Mid-Infrared radiation has the right energy (600-4000 cm^{-1}) for stretching and bending vibrations in organic molecules, and thus provides an easy assay for sample characterization.

The broadband infrared emitted from a ceramic source travels through the aperture, the interferometer, the sample compartment, and then gets detected by a cryogenic mercury cadmium telluride (MCT) detector for mid-IR measurements. The application of an interferometer enables the simultaneous measurement of all the wavelengths in interests. As shown in Figure 3.3, the interferometer applies a KBr beamsplitter to transmit 50% of the incident infrared light to a moving mirror, and reflect the other 50% of the light to a fixed mirror. Once the two beams are reflected back from the mirrors, they interfere with each other and leave the interferometer. The position of the moving mirror determines the difference in optical path of the two beams. It in turn causes constructive or destructive interference of the light. The fundamental measurement obtained by an FTIR is an "interferogram", which is the interfering light intensity as a function of the moving mirror position. The interferogram contains the information of every infrared frequency coming from the source, and thus all frequencies are being measured simultaneously. The measured interferogram cannot be directly interpreted, and is Fourier transformed back to a frequency spectrum (light intensity at each individual frequency) for analysis.[69]

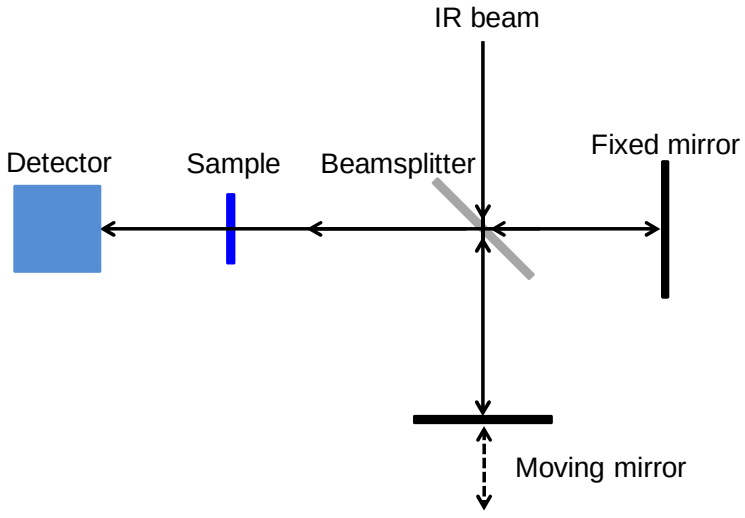

Figure 3.3 The optical diagram of an interferometer.

Sample acquisition and analysis were performed with software Resolutions Pro (Varian, Inc., now Agilent Technologies). To obtain absorbance (A) at a specific wavelength, the Beer-Lambert law was used:

$$A = -\log_{10}\left(\frac{I}{I_0}\right) \tag{3.1}$$

I The intensity of the transmitted IR
I_0 The intensity of the incident IR

The PR and lipid A films were deposited on silicon wafers. The transmitted IR contains the signal from both the film and the Si substrate. To obtain film-only spectra, the Si wafer-only signal must be subtracted. It was completed by taking the ratio of the intensity spectra of the sample (film + Si substrate) and the intensity spectra of the bare Si substrate:

$$A_{film} = A_{sample} - A_{Si} = -\log_{10}\left(\frac{I_{sample}}{I_0}\right) + \log_{10}\left(\frac{I_{Si}}{I_0}\right) = -\log_{10}\left(\frac{I_{sample}}{I_0}\frac{I_0}{I_{Si}}\right) \tag{3.2}$$

All spectra were truncated and baseline corrected to retain the absorption bands between 500 cm^{-1} and 4000 cm^{-1}.

3.6 Atomic Force Microscopy

The surface morphology of samples was imaged by atomic force microscopy (AFM, MultiMode, Veeco, now Bruker AXS, Madison, WI, USA) in tapping mode. In principle, a cantilever with a sharp tip (PPP-NCL, NANOSENORS) oscillates and lightly taps the sample surface. An optical lever is used to monitor the oscillation amplitude of the cantilever: a laser beam is shined to the back of the cantilever and reflected to a split photodiode detector. A digital feedback loop controls the vertical position (z direction) of the scanner to maintain a constant tip-sample interaction, and thus maintain a constant root mean square (RMS) oscillation signal. The vertical position of the scanner at each lateral position (x, y) is recorded and forms the topographic image.

The data acquisition, process, and analysis were performed with Nanosope III 5.12 software (Veeco, now Bruker AXS). RMS surface roughness measurements were performed on multiple 1 µm × 1 µm or larger scans at different sample positions. For PRs, the dominant surface texture wavelength was determined by 2D isotropic power spectral density analysis on multiple 3 µm × 3 µm or larger scans.

3.7 In situ Mass Spectrometry

A quadrupole mass spectrometer (PIC 300 quadrupole mass spectrometer, Hiden Analytical, Warrington, UK) was used in situ to monitor the neutral VUV photolysis products from photoresist materials and lipid A. The same mass spectrometer was also used for TIMS and described in Section 2.7. The maximum operating pressure for the channeltron detector is 5×10^{-6} Torr. When the Commonwealth ion source was in use, the chamber base pressure was well above the maximum operating pressure. Measurements of reaction products from radical exposures on lipid A have not been attempted because the radical-induced etch yield is low. Thus, in present studies, only photolysis products in the absence of ion bombardment and radical exposure were determined.

The spectrometer calibration was performed with hexafluoroethane (C_2F_6). The measured cracking pattern of C_2F_6 is shown in Figure 3.4a with CF (m/z = 31), CF_2 (m/z = 50), CF_3 (m/z = 69), and C_2F_5 (m/z = 119), consistent with the NIST database.[70] Before data acquisition, the ion source filament was degassed for 20 min and then set into standby mode (with a reduced filament current) for at least 1 h to reach thermal equilibrium in the ion source cage. The ionizer and quadrupole assembly was translated down, placing the ionizer about 1 cm proximity to the sample. The background spectrum was taken with sample in place before VUV was turned on. Under VUV exposure, the mass spectra in the range from 0.4 to 160 m/z were collected every 5 min with an increment of 0.2 m/z. The ionizing electron energy was set to 70 eV. To increase the concentration of photolysis products and therefore signal-to-noise ratio, the main gate valve between the chamber and the turbo pump was partially closed to reduce the effective pumping speed during measurements. The spectra acquisition and analysis were performed with MASsoft software (Hiden Analytical). The background gas signal (with VUV off) was stable throughout the measurement period, as shown in Figure 3.4b.

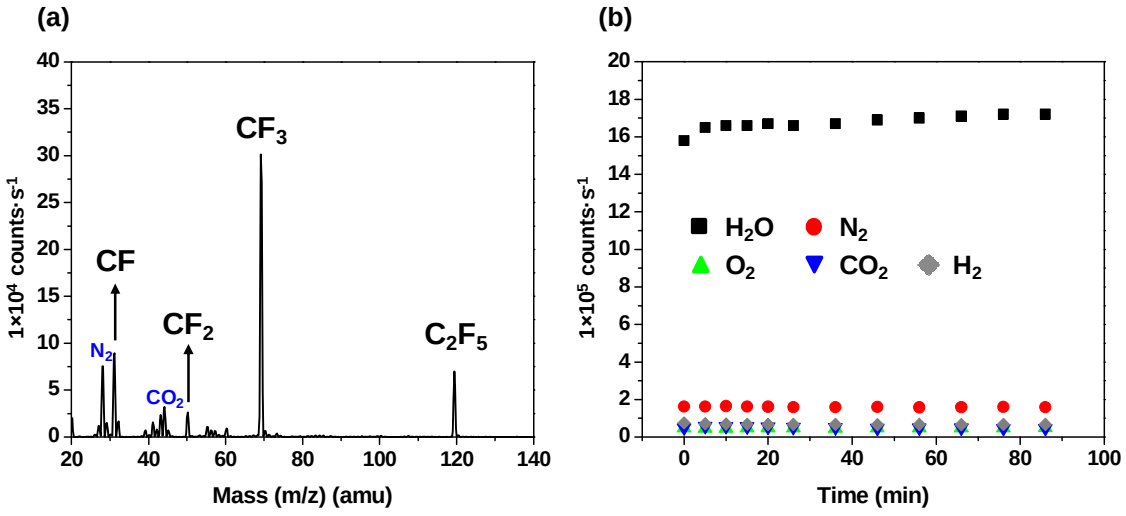

Figure 3.4 (a) The cracking pattern of C_2F_6 measured by the mass spectrometer. (b) The background gas signal over a 1.5 hr measurement span.

3.8 Quadrupole Time-of-Flight Mass Spectrometry

To obtain structural information of lipid A film bulk, unprocessed and VUV-exposed lipid A samples were analyzed using a quadrupole time-of-flight (Q-ToF) mass spectrometer (Q-ToF Premier, Waters, Milford, MA), located in QB3/Chemistry Mass Spectrometry Facility. The spectrometer was equipped with an electrospray ionization (ESI) source which was operated at atmospheric pressure. The measurements were assisted by Dr. Tony Iavarone.

ESI does not actively create ion fragments. Rather, it is a method to transfer analyte ions from a condensed liquid phase to gas phase. ESI is especially suitable for a wide range of biochemical compounds including peptides and proteins, lipids, oligosaccharides, etc. In principle, the spray capillary is held at a high electric potential with respect to a nearby counter electrode. Under the high electric field, the exiting electrolyte solution forms a "Talyor cone" and starts to eject a fine jet of liquid towards the counter electrode. The jet breaks up into a spray, where highly charged small droplets are separated apart by Coulombic repulsion. The polarity of ions in the droplets is determined by the polarity of the spray capillary. These droplets are further disintegrated by droplet jet fission, a process similar to jet injection from a Taylor cone. Finally, desolvated ions are liberated and directed into the mass analyzer through ion optics.[71]

In practice, spotted lipid A films (0.2 $mg \cdot ml^{-1}$, 10 μl) were resuspended in 200 μl solution of 74:23:3 chloroform:methanol:water to make the final lipid A concentration on the order of a few micromolar. Samples were infused from a 250-μL syringe (Hamilton, Reno, NV, USA) into the ESI probe at a flow rate of 5 $\mu L \cdot min^{-1}$ using a syringe pump. The connection between the syringe needle and the ESI probe was made using PEEK tubing (0.005-in. inner diameter × 1/16-in. outer diameter, Agilent, Santa Clara, CA). The ESI parameters were as follows: ESI capillary voltage 2.5 kV, nebulizing gas (nitrogen) flow rate 600 $L \cdot h^{-1}$, nebulizing gas temperature 150 °C, sampling cone voltage 100 V, extraction cone voltage 4 V, ion guide voltage 5 V, and source block temperature 80 °C. The ToF analyzer was operated in "V" mode. Under these conditions, a mass resolving power of 1.1×10^4 (measured at m/z = 1744) was achieved, which enabled resolution of the isotopic distributions of the ions measured in this study. Thus, an ion's mass and charge could be determined independently (i.e., the charge was determined from the reciprocal of the spacing between adjacent isotope peaks in the m/z spectrum). Mass calibration was performed prior to sample measurements using a solution of sodium formate. Mass spectra were recorded in the negative ion mode over the range m/z = 200-3000 for a period of one minute. Mass spectra were processed using MassLynx software (version 4.1, Waters).

3.9 Time-of-Flight Secondary Ion Mass Spectrometry

To obtain structural information of lipid A film surface, time-of-flight secondary ion mass spectrometry (ToF-SIMS) was performed with a secondary ion mass spectrometer (TOF.SIMS 5, ION-TOF USA, Chestnut Ridge, NY, USA), located at Beamline 9.0.2 of Advanced Light Source, Lawrence Berkeley National Laboratory. The measurements were assisted by Dr. Suet Yi Liu.

The spectrometer was equipped with a bismuth cluster primary ion source (Bi_3^+). The 25 keV primary ions impacted the sample surface by an incident angle of 45° and generated secondary ions and neutrals. The secondary ions were extracted into a reflectron time-of-flight (ToF) mass spectrometer. The SIMS spectra were acquired from an area of 150 μm × 150 μm and the total primary ion fluence was maintained to ensure static SIMS conditions for optimal sample surface analysis.

3.10 Human Whole Blood Tests

Endotoxic activity measurements are of critical importance in lipid A deactivation study. Earlier attempts applying the binding affinity between lipid A and LPS binding protein (LBP) were unsuccessful due to the low solubility of lipid A in aqueous solutions. Lipid A has to be deposited as a film in order to be processed in the vacuum beam system. The low solubility of lipid A in aqueous solutions makes resuspension of deposited film difficult. Moreover, incubating LBP solution directly with lipid A film on silicon substrate caused high background signal due to nonspecific binding between LBP and silicon. Various blocking agents were tested and improvements were minimal.

Human whole blood-based assay has been used by Rossi et al. to assess the endotoxic activity of lipid A and LPS deposited directly in 24-well plates.[72-75] As illustrated in Figure 3.5, cells of the innate immune system, such as monocytes and macrophages, can recognize LPS/lipid A through Toll-like receptor 4 (TLR-4) and protein complexes to initiate the secretion of a range of pro-inflammatory proteins (known as cytokines), including interleukin-1β (IL-1β), IL-6, and tumor necrosis factor-α (TNF-α).[34, 76, 77] The amount of secreted cytokines is proportional to the amount of LPS/lipid A, and thus it can be used to determine the endotoxic activity of LPS/lipid A. Advantages of human whole blood-based assay are as follows; first, blood can be directly applied to lipid A film and resuspension of lipid A is not necessary; second, it gives a direct measure of immune responses. The main drawback of this assay is that cytokine responses vary from donor to donor, and thus replicates with blood from multiple donors are necessary.[78] The protocol used in this study was developed based on Rossi's and optimized towards our application. General guidelines for cytokine measurement using whole blood can also be found in published protocols.[79]

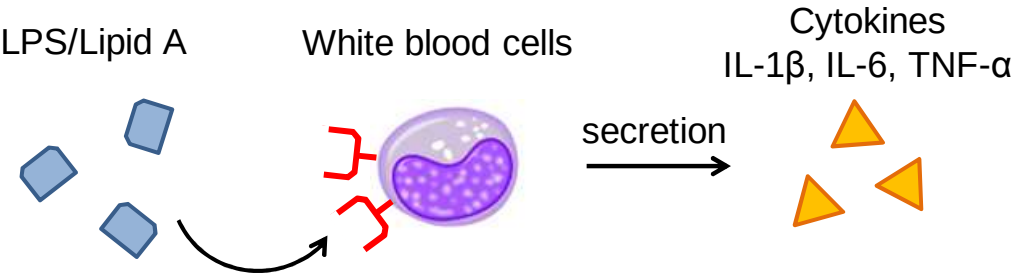

Figure 3.5 The principle of human whole blood-based tests. The concentration of secreted cytokines is a direct measure of LPS/lipid A endotoxic activity.

The basic protocol is shown in Figure 3.6. Heparinized fresh human whole blood was acquired from AllCells (Emeryville, CA, USA) and used within 6 h of collection. Samples were prepared by spotting serial diluted lipid A solution on UV/ozone-cleaned silicon substrates. These samples were placed into 24 well culture plates (Nunc Multidishes Nunclon™Δ, Nalge Nunc International, Rochester, NY, USA). 0.5 ml of fresh human whole blood was pipetted into each well. The samples were incubated in a 37 °C, 5% CO_2 incubator for 24 h. After incubation, supernatants were collected after centrifugation for 10 min at 400×g and stored at -20 °C until interleukin contents were determined. Among other pro-inflammatory proteins, we chose to monitor IL-1β concentration in this study. IL-1β measurements were performed by a commercial enzyme-linked immunosorbent assay (ELISA) from Life Technologies (Grand Island, NY, USA). For each donor, a standard curve was constructed by incubating blood with serial dilution of spotted lipid A/silicon samples. We note that lipid A film is not readily soluble in blood. Thus, this assay mainly monitors the endotoxic activity of lipid A film surface.

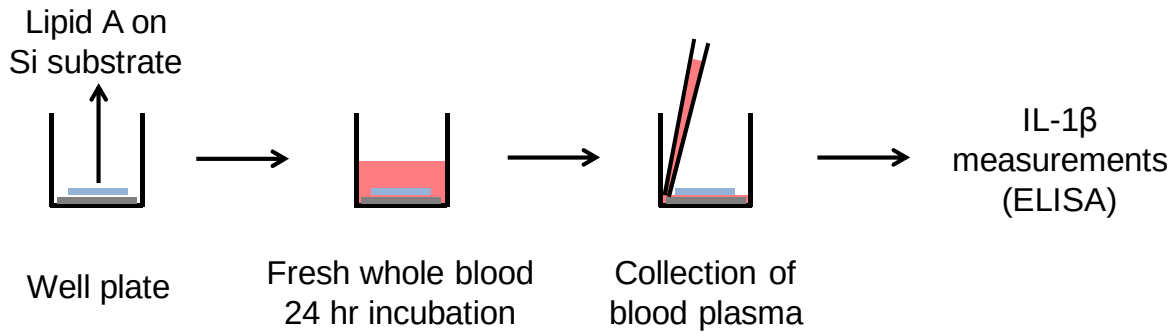

Figure 3.6 The protocol of human whole blood-based tests.

Chapter 4

Ion, VUV, and Electron Effects in 193 nm Photoresist Surface Roughening

4.1 Abstract

Previous studies in our group and with our collaborators showed a synergistic effect of ion bombardment, vacuum ultraviolet (VUV) irradiation and moderate substrate heating in 193 nm photoresist (PR) surface roughening.[80-82] This chapter presents a summary of the individual effect of 150 eV Ar ion bombardment, 147 nm VUV photon irradiation, and the synergism of simultaneous ion/VUV exposure in enhanced surface roughening of 193 nm PR. Furthermore, the effects of 1 keV electrons and various combinations of ions, VUV photons, and electrons are discussed. The results suggest that enhanced roughening of 193 nm PR is initiated by the synergistic interaction between an ion bombardment-induced carbon-rich surface layer (~2 nm) and a scissioned bulk layer (~100 nm).

4.2 Introduction

Severe degradation and roughening of 193 nm photoresist (PR) in plasma etch processes hinder the continuous scaling of semiconductor devices. Current understanding of plasma-polymer interactions during plasma etch for nanoscale fabrication was recently reviewed by Oehrlein et al.[83] Various studies investigated the effects of polymer structures and plasma parameters, such as plasma chemistry, power, and pressure in 193 nm PR roughening under various plasma conditions.[11-15] For example, micromasking, fluorocarbon deposition, and polymer surface fluorination by gas phase fluorine have been attributed to the roughening of PR in fluorocarbon-containing plasmas. [13-15] Furthermore, studies showed that, even without complex plasma gas chemistry, pure Ar plasma exposures still resulted in substantial roughening of 193 nm PR.[15] The active species in a pure Ar plasma are energetic ions, photons, and electrons. This chapter will be devoted to the individual and synergistic effects of ions, vacuum ultraviolet (VUV) photons, and electrons in surface roughening of 193 nm PR.

In a pure Ar plasma, Ar ions accelerate across the thin sheath region and bombard the material perpendicular to the sample surface. Material is removed anisotropically due to the directionality of ions. The ion energy is usually controlled by the applied bias voltage on the

sample, typically a few hundred electron volts (eV). Titus et al. showed that in an inductively coupled Ar plasma, PR surface roughening was highly correlated to the Ar ion energy.[82] When the ion bombarding energy was below ~65 eV, PR surface remained smooth; however, enhanced surface roughness was observed when the ion energy was increased beyond 65 eV and reached a maximum ~150-175 eV. This was attributed to the formation of a carbon-rich layer at the PR surface with an ion energy higher than 65 eV. Details of ion-induced modification will be further discussed in Section 4.4.

Low-pressure plasmas also generate photons in a broad range, from visible light to VUV (λ < 200 nm). Light emission spectra from technologically important plasmas have been presented in literature.[84-87] For an Ar plasma, two intense resonance lines are at 104.8 and 106.7 nm. All hydrocarbon polymers absorb in the VUV region with absorption coefficients several orders of magnitude higher than that in the ultraviolet (UV) region.[88] Thus, VUV photochemistry with PRs has lately drawn increasing attention in the etching community. To minimize PR degradation, some plasma pre-etch treatments have been observed to "cure" the 193 nm PR after the development stage.[89-91] These plasma pre-etch treatments, for example exposures to HBr- and H_2-containing plasmas, are designed to decrease the roughening and increase etch resistance of 193 nm PR during the subsequent plasma etch steps. Pargon et al. pointed out that VUV (λ ~110-210 nm) photons generated by plasmas contribute to the smoothing effect of plasma pretreatments and plasma chemistry plays a key role in both surface and sidewall roughening.[92, 93] On the other hand, Nest et al. showed in vacuum beam experiments that simultaneous 150 eV Ar ion bombardment, VUV irradiation and moderate substrate heating of 193 nm PR lead to enhanced PR surface roughness.[80, 81] The degree of surface roughening observed in vacuum beam experiments is similar to that following inductively-coupled Ar plasma exposure under similar ion/VUV fluences and energies.[82] The VUV effect and its synergy with ion bombardment and electron exposure will be further presented in Section 4.5, 4.6, and 4.8.

Compared to positive ions bombarding the substrate with energies of several hundred eVs, electrons only reach the substrate when the instantaneous sheath potential drops to nearly zero. These escaping electrons bearing low energy, usually no more than a few eVs, balance the ion charge built-up on insulating substrates.[1] Evidence has shown that electrons with energies below 100 eV can damage polymers as high energy electrons. For example, formation of unsaturated C=C bonds in poly (methyl methacrylate) (PMMA) film has been reported.[94, 95] However, since the penetration depth of these electrons is comparable to ions (~few nanometers) during plasma processes, the electron-induced PR modification is generally ignored by the etching community.[96, 97] Some configurations of plasma chambers can result in high energy electrons bombarding the surfaces along with other plasma species. As shown in Figure 4.1, a negatively direct current (DC)-biased upper electrode attracts ions and generates secondary electrons. The secondary electron yields of various electrode materials under plasma conditions have been measured by En et al.[98] For example, under 1.5 keV Ar ion bombardment, the secondary electron yield of single crystal silicon is about 0.7, which is not negligible. These secondary electrons accelerate through the sheath with energies in the keV range and can easily reach the lower electrode, on which the processing wafer is located. These electrons can easily penetrate the PR and cause damage. Electron pretreatment with a few keVs of energy has been proposed for 193 nm PR to increase the etch resistance and reduce the shrinkage under critical dimension measurements.[99-101] Observation of reduced surface roughness under SEM was

also reported.[101] These authors attributed the results to either cross-linking or scissioning of the polymer under electron exposure. The effect of 1 keV electrons and its synergy with ion bombardment and VUV irradiation will be the focus of Section 4.7-8.

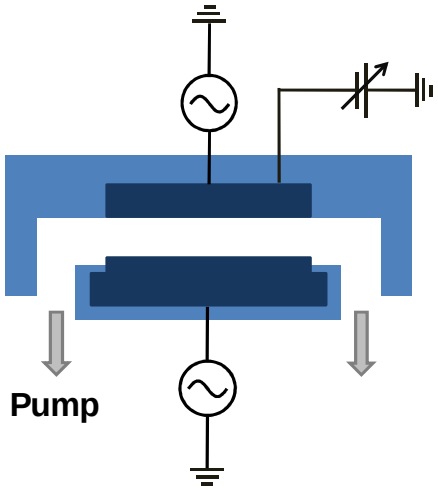

Figure 4.1 Schematic of a discharge chamber with a negatively DC-biased upper electrode. The substrate sits on the bottom electrode.

In summary, we will demonstrate that the synergism between plasma-generated species and substrate heating is of critical importance in 193 nm PR surface roughening. Enhanced surface roughness is observed with a combination of an ion-modified surface layer and a scissioned bulk layer, either by VUV photon irradiation or low-fluence electron exposure. A bi-layer wrinkling mechanism can be used to qualitatively interpret the observed synergy.

4.3 Experimental Setup

The details of the beam system are described in Chapter 2. The beam sources used in this study were the ion source, the VUV source, and the electron source. The schematic of the system setup is shown in Figure 4.2. The 150 eV Ar ion current at the sample position was measured with Faraday cup 1 (aperture size ~4.55×10^{-4} cm^2). An ion current of 2.8×10^{14} $ions\cdot cm^{-2}\cdot s^{-1}$ (±10%) was used and a 1 h exposure resulted in an ion fluence of 1.0×10^{18} $ions\cdot cm^{-2}$ (±10%). The 147 nm VUV photon flux irradiating on the sample surface was ~1.34×10^{14} $photons\cdot cm^{-2}\cdot s^{-1}$, corrected by an incidence angle of 45° to the surface normal. 1 h VUV irradiation resulted in a photon fluence of 4.8×10^{17} $photons\cdot cm^{-2}$. The 1 keV electron current at the sample position was measured with Faraday cup 2 (aperture size ~19.6×10^{-4} cm^2). Different electron fluences were achieved by changing the electron current. The in situ etch yield was monitored with quartz crystal microbalance (QCM). The bulk chemical modification was characterized with ex situ transmission Fourier transform infrared (FTIR) spectroscopy. The surface morphology of samples was imaged by atomic force microscopy (AFM) in tapping mode. Root mean square (RMS) surface roughness measurements were performed on multiple AFM scans at different sample positions.

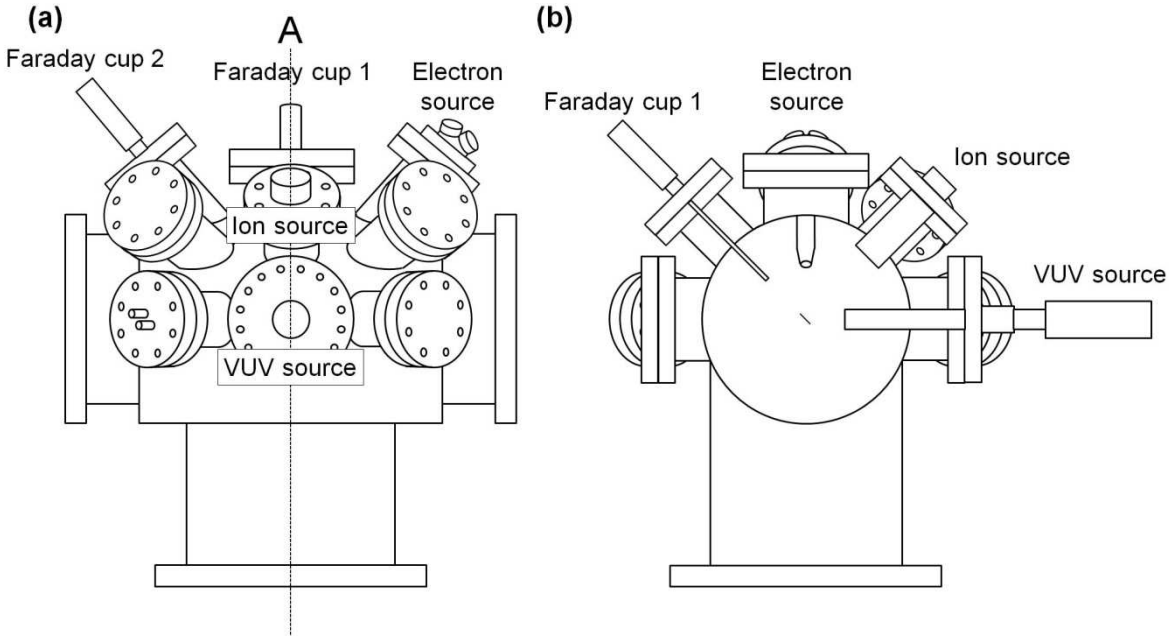

Figure 4.2 (a) Side view of the beam system (b) cross section view of the beam system at plane A labeled in (a).

4.4 Ar Ion Bombardment on 193 nm Photoresist

150 eV Ar ion bombardment on methacrylate-based PRs results in physical sputtering, near-surface region modification, and formation of a surface carbon-rich layer. Studies of Ar plasma and Ar ion bombarded polymers suggest that the surface becomes highly carbon-rich and cross-linked under steady state conditions.[102-108] Koval reported suspending a graphitized/cross-linked layer formed on PMMA surface after 250 eV Ar ion bombardment.[106] Nest et al. also showed a dramatic decrease of sputtering yield (by a factor of ~100 for 150 eV Ar ions) on 193 nm PR at a fluence of ~1.0×10^{16} ions·cm^{-2}, corresponding to the formation of this modified layer.[81] These results are supported by molecular dynamic (MD) simulations coupled with ellipsometry measurements following plasma exposures, showing that the thickness of the ion-modified layer is about 1.5-2 nm with a density of about 1.8-2.4 g·cm^{-3}.[109, 110] The density is similar to that of tetrahedral amorphous carbon (ta-C) films grown by depositing carbon ions or Ar ion plating at comparable ion energy. Correlations between the density of amorphous carbon films and its intrinsic compressive stress have been reported. It is thus expected that the ion-modified surface layer is under an analogous intrinsic compressive stress, roughly on the order of a few GPa.[111-113] In a recent publication, by AFM force curve measurements coupled with numerical finite element simulations, Lin et al. reported that the ion-modified layer, formed on polystyrene (PS) film by Ar ion bombardment in an Ar plasma, bore an elastic modulus more than 2 orders of magnitude higher than that of pristine PS. [114] This observation was based on the bi-layer wrinkling theory, which will be further discussed in Section 4.6.

In this study, an ion current of 2.8×10^{14} ions·cm^{-2}·s^{-1} (±10%) was used. The total ion fluence after 1 h of ion bombardment was ~1.0×10^{18} ions·cm^{-2}·s^{-1}(±10%). We note that the ion flux used in a beam exposure is lower compared to typical plasma etch conditions. Formation of the ion-modified layer takes roughly 0.5-1 min in a beam experiment and roughly 2-5 s in an Ar plasma exposure.[108] With the formation of the ion-modified surface layer, the surface roughness of 193 nm PR increases after ion bombardment to ~1.58 nm at 25 °C and ~2.25 nm at 65 °C. The corresponding AFM images are shown in Figure 4.3.

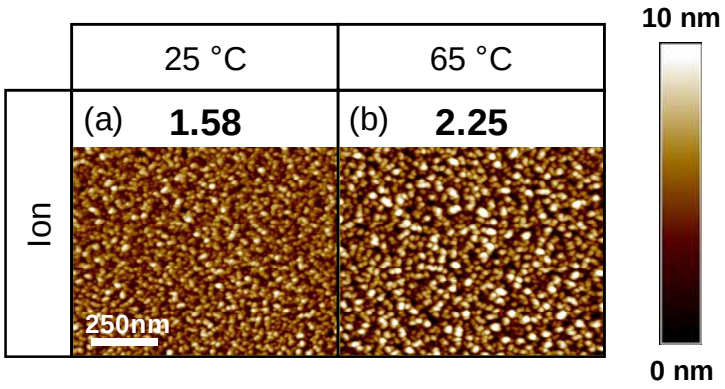

Figure 4.3 1 µm × 1 µm AFM images of 193 nm PR after 150 eV Ar ion bombardment at (a) 25 °C, (b) 65 °C. The Ar ion fluence was 1×10^{18} ions·cm^{-2}. The color scale of the images is 10 nm.

4.5 VUV Irradiation on 193 nm Photoresist

It has been shown that VUV photons, generated by closed-volume lamp sources or plasmas, can cause bulk modification of 193 nm PR. The change is typically observed with transmission FTIR. [13, 89-91, 93] Figure 4.4 shows the FTIR spectra of 193 nm PR after 147 nm VUV exposure. The exposure time ranged from 5 min to 1 h, and the photon fluence ranged from 4.0×10^{16} to 4.8×10^{17} photons·cm^{-2}. The substrate temperature was held at 65 °C.

FTIR absorption peak loss is observed in the C=O (1675-1850 cm^{-1}) and C-O-C region (1050-1350 cm^{-1}), showing the removal of ester linkages (1720 and 1738 cm^{-1}) and lactone groups (1796 cm^{-1}). The loss of oxygen-containing moieties is in the form of gaseous products, which will be presented in Chapter 5.[115, 116] The rise of the peak at 1772 cm^{-1} can be attributed to multiple origins, including the detached lactones that remain in the film, the presence of carboxylic acids, or formation of aldehydes.[90, 93, 117] The penetration depth of 147 nm VUV photons is roughly estimated to be ~100 nm, based on the loss fraction of C=O and C-O-C characteristic peaks. This is consistent with the penetration depth of VUV photons in polymeric materials, from 15 to 250 nm, depending on VUV wavelength and polymer structure.[118] Based on the damage of oxygen-containing moieties, the saturation of VUV penetration in methacrylate-based PR has been simulated and verified by experiments.[119] In contrast, little change is observed in the CH_2/CH_3 region (2800-3100 cm^{-1}). VUV photons

generated by Ar, HBr or fluorocarbon-containing plasmas have similar effects on 193 nm PR. [50, 93]

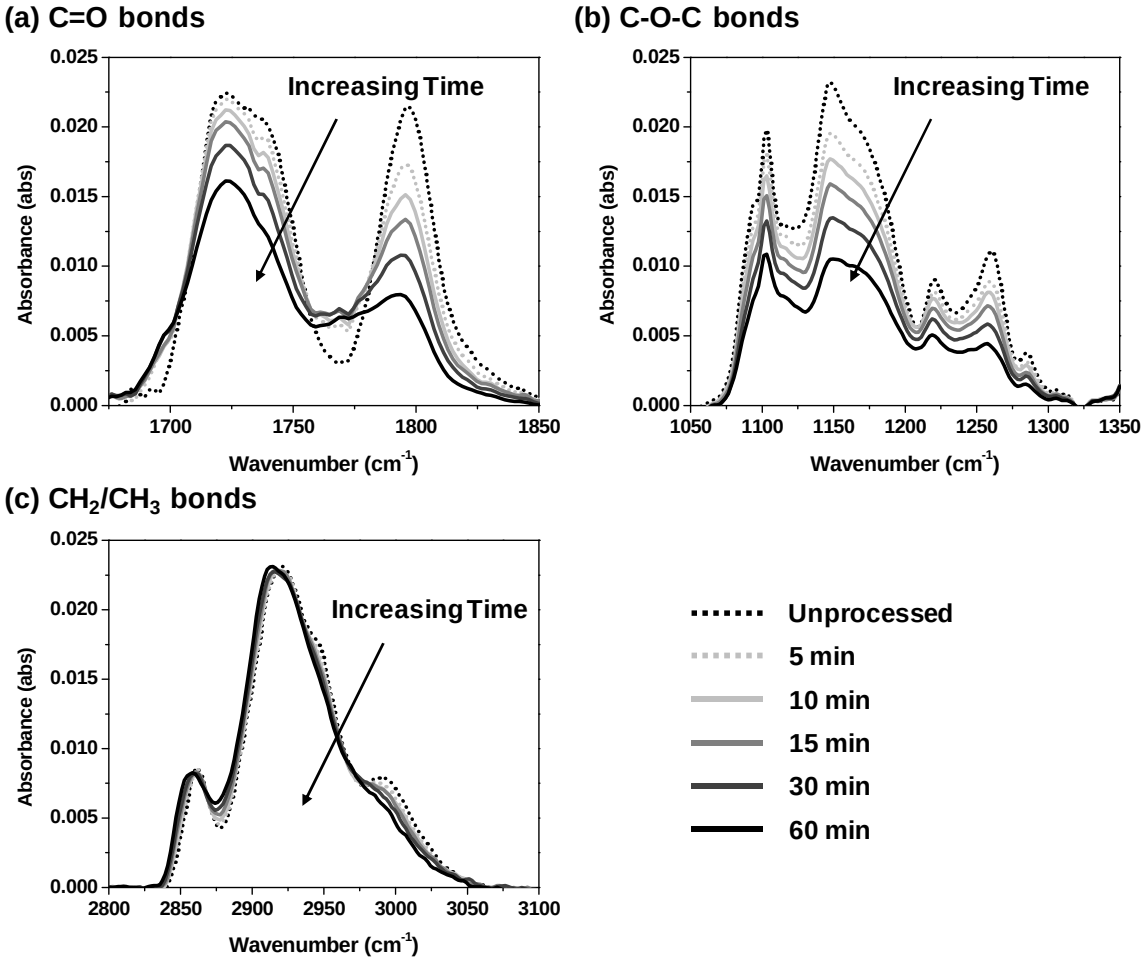

Figure 4.4 Transmission FTIR spectra of 193 nm PR after 147 nm VUV photon irradiation with a flux of 1.34×10^{14} photons·cm^{-2}·s^{-1}. (a) C=O bonds (1675-1850 cm^{-1}) (b) C-O-C bonds (1050-1350 cm^{-1}) (c) CH_2/CH_3 bonds (2800-3100 cm^{-1}).

Besides the observed bulk-modification through FTIR, Pargon et al. provided experimental evidence that after plasma-generated VUV exposure, the glass transition temperature (T_g) of 193 nm PR decreased from 170 to ~110 °C.[93] The T_g is the temperature at which the polymer undergoes the transformation from a glassy state to a rubbery state upon heating. A decreased T_g refers to a higher degree of molecular motion and a lower elastic modulus of VUV-exposed PR. It is suspected that detached free lactone and adamantyl group may stay in the film and act as a plasticizer to soften the film.[90, 93] Also, main chain scissioning could take place and thus decrease the T_g of the polymer matrix. In a recent publication, Pargon et al. observed cross-linking of 193 nm PR resulting from extended HBr plasma-generated VUV exposure. [117] Under their experimental setup, VUV-processed 193 nm PR was soluble in acetone with an exposure time less than 60 sec, but insoluble in acetone if the

exposure was extended to beyond 60 sec. Their observation suggests that VUV-induced modification is dependent on photon fluence. The photon fluence used in our study is believed to be within the VUV-induced scissioning region, supported by the fact that exposed-PR is soluble in tetrahydrofuran (THF).

In spite of the above-mentioned chemical and mechanical changes of the polymer, the surface roughness of 193 nm PR after 147 nm VUV exposure is consistently smooth at ~0.3 nm, comparable to an unprocessed film. AFM images of 147 nm VUV-exposed 193 nm PR are shown in Figure 4.5.

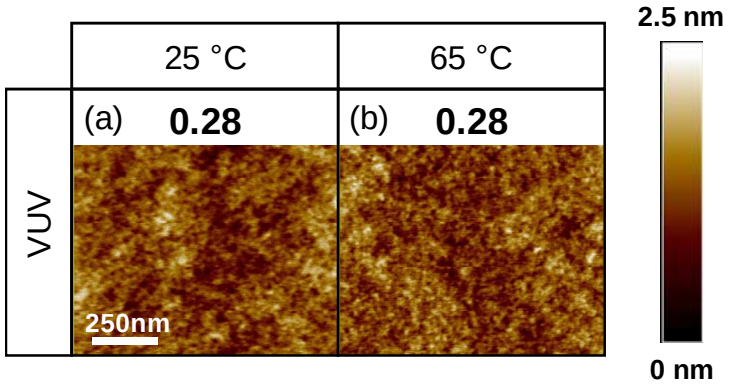

Figure 4.5 1 µm × 1 µm AFM images of 193 nm PR after 147 nm VUV photon irradiation at (a) 25 °C, (b) 65 °C. The VUV fluence was 4.8×10^{17} photons·cm^{-2}. The color scale of the images is 2.5 nm.

4.6 Simultaneous Ion and VUV Exposure on 193 nm Photoresist

The AFM images of 193 nm PR after simultaneous ion/VUV exposures are shown in Figure 4.6. Simultaneous exposure provides the combination of an ion-modified, carbon-rich surface layer on top of a VUV-modified bulk layer. The surface roughness of simultaneous ion/VUV-exposed polymer is comparable to that of pure Ar plasma-processed PR at a similar substrate temperature, ion energy and fluence.[82] Nest et al. demonstrated that this observation is valid with different VUV sources, and the surface roughness of processed PR increases with increasing VUV photon fluence and substrate temperature.[80, 81] These results suggest that the mechanical difference between the ion-modified layer and the VUV-modified layer is the key factor for surface roughening of 193 nm PR under plasma conditions. The schematic summary of ion-only, VUV-only, and simultaneous ion/VUV exposure is shown in Figure 4.7.

It is well known that the combination of a compressively stressed film and a compliant substrate can result in complex wrinkle formation. Various studies have been devoted to constructing such bi-layer systems and characterizing the resulting surface morphology. Metal, SiO_2 or Si thin films deposited or otherwise induced to form on polydimethylsiloxane (PDMS) can result in wrinkling upon cooling or releasing the pre-strained PDMS underlayer.[120-125] Wrinkles are also observed by deposition of aluminum on PS films heated above its glass

transition temperature, and by sputtering SiO_2 on PMMA at about 50 °C.[126, 127] The responsible mechanism has been generally understood to be a stress-driven instability.[128-130] Upon wrinkling, the elastic top layer undergoes both in-plane and out-of plane displacement to relax the compressive stress, and the compliant underlayer deforms concurrently.

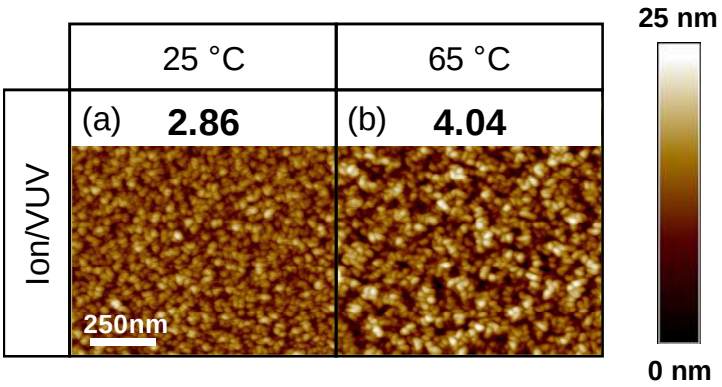

Figure 4.6 1 µm × 1 µm AFM images of 193 nm PR after simultaneous 150 eV Ar ion and 147 nm VUV photon exposure at (a) 25 °C, (b) 65 °C. The Ar ion fluence was 1×10^{18} ions·cm^{-2} and the VUV fluence was 4.8×10^{17} photons·cm^{-2}. The color scale of the images is 25 nm.

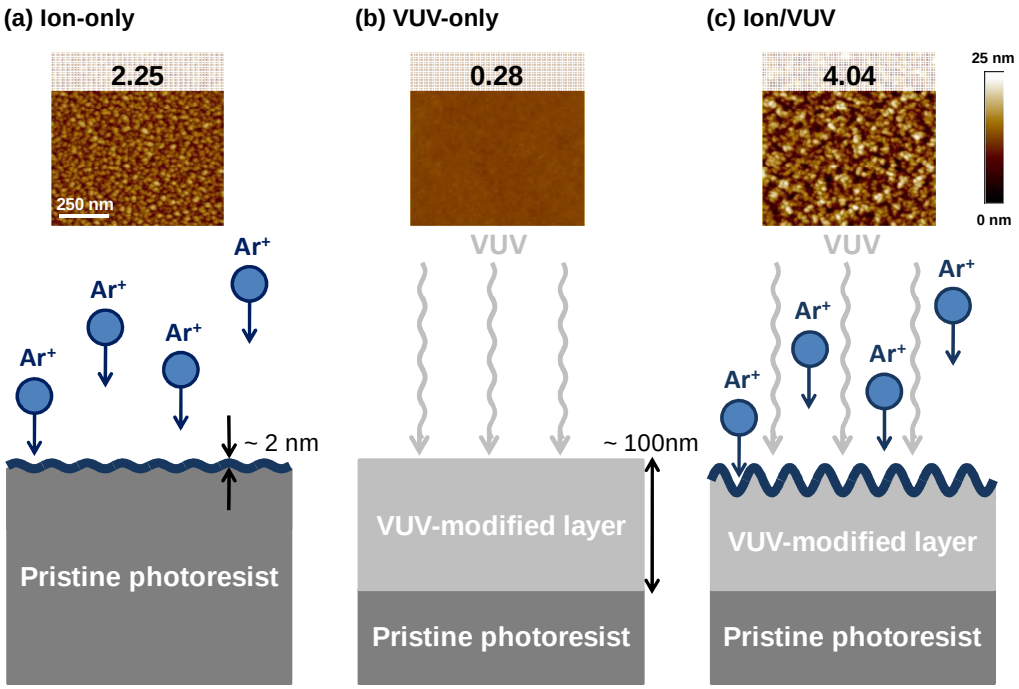

Figure 4.7 A summary of species effects on 193 nm PR and corresponding 1 µm × 1 µm AFM images after processed at 65 °C for (a) 150 eV Ar ion, (b) 147 nm VUV, (c) simultaneous ion/VUV. The color scale of the AFM images is 25 nm.

Bruce et al. have suggested this buckling/wrinkling mechanism to explain nanoscale surface roughening of polymers under plasma etch conditions.[131] The onset of wrinkling requires that the compressive stress exceeds the value of critical stress, σ_c, which is determined by the mechanical properties of the two layers. If both layers are assumed to be elastic, σ_c is

$$\sigma_c = -\frac{E_f}{4\left(1-\nu_f^2\right)}\left[\frac{3E_s\left(1-\nu_f^2\right)}{E_f\left(1-\nu_s^2\right)}\right]^{2/3} \tag{4.1}$$

where E is the elastic modulus, v is the Poisson's ratio, and subscripts f and s denote the stiff overlayer and compliant underlayer, respectively.

In the small deformation limit, the equilibrium amplitude, A, and wavelength, λ, can be readily derived as shown here:

$$A = h\left(\frac{\sigma}{\sigma_c}-1\right)^{1/2} \tag{4.2}$$

$$\lambda = 2\pi h\left[\frac{E_f\left(1-\nu_s^2\right)}{3E_s\left(1-\nu_f^2\right)}\right]^{1/3} \tag{4.3}$$

where h is the thickness of the top layer.

Bruce et al. conducted the experiments on PS. After Ar ion bombardment, an ion-modified surface layer was formed on the PS film. By changing ion energy, the thickness of the ion-modified surface layer was seen to change. It was shown that the experimental values for equilibrium amplitude (roughness) and wavelength were in good agreement with calculated theoretical values.

We note that both amplitude and wavelength are proportional to $E_s^{-1/3}$, where E_s is the elastic modulus of the compliant underlayer. As simultaneous ion/VUV exposure renders a bi-layer structure to methacrylate-based PR, we adopt the wrinkling theory to further study the roughening of 193 nm PR. The following sections will present the results of 1 keV electron-only exposures and various combinations of ions, VUV photons, and electrons.

4.7 1 keV Electron Exposure on 193 nm Photoresist

The transmission FTIR spectra of 193 nm PR after 1 keV electron exposure are shown in Figure 4.8.

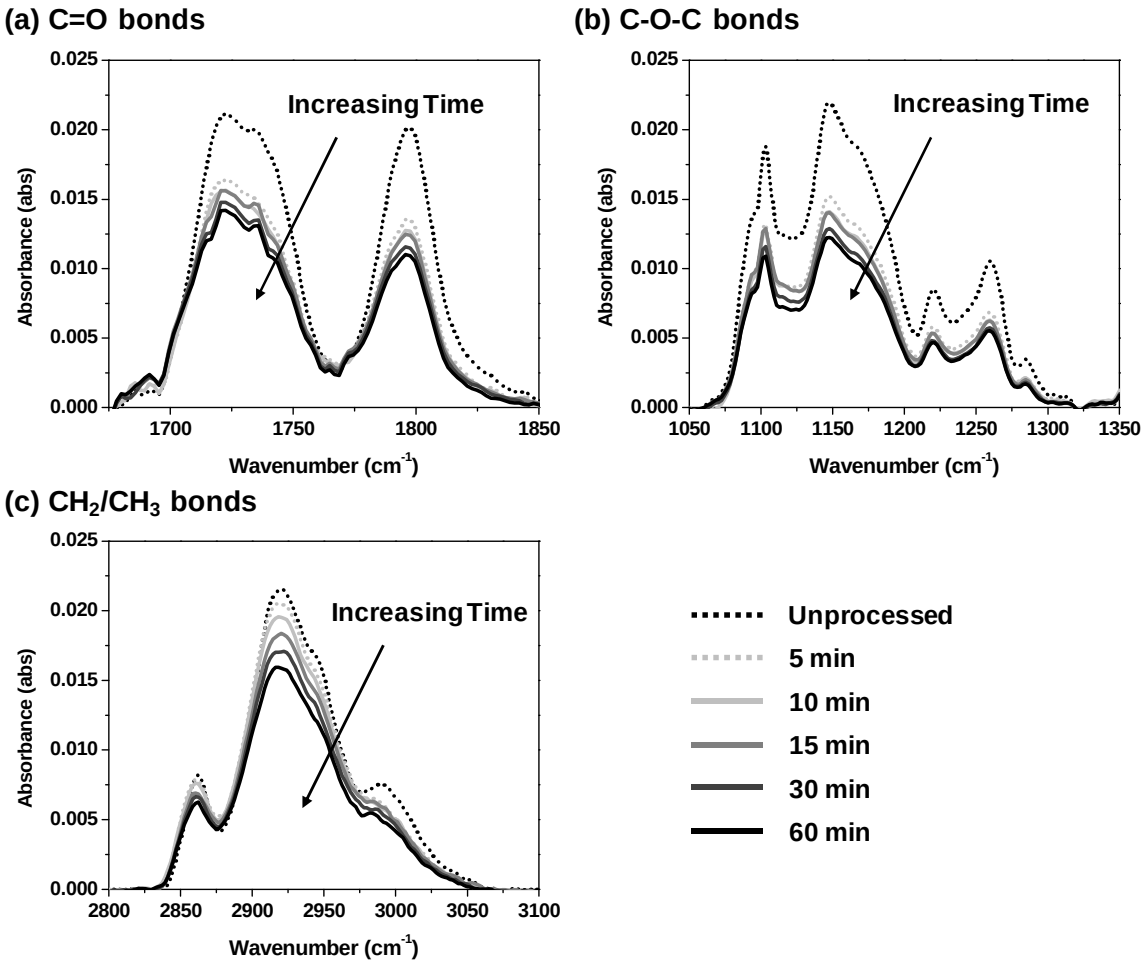

Figure 4.8 Transmission FTIR spectra of 193 nm PR after 1 keV electron exposure with a flux of 9.8×10^{12} electrons·cm^{-2}·s^{-1}. (a) C=O bonds (1675-1850 cm^{-1}) (b) C-O-C bonds (1050-1350 cm^{-1}) (c) CH_2/CH_3 bonds (2800-3100 cm^{-1}). The substrate temperature was 65 °C.

The electron flux was maintained at 9.8×10^{12} electrons·cm^{-2}·s^{-1} with exposure time ranging from 5 min to 1 h, resulting in electron fluences from 0.47 to 5.6 mC·cm^{-2}, respectively. The substrate temperature was held at 65 °C. For electron-only exposure, FTIR absorption peak loss is observed in the C=O, C-O-C and CH_2/CH_3 regions. Based on the loss fraction of absorption peaks, we estimate 1 keV electrons can penetrate 193 nm PR to a depth of ~100 nm, which is consistent with reported electron ranges in PMMA. [132] It is worth noting that the

damage occurs within each region under a different time scale. In oxygen-containing regions (Figure 4.8a and b), the high rate of loss in the first 5 min is attributed to the depletion of oxygen within the penetration depth of electrons. The loss of oxygen-containing bonds saturates after ~30 min (2.8 mC·cm^{-2}) and is most likely in the form of gaseous products such as CO and CO_2.[133] In the CH_2/CH_3 region (Figure 4.8c), the main peak decreases gradually with increasing electron fluence. The peak loss mainly corresponds to the loss of hydrogen from the polymer, probably resulting in formation of H_2 and small amounts of CH_4.[133] Electron-only exposures conducted at 25 °C show similar loss of FTIR absorption peaks with a slightly decreased loss fraction. The temporal evolution of normalized absorption peak loss for CH_2 (asymmetric stretching, 2920 cm^{-1}), ester (C=O stretching, 1722 cm^{-1}) and lactone (C=O stretching, 1797 cm^{-1}) is shown in Figure 4.9.

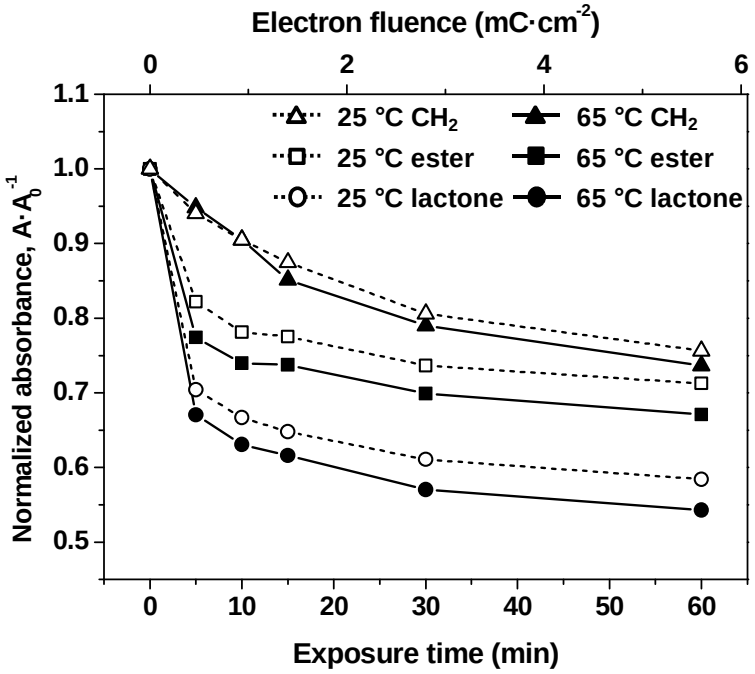

Figure 4.9 Normalized absorbance of CH_2 asymmetric stretching (2920cm^{-1}), C=O ester (1722 cm^{-1}), and C=O lactone (1797 cm^{-1}) for different 1 keV electron exposure time. The substrate was maintained at 25 and 65 °C for hollow and solid symbols, respectively.

An in situ QCM measurement of 193 nm PR under 1 keV electron exposure is shown in Figure 4.10. The electron flux was 1.26×10^{13} electrons·cm^{-2}·s^{-1}. Exposure time and corresponding electron fluence are both labeled. The slope of the QCM curve is proportional to the instantaneous etch yield. A high initial etch yield (for fluences < 1 mC·cm^{-2}) is followed by a decreased steady-state etch yield (for fluences > 3 mC·cm^{-2}). In accordance with the FTIR results, the initial high etch yield is due to the rapid formation of oxygen-containing gaseous products. The steady-state etch yield is mainly due to the abstraction of hydrogen.

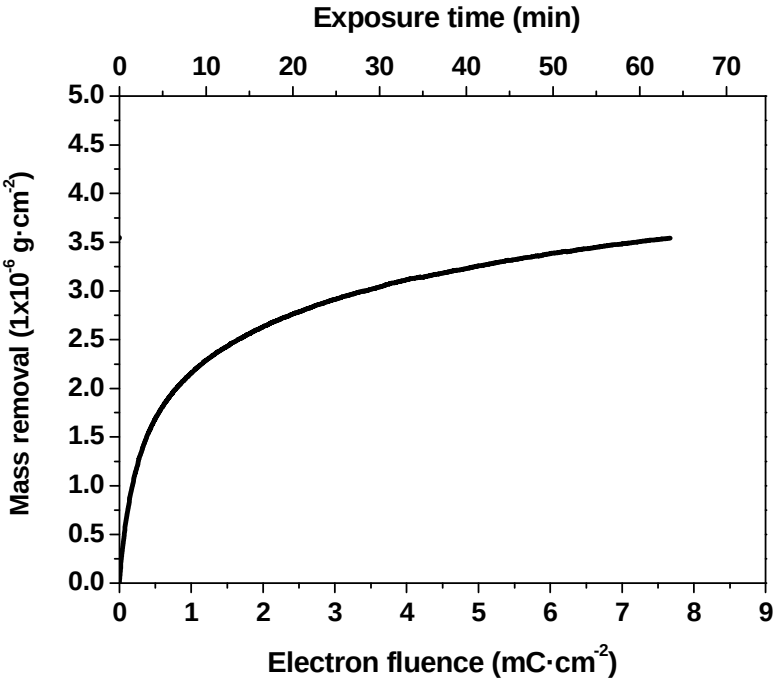

Figure 4.10 In situ QCM measurement of 193 nm PR under 1 keV electron exposure at room temperature. A high initial etch yield (< 1 mC·cm^{-2}) is followed by a decreased steady-state etch yield (> 3 mC·cm^{-2}).

From electron beam resist studies, it is known that low fluence electron beams induce scissioning of PMMA while higher electron fluences induce cross-linking.[134-136] Because 193 nm PR is a methacrylate-based polymer, a similar behavior under electron irradiation is expected. Chen et al. have shown that linear acrylic 193 nm PR can be used to produce both "positive" and "negative" patterns by 40 keV electron irradiation.[137] Under low electron fluences, the T_g of the bulk polymer decreases and 193 nm PR behaves as a "positive-tone" electron resist. In contrast, under high electron fluences, 193 nm PR acts as a "negative-tone" resist where cross-linked networks form, and the T_g rises above that of the virgin polymer. We observe that low fluence, 1 keV electron-irradiated PRs are soluble in THF (< 1 mC·cm^{-2}), while higher fluences leave insoluble, cross-linked films on the silicon substrate (> 4 mC·cm^{-2}). This trend agrees with both the in situ QCM measurement and FTIR spectra. The fast removal of oxygen-containing bonds results in the bulk scissioning of 193 nm PR, and the following abstraction of hydrogen enhances the recombination of broken bonds. Thus, electron-induced cross-linking, within the penetration depth, begins to dominate when the etch yield starts to decrease.

For electron-only exposure with various fluences, the RMS surface roughness of 193 nm PR remains low, about 0.4 nm, similar to that of unprocessed films (~0.3 nm), as shown in Figure 4.11.

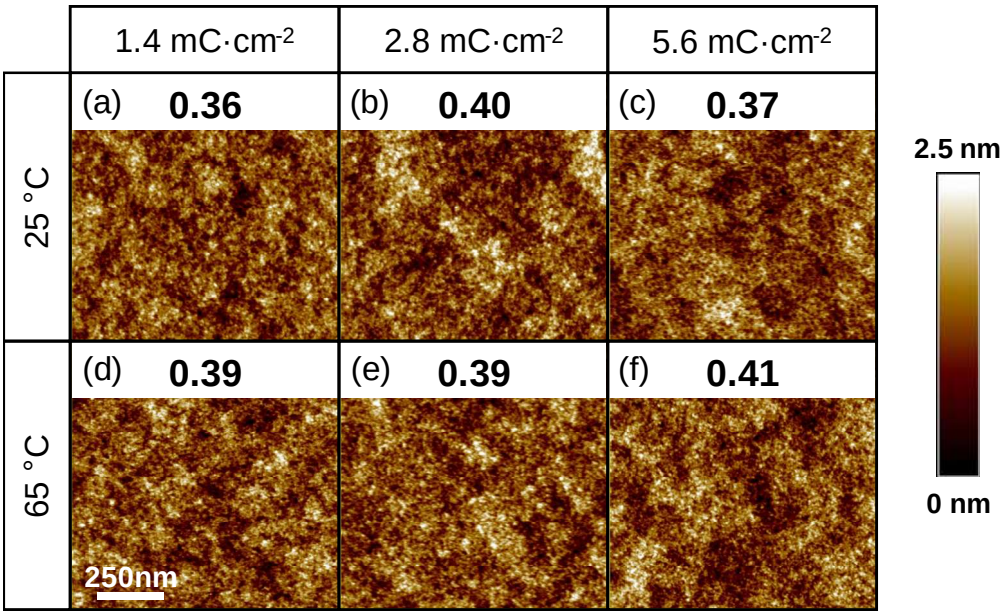

Figure 4.11 1 µm × 1 µm AFM images of 193 nm PR after 1 keV electron exposure. (a), (b), and (c) were conducted at 25 °C with various electron fluences; (d), (e), and (f) were conducted at 65 °C with various electron fluences. The color scale of the images is 2.5 nm.

4.8 Simultaneous Ion, VUV, and Electron Effects on 193 nm Photoresist

In the beam system, experiments were conducted with (1) simultaneous VUV/electron exposure; (2) simultaneous ion/electron exposure; (3) simultaneous ion/VUV/electron exposure, with each exposure conducted at both 25 and 65 °C. For exposure protocols (1)-(3), the exposure time was 1 h, resulting in an ion fluence of 1×10^{18} ions·cm^{-2} and a VUV fluence of 4.8×10^{17} photons·cm^{-2}. Different electron fluences were achieved by changing the electron flux. The surface roughness of 193 nm PR resulting from various exposure protocols is shown in Figure 4.12. The corresponding AFM images are shown in Figure 4.13 and 4.14 for samples processed at 65 and 25 °C, respectively.

The surface roughness of simultaneous VUV/electron exposures is relatively low, about 0.4 nm. Although electrons can induce either scissioning or cross-linking to a depth of ~100 nm, none of the electron-only or simultaneous electron/VUV exposures increase surface roughness. Bulk modification alone is not sufficient to roughen the PR surface.

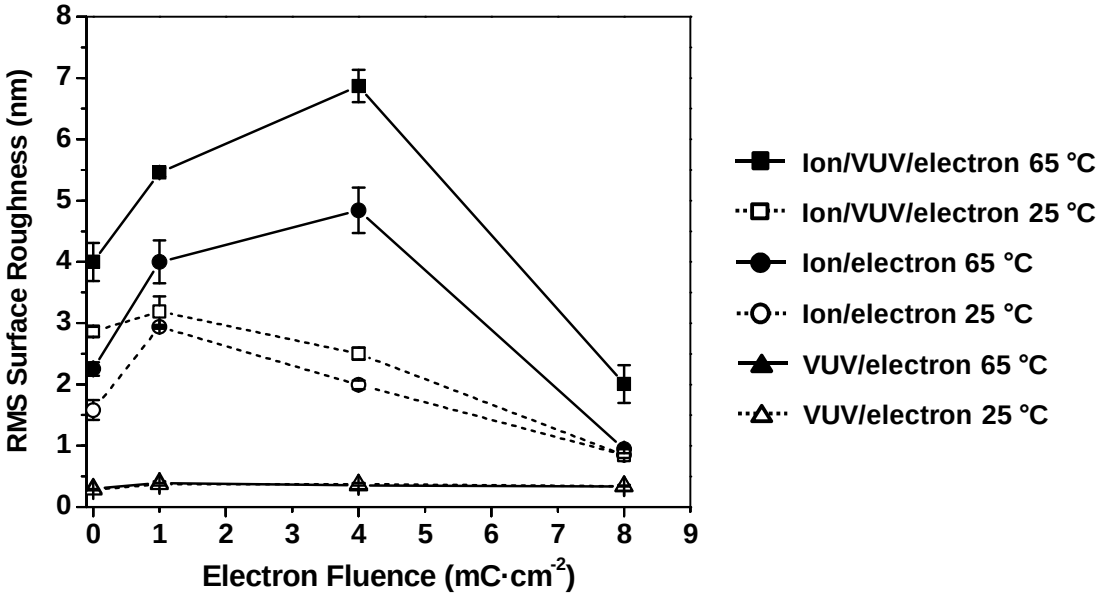

Figure 4.12 RMS surface roughness of 193 nm PR resulting from various exposure protocols: simultaneous ion/VUV/electron (■ 65 °C, □ 25 °C), simultaneous ion/electron (● 65 °C, ○ 25 °C) and simultaneous VUV/electron (▲ 65 °C, Δ 25 °C).

As mentioned in earlier sections, energetic ion bombardment is essential for enhanced surface roughening. It is stressed here that at 65 and 25 °C, the surface texture and roughness of simultaneous ion/low fluence electron (1 mC·cm^{-2}) is comparable to that of simultaneous ion/VUV exposure (Figure 4.12). Based on the bi-layer wrinkling theory, the amplitude (roughness) is proportional to $E_s^{-1/3}$, where E_s is the elastic modulus of the compliant underlayer. A lower E_s will increase the roughness, while a higher E_s will reduce the roughness. Both VUV photons and low fluence electrons cause bulk scissioning in the irradiated polymer and decrease its bulk T_g and elastic modulus E_s.[93, 136-138] A compressively stressed, ion-modified surface layer on top of a compliant bulk layer is suggested to initiate the observed surface roughness. In contrast, bulk cross-linking induced by high fluence electrons increases the elastic modulus of irradiated polymer and suppresses the roughening driven by the ion-modified layer.[136] For simultaneous ion/VUV/electron and ion/electron exposures, surface roughness is higher at 65 °C than that at 25 °C, which is consistent with previous studies.[80-82] The elevated substrate temperature increases the mobility and decreases the elastic modulus of the bulk polymer, and thus appears to amplify surface roughening.[139] The observed change of surface roughness and morphology can be qualitatively explained by a bi-layer wrinkling mechanism.

It is worth noting that these experiments were conducted over exposure periods of 1 h. At intermediate (4 mC·cm^{-2}) and high (8 mC·cm^{-2}) electron fluences, 193 nm PR changed from positive-tone to negative-tone polymer during the exposure. The relative transition time during the exposure is expected to be important as well as substrate temperature, since the mobility of polymer fragments is temperature-dependent. For intermediate electron fluence (4 mC·cm^{-2}), the relatively long scission-to-crosslinking transition time and initial low cross-linking density are suspected to induce local non-uniformity in the polymer bulk, and thus increase the surface roughening at an elevated substrate temperature. At 25 °C, with a less mobile polymer matrix, intermediate electron fluence is sufficient to suppress surface roughness (Figure 4.12).

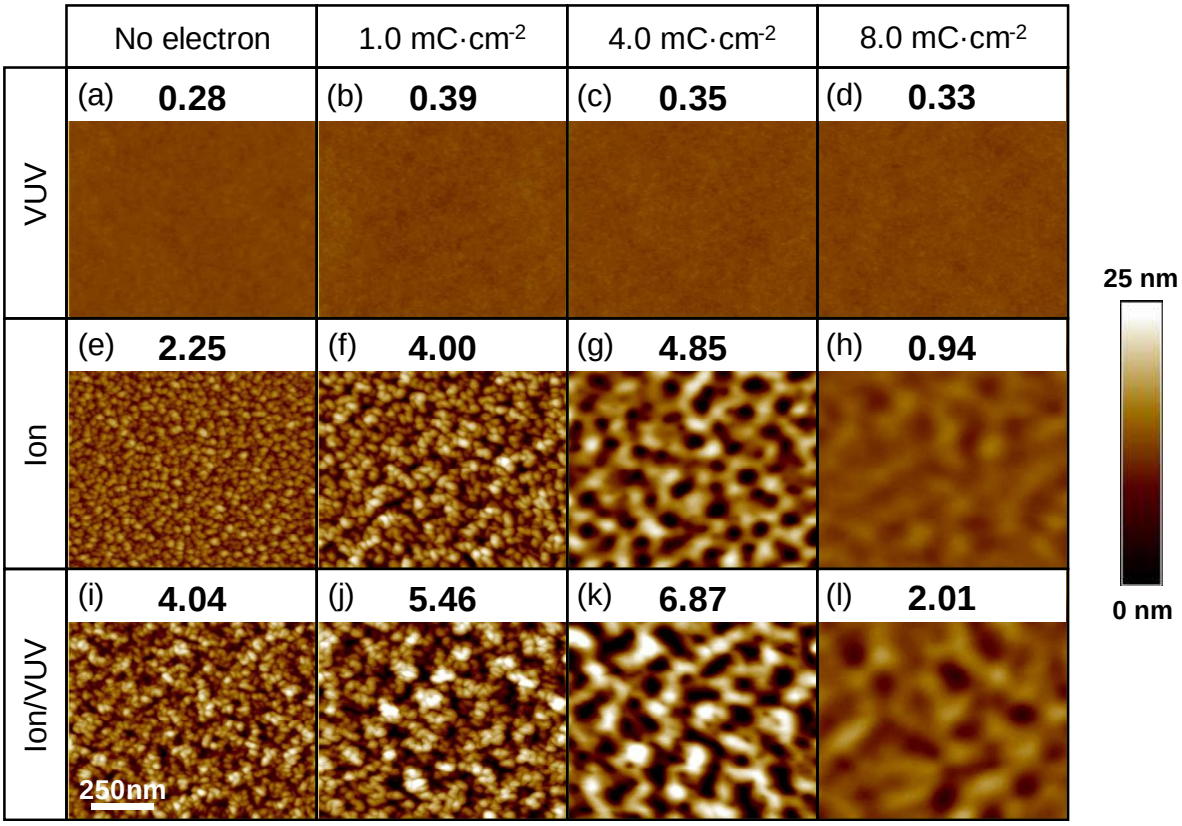

Figure 4.13 1 µm × 1 µm AFM images of 193 nm PR after different exposure protocols at a substrate temperature of 65 °C: simultaneous VUV/electron exposure with different electron fluences (a) no electrons (b) 1 mC·cm^{-2} (c) 4 mC·cm^{-2} (d) 8 mC·cm^{-2}; simultaneous ion/electron exposure with different electron fluences (e) no electrons (f) 1 mC·cm^{-2} (g) 4 mC·cm^{-2} (h) 8 mC·cm^{-2}; simultaneous ion/VUV/electron exposure with different electron fluences (i) no electrons (j) 1 mC·cm^{-2} (k) 4 mC·cm^{-2} (l) 8 mC·cm^{-2}. The 150 eV Ar ion and VUV photon fluence was kept the same: 1×10^{18} ions·cm^{-2}, 4.8×10^{17} photons·cm^{-2}, respectively. The color scale of the images is 25 nm.

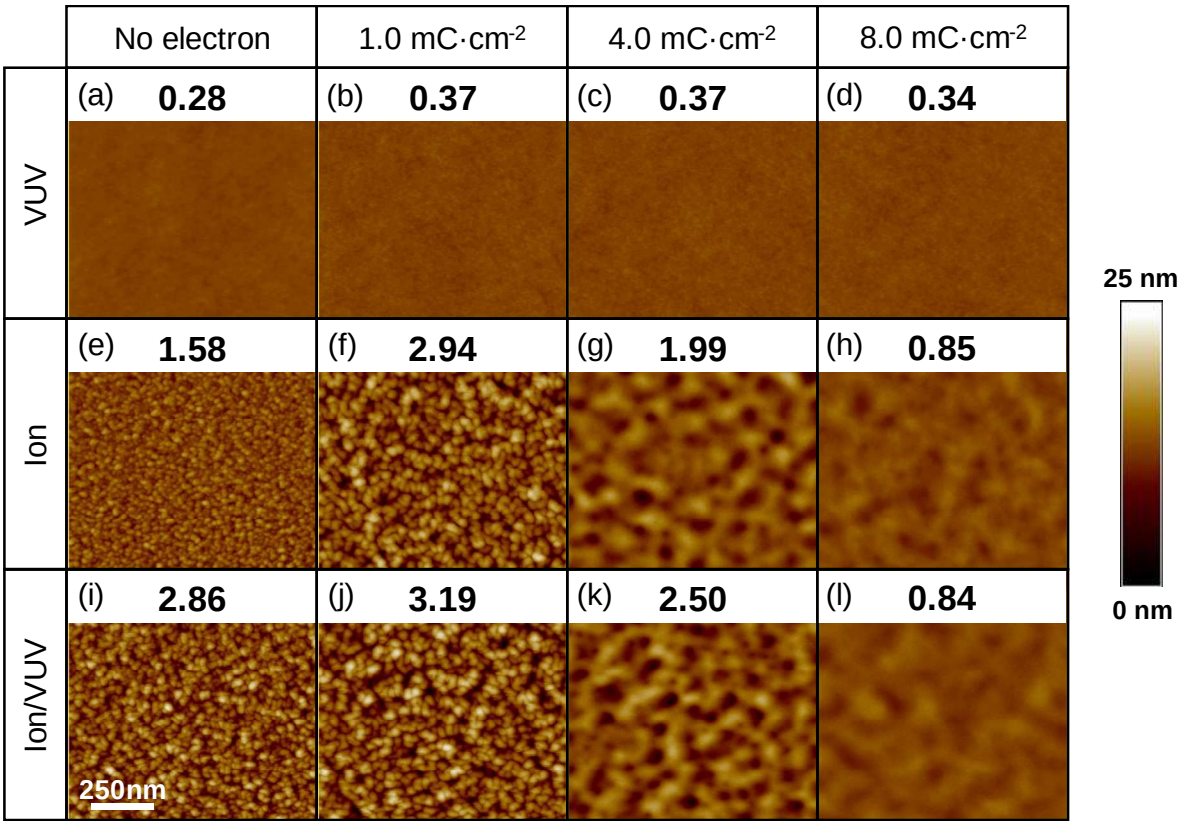

Figure 4.14 1 µm × 1 µm AFM images of 193 nm PR after different exposure protocols at a substrate temperature of 25 °C: simultaneous VUV/electron exposure with different electron fluences (a) no electrons (b) 1 mC·cm^{-2} (c) 4 mC·cm^{-2} (d) 8 mC·cm^{-2}; simultaneous ion/electron exposure with different electron fluences (e) no electrons (f) 1 mC·cm^{-2} (g) 4 mC·cm^{-2} (h) 8 mC·cm^{-2}; simultaneous ion/VUV/electron exposure with different electron fluences (i) no electrons (j) 1 mC·cm^{-2} (k) 4 mC·cm^{-2} (l) 8 mC·cm^{-2}. The 150 eV Ar ion and VUV photon fluence was kept the same: 1×10^{18} ions·cm^{-2}, 4.8×10^{17} photons·cm^{-2}, respectively. The color scale of the images is 25 nm.

4.9 Conclusion

In summary, energetic plasma species modify 193 nm PR into a layered structure. We have observed enhanced surface roughness with simultaneous exposures, providing a combination of a surface carbon-rich layer (~2 nm) from Ar ion bombardment and a bulk-scissioned layer (~100 nm). The scissioning agents can be either VUV photons or low fluence electrons (1 mC·cm^{-2}). Bulk cross-linking induced by high fluence electron exposure (8 mC·cm^{-2}) suppresses surface roughening. It is possible to control the PR surface roughness by manipulating energetic species flux and substrate temperature, while the dynamic nature of surface roughness evolution challenges current understanding and clearly requires further studies.

Chapter 5

Ion and VUV Effects in Surface Roughening of 193 nm Photoresist-associated Homopolymers

5.1 Abstract

While the effects of ions and vacuum ultraviolet (VUV) photons have been identified and a bi-layer wrinkling mechanism has been proposed and described in chapter 4, the role of different pedant groups in 193 nm photoresist (PR) roughening remains poorly understood. This chapter presents the results on roughening of 193 nm PR-associated homopolymers under 150 eV Ar ion bombardment and 147 nm VUV photon irradiation. Poly-(2-methyl-2-adamantyl methacrylate) (p-MAMA) and poly-(R-functionalized adamantyl methacrylate) (p-RAMA) are the chosen materials. P-MAMA is the leaving group and p-RAMA is the polar group in 193 nm PR. Monitored by ex situ transmission FTIR and in situ mass spectrometry, p-MAMA undergoes temperature-dependent bulk degradation during VUV exposure while p-RAMA is relatively insensitive to VUV. We identify the adamantyl leaving group as one of the main photolysis products from p-MAMA. Higher substrate temperatures increase the vapor pressure and facilitate desorption of the detached adamantyl leaving group. The adamantane loss/detachment shows strong correlation to PR surface roughening. A bi-layer wrinkling mechanism is used to qualitatively explain the observed surface roughening. The present results demonstrate that PR leaving group content and structure can couple to plasma etch processes and strongly alter post-etch surface morphology.

5.2 Introduction

The relatively low etch resistance and tendency to roughen observed with methacrylate-based 193 nm photoresist (PR) are generally attributed to its high oxygen content.[19] To achieve both lithography and subsequent plasma etch requirements, 193 nm PR has been formulated with functional groups suitable for 193 nm light exposure.[7] The adamantyl pendant group was added to improve etch resistance.[140] 2-methyl-2-adamantyl methacrylate (MAMA) was then designed to be cleavable by photogenerated acids and has become a commonly used leaving group.[8] Lactone groups are also incorporated to increase the polarity of the polymer and solubility in aqueous alkaline solutions.[141] A R-functionalized adamantyl methacrylate is

the third functional group in 193 nm PR to improve adhesion of the material. These different functional groups could complicate the analysis of roughening mechanisms.

On the other hand, plasma-generated vacuum ultraviolet (VUV) photons have been observed to play a role in both roughening and smoothing of PRs. However, its synergism with other plasma-generated species and the mechanisms associated with the resulting polymer texture are not well understood. Moreover, plasma experiments have shown that poly-(2-methyl-2-adamantyl methacrylate) (p-MAMA), which is the leaving group in 193 nm PR, tends to roughen more compared to 193 nm PRs and associated model copolymers.[14, 89, 142, 143] Surface roughening rate of adamantyl PR was correlated to deposited energy density during plasma processes.[15, 144] However, the interaction between the leaving group and plasma-generated VUV radiation remains unanswered.

In order to clarify the polymer structural dependence in roughening, we further study the effects of ions, VUV photons and substrate heating on 193 nm PR and associated homopolymers. We demonstrate that VUV exposure of PRs cleaves the adamantyl leaving group through in situ mass spectrometry. The adamantane loss/detachment is highly correlated to surface roughening of PRs, but only in the presence of simultaneous ion bombardment. The specific role of ions and VUV photons in material modification will be presented. A bi-layer wrinkling mechanism is proposed to qualitatively explain enhanced roughening observed under simultaneous ion/VUV exposure and moderate substrate heating.

5.3 Experimental Setup

The details of the beam system are described in Chapter 2. The beam sources used in this study were the ion source and the VUV source. The schematic of the system setup is shown in Figure 5.1. The 150 eV Ar ion current at the sample position was measured with Faraday cup 1 (aperture size ~4.55×10^{-4} cm^2). An ion current of 2.8×10^{14} $ions\cdot cm^{-2}\cdot s^{-1}$ (±10%) is used and a 1 h exposure resulted in an ion fluence of 1.0×10^{18} $ions\cdot cm^{-2}$ (±10%). The 147 nm VUV photon flux irradiating on the sample surface was ~1.34×10^{14} $photons\cdot cm^{-2}\cdot s^{-1}$, corrected by an incidence angle of 45° to the surface normal. 1 h VUV irradiation resulted in a photon fluence of 4.8×10^{17} $photons\cdot cm^{-2}$. The bulk chemical modification was characterized with ex situ transmission Fourier transform infrared (FTIR) spectroscopy. The photolysis products were monitored with in situ mass spectrometry. The surface morphology of samples was imaged by atomic force microscopy (AFM) in tapping mode. Root mean square (RMS) surface roughness measurements were performed on multiple AFM scans at different sample positions.

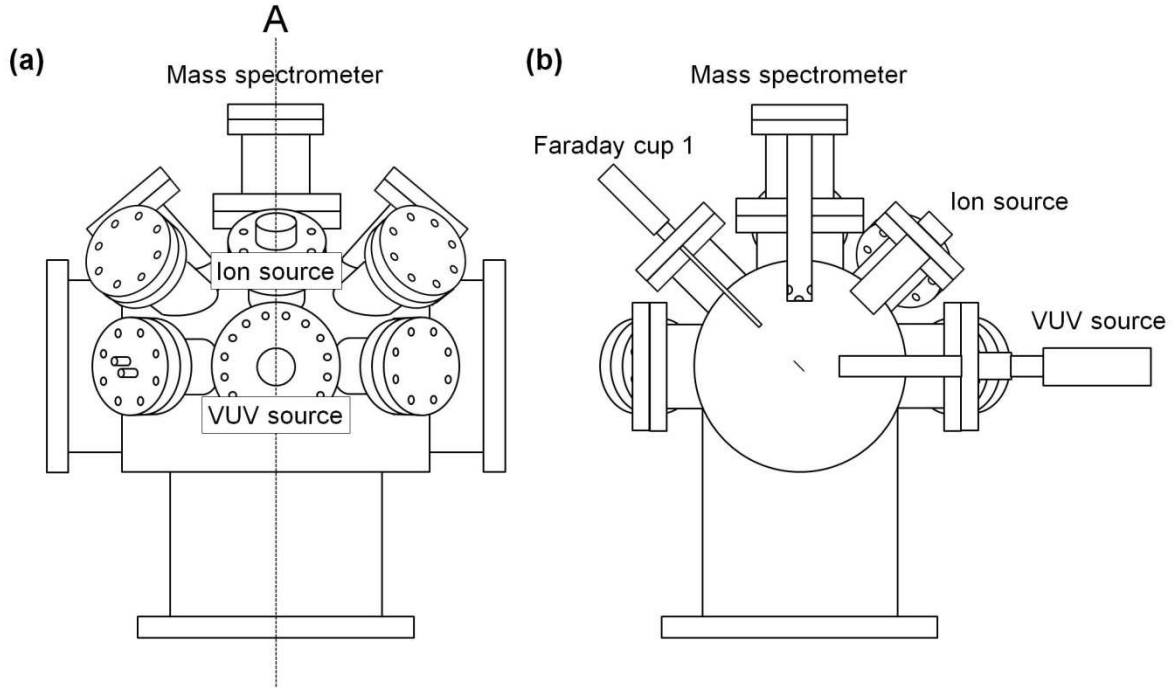

Figure 5.1 (a) Side view of the beam system (b) cross section view of the beam system at plane A labeled in (a).

5.4 Ar Ion Bombardment on p-MAMA and p-RAMA: Physical Sputtering of PR Surface

150 eV Ar ion bombardment on methacrylate-based PRs results in physical sputtering and near-surface region modification. The thickness of the ion-modified layer is about 1.5-2 nm with a density of about 1.8-2.4 $g \cdot cm^{-3}$. It is also expected that this surface layer is under an intrinsic compressive stress, roughly on the order of a few GPa. Detailed discussion can be found in Section 4.4.

To describe the sputtering behavior of organic materials, Ohnishi et al. have proposed a "$N/(N_C-N_O)$" parameter, where N, N_C and N_O are the total number of atoms, the number of carbon atoms and the number of oxygen atoms in a repeating unit, respectively.[19] They showed that the sputtering yield of many polymers under ion bombardment is proportional to this parameter, which is inversely proportional to "effective carbon content" in the polymer. The "Ohnishi parameters" are fairly similar for 193 nm PR (4.07), p-MAMA (3) and p-RAMA (3.36). This implies that ion modification, which is limited to the top 1-2 nm of the polymers, should be similar among the three materials. Finally, the surface roughness of pristine PRs is about 0.3-0.4 nm. The AFM images of p-MAMA, 193 nm PR, and p-RAMA after 150 eV Ar ion bombardment are shown in Figure 5.2. At 65 °C, 1 h of ion bombardment increases surface roughness to ~2.1 nm for p-MAMA, ~2.3 for 193 nm PR and ~1.2 nm for p-RAMA.

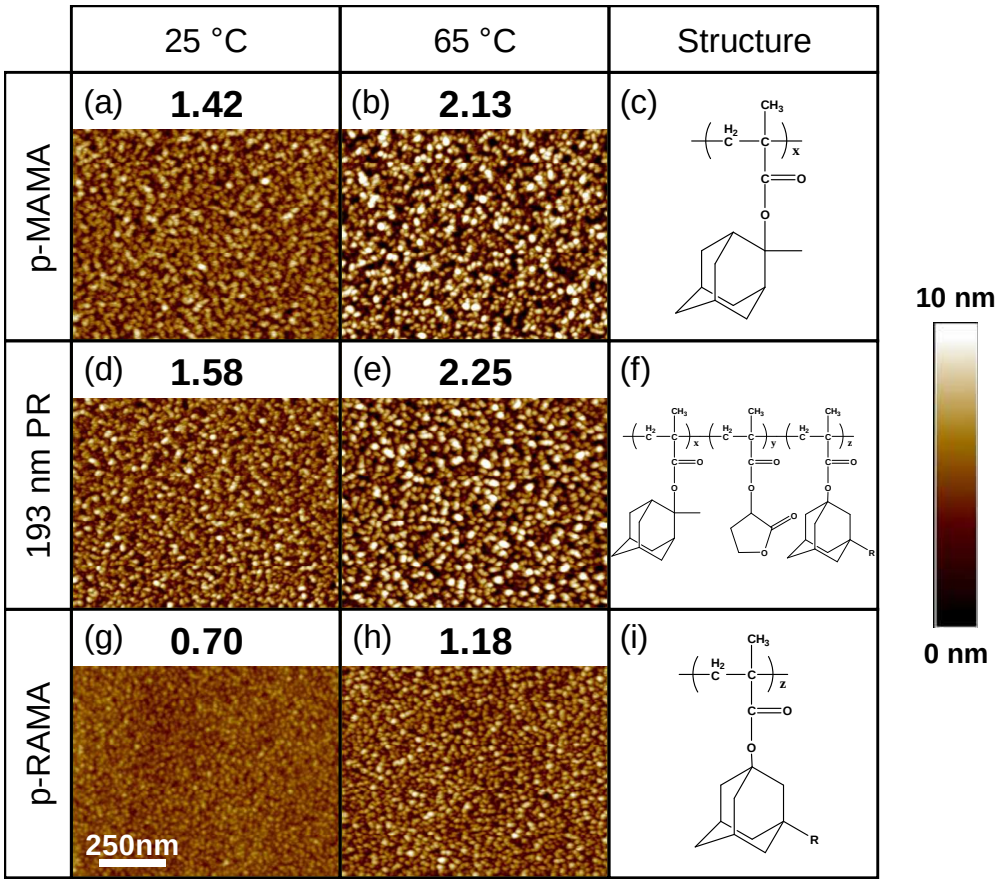

Figure 5.2 1 µm × 1 µm AFM images of p-MAMA (a) 25 °C, (b) 65 °C, 193 nm PR (d) 25 °C, (e) 65 °C, and p-RAMA (g) 25 °C, (h) 65 °C after 150 eV Ar ion bombardment. The chemical structures of polymers are also shown here, (c) p-MAMA, (f) p-193 nm PR, and (i) p-RAMA. The Ar ion fluence was 1×10^{18} ions·cm^{-2}. The color scale of the AFM images is 10 nm.

5.5 VUV Irradiation on p-MAMA and p-RAMA

While ion-induced modification is limited to the near-surface region, transmission FTIR is used to monitor the bulk chemical change caused by VUV irradiation. The transmission FTIR spectra of p-MAMA and p-RAMA after 1 h of VUV irradiation are shown in Figure 5.3 and 5.4, respectively. The substrate was maintained at various temperatures (25-65 °C) during exposure. The results show that p-MAMA is more susceptible to VUV irradiation. The loss of ester linkages (1720 cm^{-1}) (Figure 5.3a), C-O-C bonds (1050-1300 cm^{-1}) (Figure 5.3b), and CH_2/CH_3 moieties (2800-3100 cm^{-1}) (Figure 5.3c) are enhanced by increasing the substrate temperature. On the other hand, p-RAMA is relatively stable under the same fluence of VUV exposure, and the decrease of the FTIR absorption peak is not dependent on the substrate temperature (Figure 5.4). We note that both polymers are thermally stable at these temperatures. The T_g of p-RAMA is ~228 °C, but we were unable to determine the T_g of p-MAMA before decomposition. The decomposition temperature (T_d) of p-MAMA has been reported as 204 °C.[8] Samples processed

with heating only (65 °C) for 1 h were examined with FTIR, and no absorption peak changes were observed.

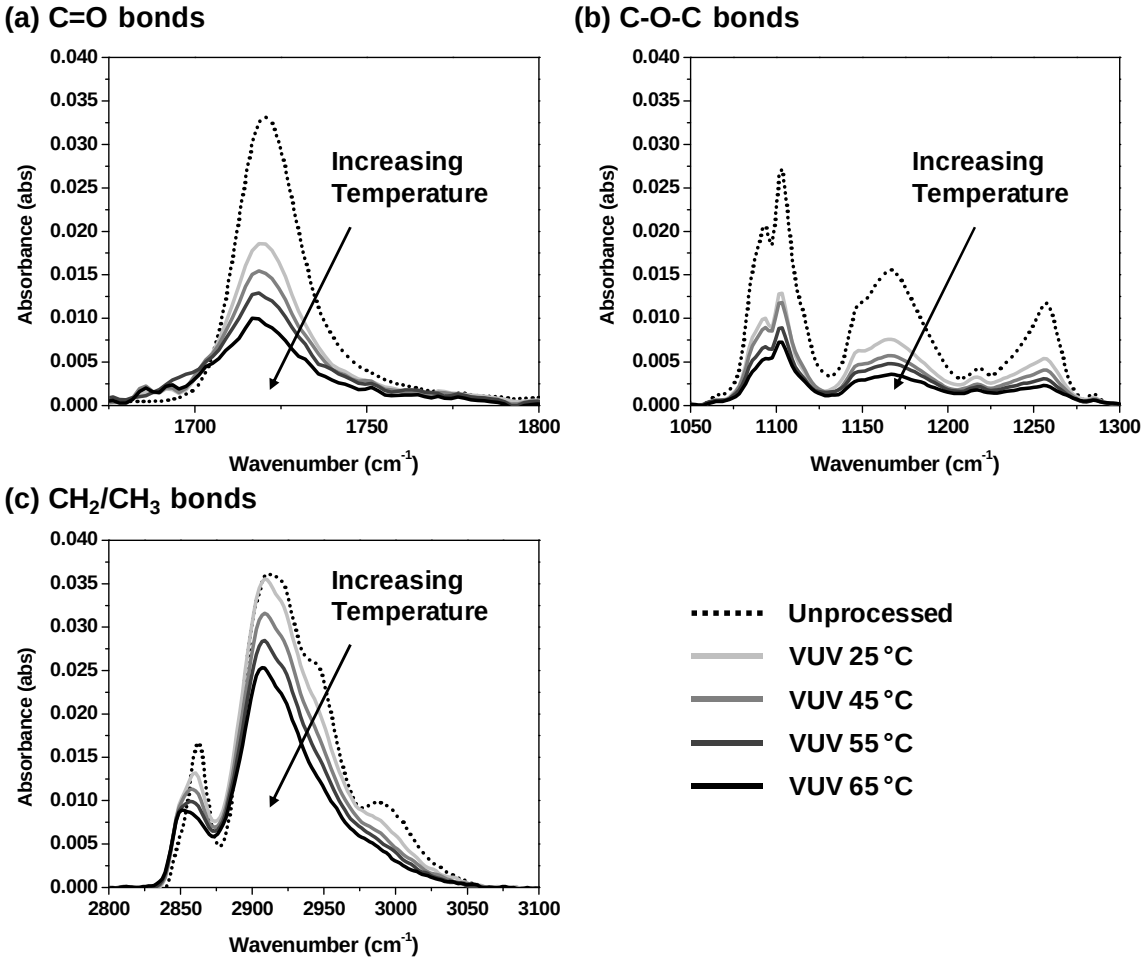

Figure 5.3 Transmission FTIR spectra of p-MAMA after 1 h of 147 nm VUV photon irradiation. (a) C=O bonds (1675-1800 cm^{-1}) (b) C-O-C bonds (1050-1300 cm^{-1}) (c) CH_2/CH_3 bonds (2800-3100 cm^{-1}). The VUV fluence was 4.8×10^{17} photons·cm^{-2}.

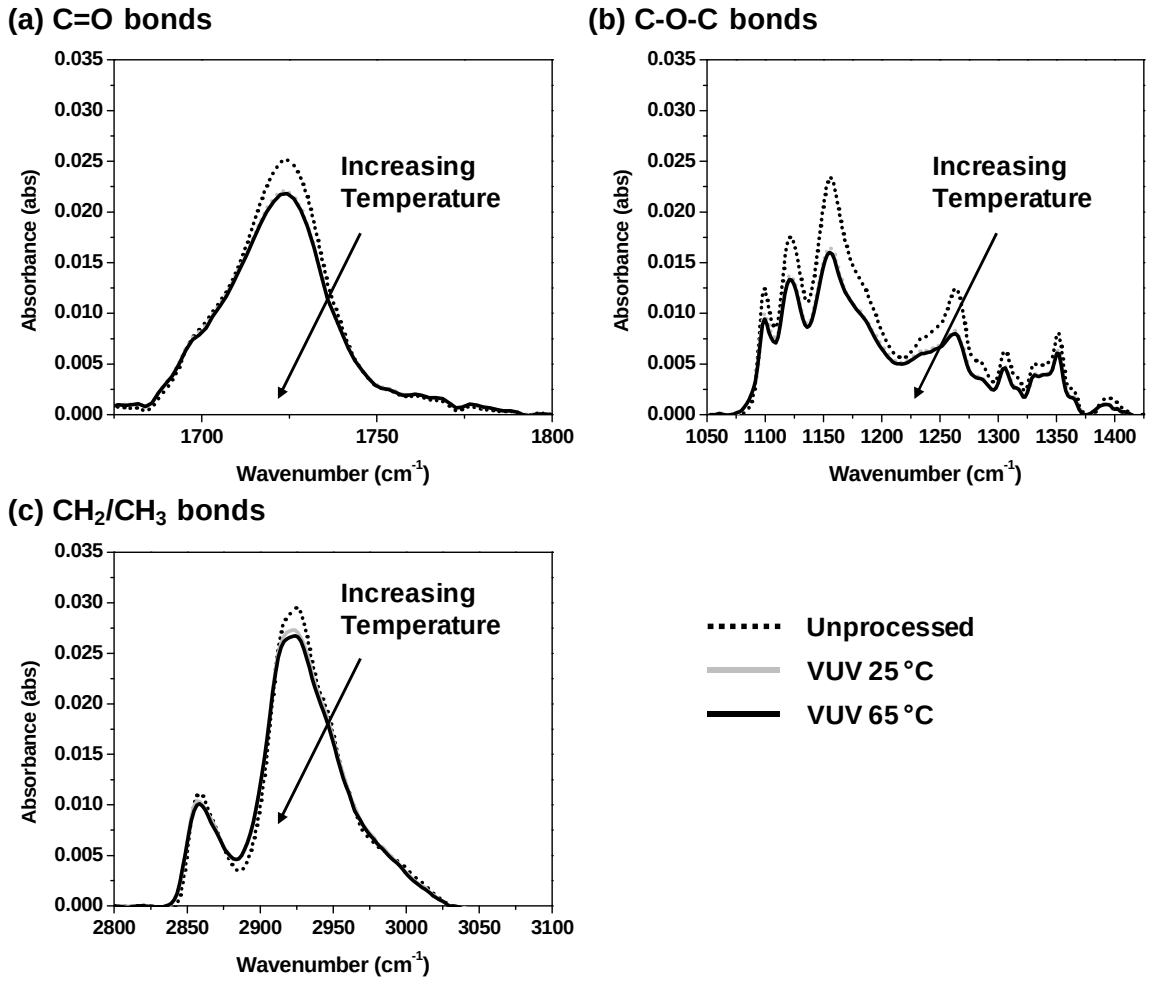

Figure 5.4 Transmission FTIR spectra of p-RAMA after 1 h of 147 nm VUV photon irradiation. (a) C=O bonds (1675-1800 cm^{-1}) (b) C-O-C bonds (1050-1425 cm^{-1}) (c) CH_2/CH_3 bonds (2800-3100 cm^{-1}). The VUV fluence was 4.8×10^{17} photons·cm^{-2}.

After VUV-only irradiation, the surface roughness of all polymers remains similar to that of unprocessed films (~0.3 nm), even at higher substrate temperatures. AFM images of VUV-processed polymers are shown in Figure 5.5. While VUV radiation alone does not roughen the PR at all, FTIR spectra clearly show that VUV-induced damage is highly dependent on the polymer structure.

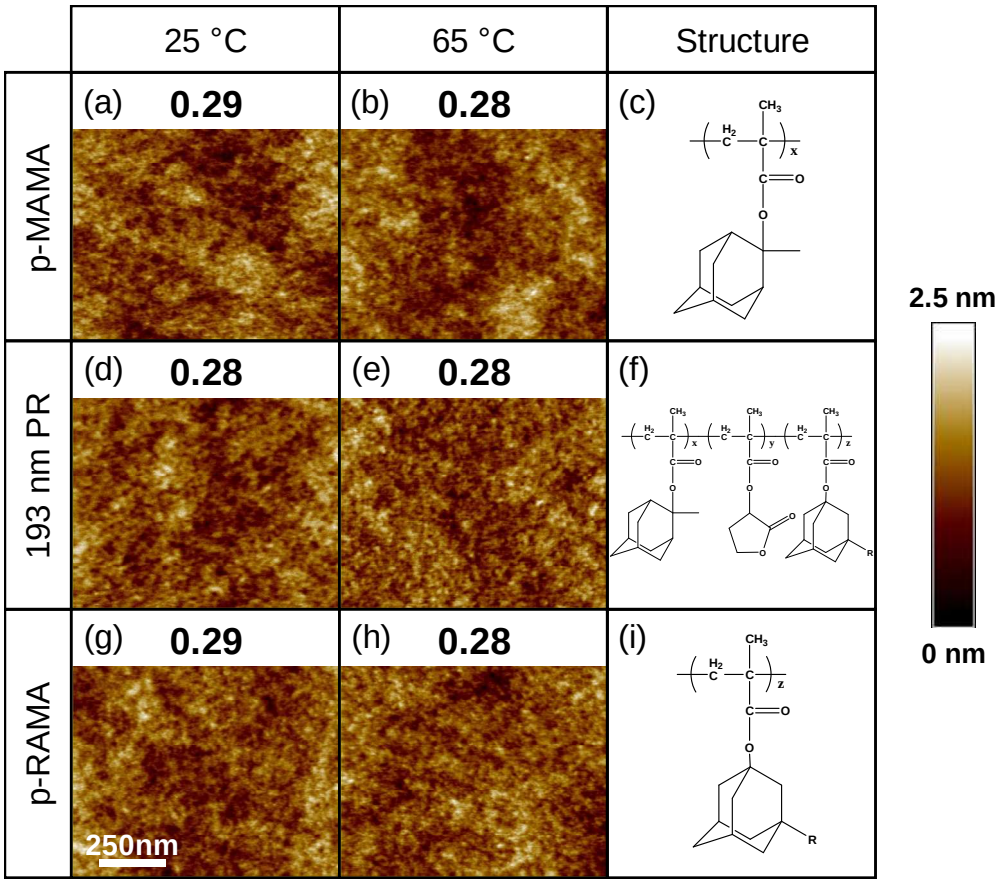

Figure 5.5 1 μm × 1 μm AFM images of p-MAMA (a) 25 °C, (b) 65 °C, 193 nm PR (d) 25 °C, (e) 65 °C, and p-RAMA (g) 25 °C, (h) 65 °C after 147 nm VUV photon irradiation. The chemical structures of polymers are also shown here, (c) p-MAMA, (f) p-193 nm PR, and (i) p-RAMA. The VUV photon fluence was 4.8×10^{17} photons·cm^{-2}. The color scale of AFM images is 2.5 nm.

In situ mass spectrometry was further used to monitor the photolysis products. The residual gas mass spectra of p-MAMA, p-RAMA and 193 nm PR are shown in Figure 5.6. The spectra were taken after 1 min of VUV exposure with a VUV fluence of ~8×10^{15} photons·cm^{-2}. Except for subtraction of the background signal, no further signal processing was performed. The substrate temperature was held at 65 °C. All mass spectra are plotted on the same scale to facilitate direct comparison. For p-MAMA (Figure 5.6a), we observe several main photolysis products, including H_2 (m/z = 2), CO (m/z = 28), CO_2 (m/z = 28, 44) and a peak at m/z = 148 representing the adamantyl leaving group (2-methylideneadamantane, $C_{11}H_{16}$). Peaks from m/z = 60-140 can be attributed to the cracking pattern of the adamantyl leaving group, with the peak clusters separated by about 14 amu intervals.[145] We note that the PR leaving group is designed to be cleavable by photogenerated acids upon 193 nm wavelength exposures. The present result suggests that 147 nm photons can either directly attack the adamantyl-ester linkage or generate protons to cleave the leaving group.

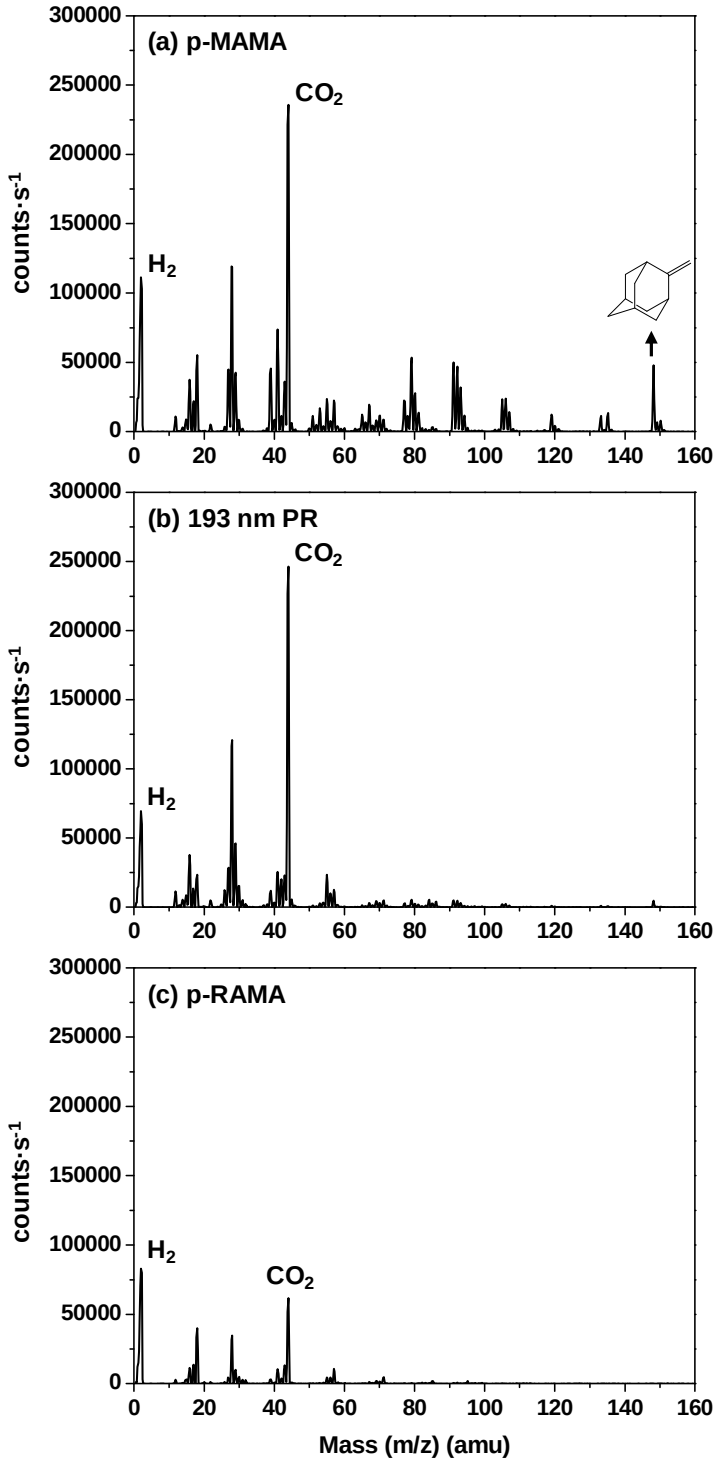

Figure 5.6 Residual gas mass spectra of (a) p-MAMA, (b) 193 nm PR, and (c) p-RAMA after 1 min of VUV exposure. The substrate temperature was maintained at 65 °C.

For 193 nm PR (Figure 5.6b), the main products are H_2, CO, and CO_2. We observe the peak of the adamantyl leaving group and lactone (m/z = 86). However, the adamantane signal is small compared to that from p-MAMA. This result is expected because the total adamantyl leaving group content is less in the 193 nm PR structure.

For p-RAMA, mass spectrometry results are consistent with FTIR, showing that it is relatively insensitive to VUV exposures. The signals of H_2, CO, and CO_2 are smaller compared to p-MAMA and 193 nm PR, and no high mass products can be identified. It shows that the tertiary carbon adamantyl ester of p-RAMA is not easily cleavable by VUV photons (Figure 5.5i), perhaps because of the strain in the adamantane cyclic structure.[8] The formation of a C=C bond requires a sp^2 hybridization which is unlikely to maintain the bond angle in adamantane structure. Whereas in the case of p-MAMA, the methyl group on the C-2 position (Figure 5.5c) is free from ring strain and thus a C=C bond is stable.

To quantitatively compare the results, the raw signal (counts·s^{-1}) from the mass spectrometer must be corrected by the species' electron impact ionization cross section, transmission efficiency and detection coefficient. The signal from detection of neutral species in the mass spectrometer is given by

$$S = \alpha \cdot I_e \cdot \sigma \cdot n_{ionizer} \tag{5.1}$$

S	The measured signal in counts·s^{-1}
I_e	The electron current in the ionizer of the mass spectrometer
σ	The cross section of electron impact ionization
$n_{ionizer}$	The number density of the species in the ionizer

$$\alpha = \beta \cdot t(m/z) \cdot \theta(m/z) \cdot l_{cage} \tag{5.2}$$

β	The extraction efficiency of the ions from the ionizer
$t(m/z)$	The transmission efficiency of the quadrupole mass filter
$\theta(m/z)$	The detection coefficient of the channeltron detector
l_{cage}	The length of the ionizer cage

where transmission efficiency and detection coefficient are both dependent on species mass-to-charge ratio (m/z).

To simplify our analysis, we only compare direct ionization signals from H_2 (m/z = 2), CO_2 (m/z = 44) and the adamantyl leaving group (m/z = 148), whose most intense peak is the parent peak ($A \rightarrow A^+$). The partial ionization cross section at 70 eV electron impact is chosen as: σ_{H_2} = 0.93 $Å^2$, σ_{CO_2} = 2.26 $Å^2$ from literature.[146, 147] The total ionization cross section of adamantyl group is estimated to be 13 $Å^2$.[148] This value is close to that of benzene (C_6H_6), a lower limit for hydrocarbons with similar sum formula or structure.[149, 150] We note that the use of a total ionization cross section will be an upper limit for the partial ionization cross section appropriate for quantitative analysis. Previous results from the same mass spectrometer suggest

$t(m)\theta(m) = m^{-0.81}$, and the extraction efficiency of direct ionization products is independent of mass.[46] The calculated values of H_2 and the adamantyl leaving group are normalized to the CO_2 value from the same polymer, respectively. Results are shown in Table 5.1. For all three materials, CO_2 is the most abundant photolysis product and molecular hydrogen (H_2) is the second most abundant product. The correlation between photolysis products and surface roughness of polymers under simultaneous ion/VUV exposure will be presented and further discussed in following sections.

Table 5.1 Relative photolysis product content of p-MAMA, 193 nm PR and p-RAMA normalized to its CO_2 content. The VUV exposure time was 1 min. The substrate temperature was maintained at 65 °C.

1 min of VUV exposure	Main photolysis products	Relative content versus CO_2
p-MAMA	CO_2	100.0%
	H_2	9.4%
	Adamantyl leaving group	9.4%
193 nm PR	CO_2	100.0%
	H_2	5.6%
	Adamantyl leaving group	0.8%
p-RAMA	CO_2	100.0%
	H_2	26.7%

5.6 Simultaneous Ion and VUV Exposure on p-MAMA and p-RAMA

The AFM images of p-MAMA, p-RAMA and 193 nm PR after simultaneous 150 eV Ar ion and 147 nm VUV exposures are shown in Figure 5.7. The samples were processed with the same ion and VUV fluence (1.0×10^{18} ions·cm^{-2}, 4.8×10^{17} photons·cm^{-2}) over 1 h of exposure. Two sets of substrate temperatures were chosen: 25 °C (Figure 5.7a, d, and g) and 65 °C (Figure 5.7b, e, and h).

We observe that a higher substrate temperature results in a rougher surface for each material. Also, under the same condition, p-MAMA is substantially rougher than 193 nm PR and p-RAMA. P-RAMA is the smoothest of the three materials. It is worth noting that the degree of surface roughening of 193 nm PR processed at 65 °C (Figure 5.7e) is comparable to that after Ar plasma treatment with similar ion and VUV fluence, ~3.5 nm.[82] The severe roughening of p-

MAMA is also consistent with reports from plasma experiments.[14, 89, 142] As presented and discussed in previous sections, VUV-only or ion-only exposures do not give the same degree of surface roughness. Enhanced surface roughness is only observed after simultaneous exposures, when both ion sputtering and VUV-induced photolysis happen at the same time.[80, 81] Because ion bombardment renders similar modification on PR surface, the difference in VUV-induced photolysis could be the key factor in PR surface roughening upon simultaneous ion/VUV exposure.

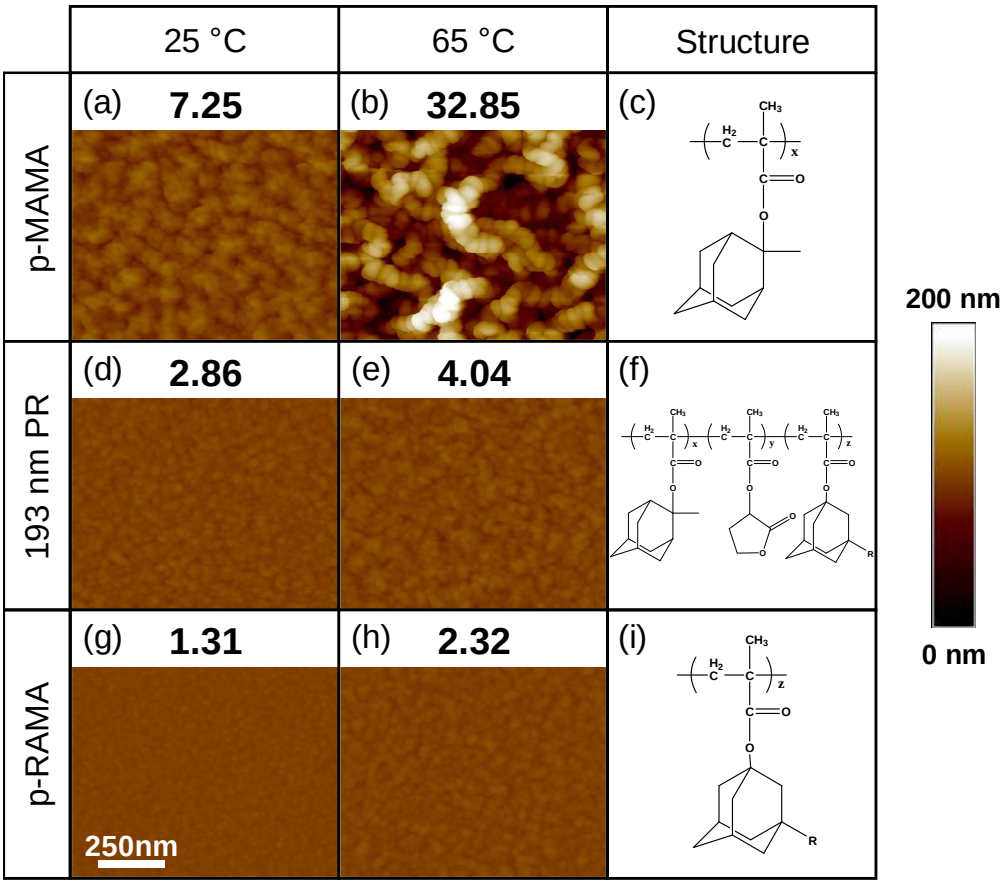

Figure 5.7 1 µm × 1 µm AFM images of p-MAMA (a) 25 °C, (b) 65 °C, 193 nm PR (d) 25 °C, (e) 65 °C, and p-RAMA (g) 25 °C, (h) 65 °C after simultaneous 150 eV Ar ion and 147 nm VUV photon exposure. The chemical structures of polymers are also shown here, (c) p-MAMA, (f) 193 nm PR, and (i) p-RAMA. The Ar ion fluence was 1×10^{18} ions·cm^{-2} and the VUV photon fluence was 4.8×10^{17} photons·cm^{-2}. The color scale of the AFM images is 200 nm.

Figure 5.8 shows the temporal evolution of H_2 (Figure 5.8a), CO_2 (Figure 5.8b), and adamantyl leaving group (Figure 5.8c) under VUV exposures at 25 and 65 °C. The exposure time was 1 h; VUV was turned on at 0 min and off at 60 min.

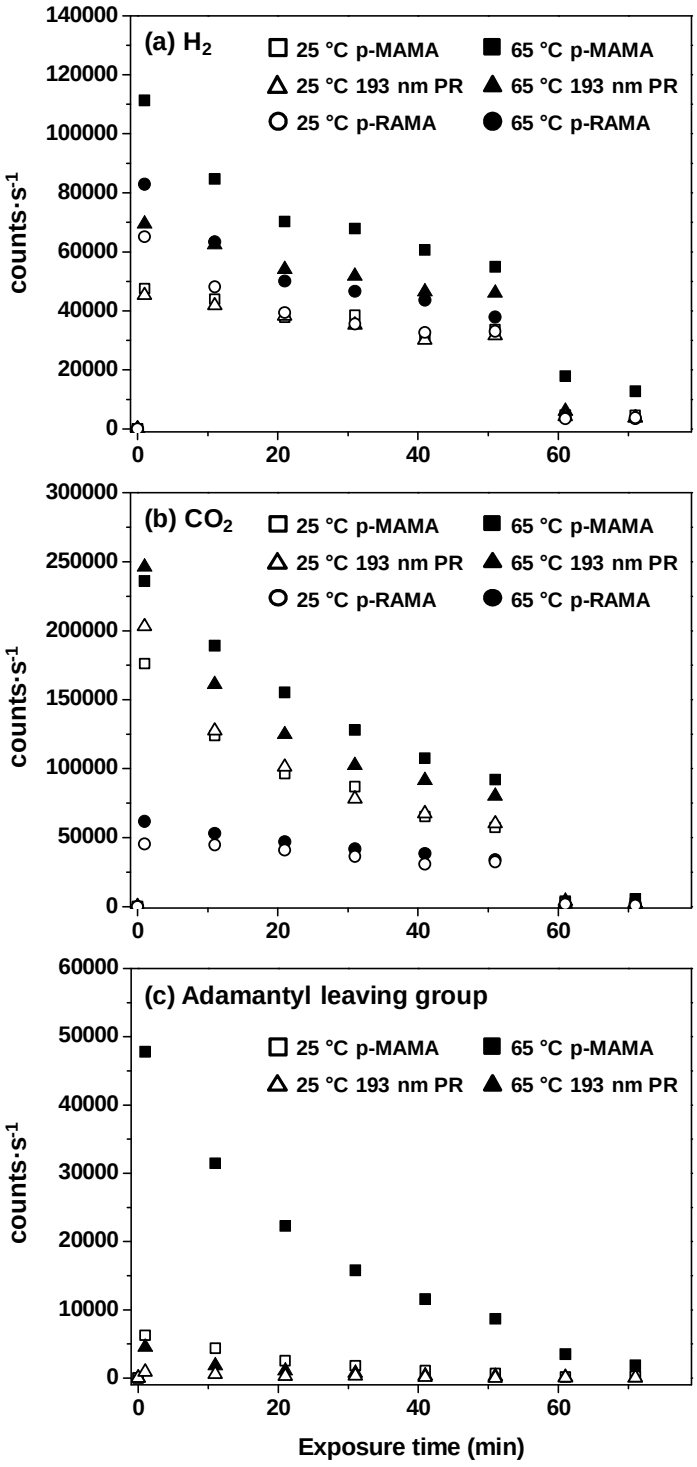

Figure 5.8 Temporal evolution of photolysis products under VUV exposure (a) H_2, (b) CO_2, and (c) adamantyl leaving group.

Two phenomena are observed. First, the photolysis product signal peaks at the first minute of exposure and then gradually decreases for all three polymers at both processing temperatures. This suggests the saturation of the penetration depth of photons in PRs. The saturation of VUV penetration in methacrylate-based PR has been simulated and verified by experiments.[119] At first, photons rapidly cleave the oxygen-containing linkages in the near-surface region of polymers. Desorption of photolysis products allow photons to further penetrate and release materials in the bulk film since the remaining C-C and C-H bonds have a lower absorption cross section in the VUV region of interest here. However, the photons are ultimately absorbed by these remaining carbon-carbon and carbon-hydrogen bonds (albeit requiring deeper penetration) and thus the penetration depth saturates. Second, higher substrate temperatures result in higher material loss.

Nelea et al. have reported mass spectrometry results of 121.6 nm VUV exposure on polyethylene (PE), polypropylene (PP), polystyrene (PS), poly (ethylene terephthalate) (PET), and polyamide-6 (PA).[151] For all five polymers investigated, the primary product was molecular hydrogen. In our studies, CO_2 is the most abundant photolysis product and molecular hydrogen (H_2) is the second most abundant product for all three materials (Table 5.1 and Figure 5.8). The difference might be attributed to higher concentration of oxygen-containing moieties in PRs. In general, the ester and lactone species have higher photon absorption cross sections than alkane and alkene in the VUV region of interest here.[152-155] Our result from mass spectrometry is also consistent with the higher fractional loss of oxygen-containing absorption peak obtained from transmission FTIR.

As mentioned earlier, higher oxygen-content generally results in lower etch resistance for 193 nm PRs as compared to other PRs. However, oxygen content itself cannot explain the enhanced surface roughening under simultaneous ion/VUV exposure and moderate substrate heating. First, p-MAMA and p-RAMA have similar densities of ester linkage, but p-MAMA is severely roughened compared to p-RAMA under the same processing condition (Figure 5.7). Moreover, from our mass spectrometric study, the generation of CO_2 upon VUV exposure is not correlated to the surface roughness. While 193 nm PR and p-MAMA generate comparable amount of CO_2 upon VUV irradiation, the surface roughening of 193 nm PR is considerably less than that of p-MAMA (Figure 5.7). Lastly, the generation of H_2 does not appear to correspond to PR surface roughening, either.

The only distinctive factor is the cleavage and desorption of the adamantyl leaving group upon VUV exposure (Figure 5.6 and 5.8). The higher the adamantyl leaving group loss, the higher the surface roughness of processed polymer (Figure 5.7). Figure 5.9a shows the temporal evolution of the adamantyl leaving group for p-MAMA under VUV exposures at various substrate temperatures. It clearly demonstrates that higher substrate temperatures result in higher adamantyl leaving group loss.

Figure 5.9b shows the relationship between relative adamantyl leaving group loss and adamantane vapor pressure. The relative loss is calculated by normalizing the area integral of the mass spectra raw data (Figure 5.9a) to that at 65 °C. The adamantane vapor pressure data is taken by interpolation from the literature values.[156] It shows a fairly good linear relationship, suggesting the increased loss of the adamantyl leaving group is controlled by its vapor pressure. It also suggests that at a higher substrate temperature, VUV photons can penetrate deeper into p-

MAMA film because the cleaved adamantyl leaving groups are ready to leave without absorbing excess incoming photons. It is worth noting that the structure of the adamantyl leaving group is slightly different from adamantane, with an additional C=C double bond at the C-2 position (Figure 5.9b). However, it is likely that the thermodynamic properties of these two compounds are similar, and the increased loss of materials can be explained by the change of vapor pressure.

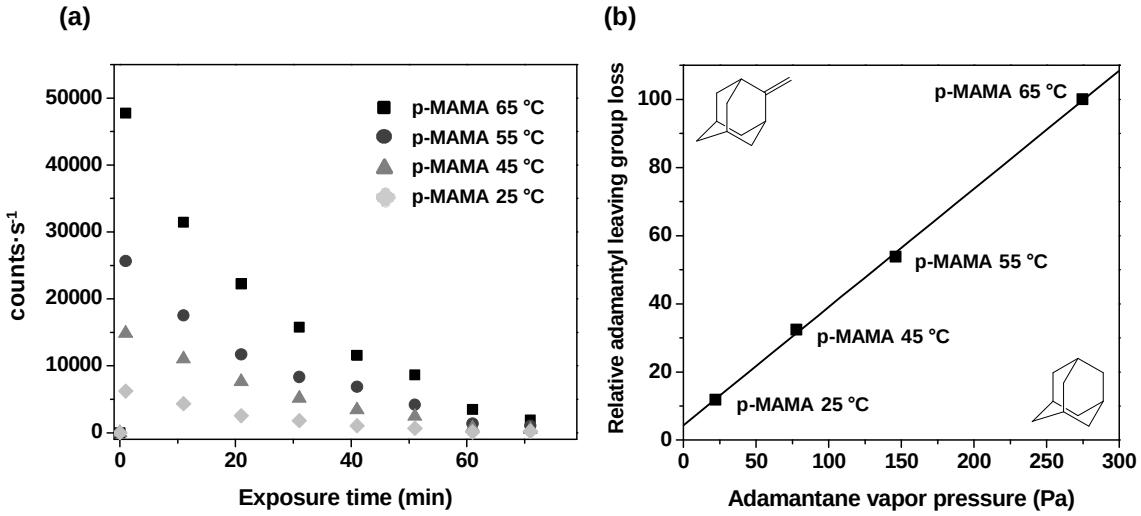

Figure 5.9 (a) Temporal evolution of the adamantyl leaving group of p-MAMA under VUV exposure at various substrate temperatures. (b) Relative adamantyl leaving group loss versus adamantane vapor pressure.

Lastly, simultaneous ion/VUV exposures were done on p-MAMA at various substrate temperatures, and the AFM images are shown in Figure 5.10. A higher substrate temperature results in higher surface roughness.

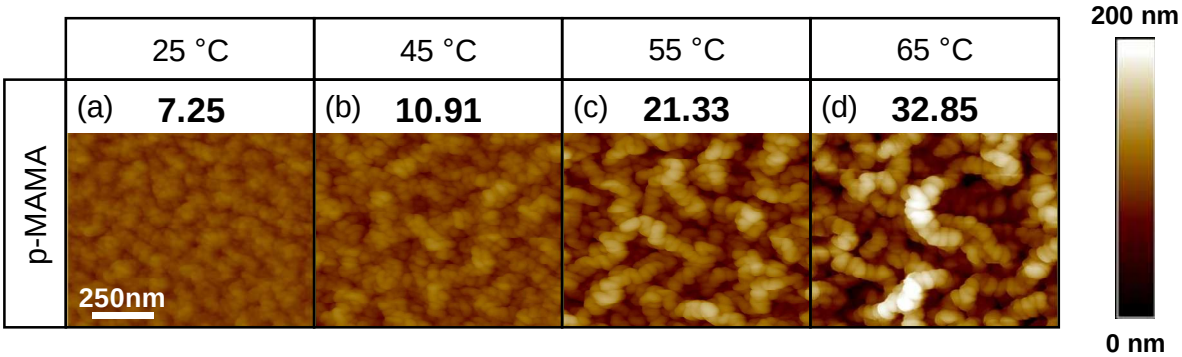

Figure 5.10 1 µm × 1 µm AFM images of p-MAMA after simultaneous ion/VUV exposure at various substrate temperatures (a) 25 °C, (b) 45 °C, (c) 55 °C, and (d) 65 °C. The Ar ion fluence was 1×10^{18} ions·cm^{-2} and the VUV photon fluence was 4.8×10^{17} photons·cm^{-2}. The color scale of the images is 200 nm.

From FTIR spectra, the loss of the CH_2/CH_3 absorption peak for simultaneous ion/VUV exposure is less than that for VUV-only exposure, as shown in Figure 5.11. It suggests that the highly carbon-rich surface layer caused by ion bombardment hinders the desorption of detached adamantyl leaving groups. However, as mentioned earlier, the formation of an ion-modified layer requires a period of 0.5-1 min under our experimental condition. Significant amount of adamantyl leaving groups would have been desorbed before the complete formation of this surface layer. Moreover, since this layer will give restriction to all the ion-bombarded conditions, a comparison by the mean of "relative loss of adamantyl leaving group" is legitimate. It is noted that "relative loss of adamantyl leaving group" is directly measured and calculated from mass spectrometry measurements. It is also an index of VUV penetration and adamantyl group detachment. A higher degree of adamantane loss also refers to deeper modification and a greater extent of detachment.

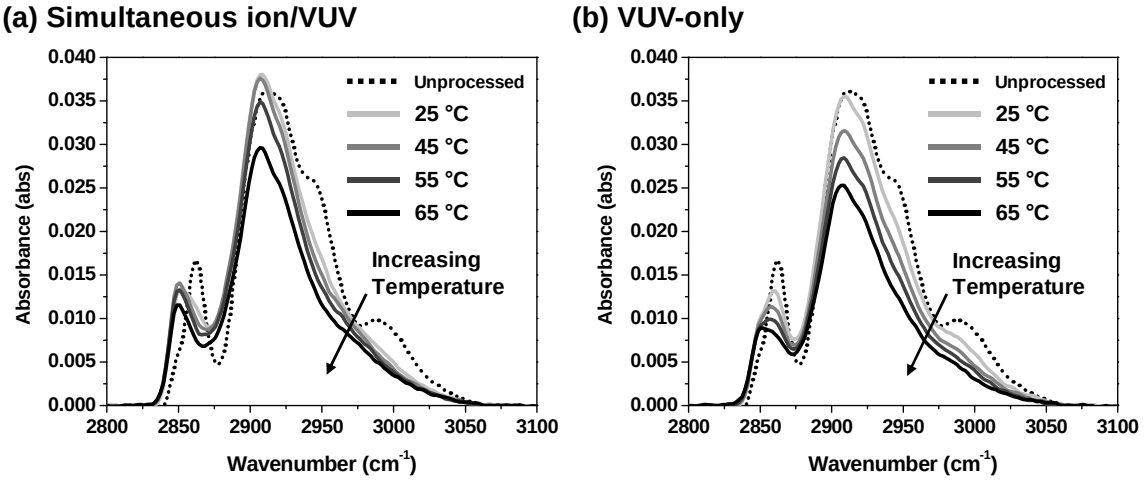

Figure 5.11 Transmission FTIR spectra of p-MAMA in the region of CH_2/CH_3 bonds (2800-3100 cm^{-1}) after (a) simultaneous ion/VUV exposure, (b) VUV-only irradiation at various substrate temperatures. The Ar ion fluence was 1×10^{18} ions·cm^{-2} and the VUV photon fluence was 4.8×10^{17} photons·cm^{-2}.

In Figure 5.12a, we plot the surface roughness of p-MAMA and 193 nm PR caused by simultaneous ion/VUV exposure versus the relative loss of adamantyl leaving group by VUV-only exposure. A good correlation observed here suggests that higher adamantyl leaving group loss/detachment is associated with higher surface roughness. In Figure 5.12b, the dominant lateral characteristic wavelengths, i.e. roughness feature width, caused by simultaneous ion/VUV exposure are plotted against relative adamantyl leaving group loss by VUV-only exposure. It also shows a good correlation; higher adamantyl leaving group loss/detachment results in longer lateral wavelength. It clearly suggests that the loss and detachment of adamantane plays a key role in PR surface roughening. We will discuss the possible mechanism in the following section.

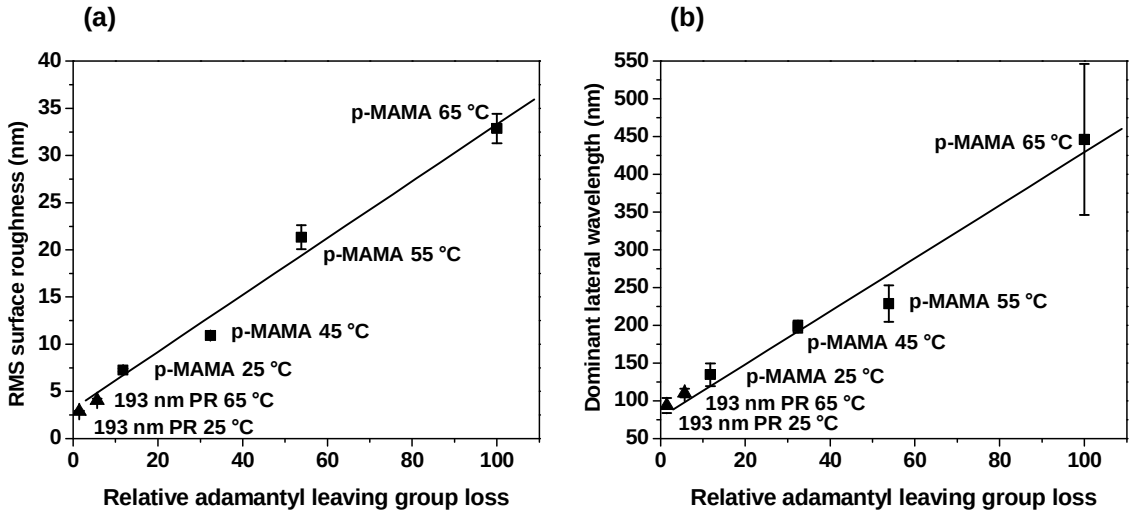

Figure 5.12 (a) Surface roughness resulting from simultaneous ion/VUV exposure versus relative adamantyl leaving group loss caused by VUV-only exposure. (b) Dominant lateral wavelength resulting from simultaneous ion/VUV exposure versus relative adamantyl leaving group loss caused by VUV-only exposure.

5.7 Discussion

We have shown a strong correlation between the loss/detachment of adamantyl leaving group and surface roughening of PRs with simultaneous ion/VUV exposure. VUV irradiation causes a modified bulk region as observed from transmission FTIR and mass spectrometry. As reported in previous studies and discussed in the earlier sections, ion exposure of PR materials results in a near-surface layer with a probable compressive stress of about a few GPa. Simultaneously exposing PR to ions and VUV photons therefore confers a bi-layer character to the PR.

As summarized in Section 4.6, Bruce et al. have suggested a bi-layer wrinkling mechanism to explain nanoscale surface roughening of polymers under plasma etch conditions.[131] In short, to initiate the wrinkling phenomenon on a bi-layer system, the overlayer has to be under a compressive stress, σ, which is above the value of critical stress, σ_c. If both layers are assumed to be elastic, σ_c is

$$\sigma_c = -\frac{E_f}{4\left(1-\nu_f^2\right)}\left[\frac{3E_s\left(1-\nu_f^2\right)}{E_f\left(1-\nu_s^2\right)}\right]^{2/3} \tag{5.3}$$

where E is the elastic modulus, ν is the Poisson's ratio, and subscripts f and s denote the stiff overlayer and compliant underlayer, respectively.

In the small deformation limit, the equilibrium amplitude, A, and wavelength, λ, can be readily derived as shown here:

$$A = h\left(\frac{\sigma}{\sigma_c} - 1\right)^{1/2} \tag{5.4}$$

$$\lambda = 2\pi h\left[\frac{E_f\left(1-\nu_s^2\right)}{3E_s\left(1-\nu_f^2\right)}\right]^{1/3} \tag{5.5}$$

where h is the thickness of the top layer.

We note that both amplitude and wavelength are proportional to $E_s^{-1/3}$, where E_s is the elastic modulus of the compliant underlayer. A decreased underlayer modulus will increase both the equilibrium amplitude and wavelength of the wrinkle. In other words, if an agent could reduce the modulus of the underlayer, it would then magnify the wrinkle formation according to this theory.

Bruce et al. showed that a 150 eV Ar ion modified surface layer with an intrinsic stress of ~-17.3 GPa was sufficient to induce a few nanometers of surface roughness with a dominant wavelength of tens of nanometers on Ar plasma-processed PS.[131] In the present case, we assume the properties of the ion-modified layer are unchanged at different temperatures, and the only variable that can change is elastic modulus, E_s, of the underlayer. With these assumptions, the model stipulates that for p-MAMA, a decrease of elastic modulus of roughly 2 orders of magnitude is needed to obtain a ~4.5 times increase of RMS surface roughness and a ~3.3 times increase of the dominant wavelength from 25 to 65 °C. A decrease of polymer elastic modulus by 2 orders of magnitude is in fact usually observed when the temperature is close to its glass transition temperature (T_g). If the T_g of the VUV-modified underlayer can be shown to decrease when the temperature approaches 65 °C, then the observed PR texturing could be qualitatively explained by the proposed wrinkling mechanism.

As mentioned in Section 4.5, Pargon et al. provided experimental evidence that after plasma VUV exposure, the bulk T_g of 193 nm PR decreased to ~110 °C.[93] It is suspected that detached free lactone and adamantyl group may stay in the film and act as plasticizers to soften the film.[90, 93] Also, main chain scissioning could take place and thus decrease the T_g of the polymer matrix.[115] The role of adamantyl groups in 193 nm PR appears to be crucial. The adamantane moiety was first added to methacrylate-based polymers to increase etch resistance. Besides improving the etch resistance of PR, rigid adamantyl pendant groups also increase polymer T_g.[157] In the early 1990s, Matsumoto et al. showed that for 1-adamantyl methacrylate copolymerized with methyl methacrylate, the increase of adamantane content increased the T_g of polymers from ~120 °C to above 200 °C.[158]

We have shown that VUV exposure leads to cleavage and desorption of the adamantyl leaving group. Moderate substrate heating elevates adamantyl vapor pressure, resulting in enhanced adamantyl desorption. This resulting decrease in adamantane content should greatly

decrease T_g. Without the RAMA component, the T_g of VUV-exposed p-MAMA is expected to be even lower than that of VUV-exposed 193 nm PR (~110 °C, as measured by Pargon et al.). We cannot directly measure the amount of adamantyl leaving groups whose desorption is hindered by the ion-modified layer. However, they can act as plasticizers to also decrease T_g and E_s of the VUV-modified underlayer.[90, 93] Scott et al. reported that addition of plasticizers into PMMA greatly reduced the T_g of PMMA from 120 °C to below room temperature, depending on the type and volume fraction of plasticizer used.[159] With a 30 vol% of plasticizers in PMMA, roughly 2 orders of magnitude decrease of elastic modulus was reported at 80 °C, close to the temperature in this study. We propose that the combined effect, namely desorption of adamantyl groups and detached adamantane acting as plasticizers, will reduce the T_g of the underlying film sufficiently to account for the reported polymer surface texturing in the context of wrinkling theory. While we cannot rule out the mechanism of detached lactone groups acting as plasticizers in the polymer film, the fact that p-MAMA is significantly rougher than 193 nm PR suggests that loss/detachment of the adamantyl group by VUV is the dominant factor. This effect is clearly shown in Figure 5.12.

However, it is important to keep in mind that during actual plasma etch or simultaneous ion/VUV exposure, the film properties are varying in both depth and time. The photolysis products trapped by the ion-modified layer also possibly build up out-of-plane stress to this layer, especially under moderate substrate heating. The wrinkling theory described above refers to a system which does not account for the dynamic change. It seems clear that a more sophisticated analysis of the film mechanical behavior is required to further describe PR surface roughening in detail. Also, further studies have to be carried out in order to directly compare surface roughness of blanket film with roughness developed on patterned samples, which bear different boundary conditions.

Although we chose to employ a simple plasma chemistry, namely Ar, we recognize that more complex plasma chemistries may well involve additional roughening mechanisms. For instance, VUV flux and wavelength are different in other inert gas plasmas.[84] Fluorocarbon-containing plasmas lead to a competition between etching and fluorocarbon polymer deposition. Moreover, C and CF-related VUV emission in the 150-210 nm wavelength range strongly modifies 193 nm PR.[50] Thermal stress-induced instability and micromasking have also been proposed to explain the roughening of 193 nm PR under fluorocarbon-containing plasma etch.[13] It is clear that further studies of plasma chemistry and its effects on mechanical properties of treated materials are crucial to establish a better understanding of PR roughening mechanism.

5.8 Conclusion

Results from vacuum beam experiments on commercial methacrylate-based 193 nm PR and its homopolymer constituents show that p-MAMA has higher VUV sensitivity compared to 193 nm PR and p-RAMA. Besides H_2, CO, and CO_2, the adamantyl leaving group is one of the main photolysis products. Observed loss of adamantyl leaving group is highly correlated with its change in vapor pressure as the film temperature increases. Also, adamantane loss/detachment is suggested to lower the T_g of the polymer and thereby decrease its elastic modulus. We have observed enhanced surface roughening with simultaneous ion/VUV exposures, providing a

combination of a surface carbon-rich layer (~2 nm) from Ar ion bombardment and a more compliant underlayer as induced by photolysis from VUV irradiation. Under the same conditions, the surface roughness of p-MAMA is much higher than that of 193 nm PR and p-RAMA. It can be qualitatively explained by a stress-induced wrinkling mechanism: loss/detachment of the adamantyl leaving group lowers the T_g and elastic modulus of the polymer film and thus increases both equilibrium amplitude and wavelength. We conclude that the behavior of the PR leaving group during plasma exposures is a key factor for future design of PR materials and plasma etch processes.

Chapter 6

Plasma Deactivation of Endotoxic Biomolecules: Vacuum Ultraviolet Photon and Radical Beam Effects on Lipid A

6.1 Abstract

Low-pressure plasmas are promising techniques for surface sterilization of bacteria and deactivation of harmful biomolecules. It is widely accepted that plasma-generated energetic and reactive species are responsible for plasma-induced sterilization; however, how these species act alone or synergistically to deactivate endotoxic biomolecules is not completely understood. Using a vacuum beam system, we study the effects of vacuum ultraviolet (VUV) radiation, oxygen and deuterium radicals on lipid A, the immune-stimulating region of lipopolysaccharide (LPS). VUV-induced photolysis causes bulk modification of exposed lipid A film up to the penetration depth of VUV photons, ~200 nm. On the other hand, radicals mainly cause chemical etching and modification near the surface of lipid A films. The fatty acid chains and the phosphate groups, key structures governing the endotoxic activity of lipid A, are greatly reduced after beam exposures. Although radical-induced etch yield of lipid A is lower than VUV-induced photolysis, secondary ion mass spectrometry (SIMS) and human whole blood-based assay suggest radicals render a higher degree of modification at the film surface. This study contributes to the fundamental understanding of plasma effects on biomolecules for better sterilization/deactivation schemes and applications.

6.2 Introduction

Studies have found protein and endotoxin contamination on ready-for-use instruments in healthcare facilities.[30-33] This has raised concerns of transmission of Creutzfeldt-Jacob diseases (CJD) and the sepsis syndrome caused by bacterial pyrogens, such as lipopolysaccharide (LPS), the major component of the outer-membrane of Gram-negative bacteria.[34] Low temperature plasma-based technologies are promising alternatives to sterilize bacteria and deactivate virulent biomolecules from the surface of heat-sensitive medical instruments.[37-39] The effects of plasmas on a biological target are typically attributed to plasma-generated energetic and reactive species; however, how these species act alone or

synergistically on biomolecules is not completely understood. To investigate the mechanisms of biomolecule deactivation, we chose lipid A (*Salmonella minnesota* Re 595 mutant), the primary immune-stimulating region of LPS, as our model biomolecule. As shown in Figure 6.1a, lipid A typically consists of a β(1-6)-linked D-glucosamine disaccharide carrying two phosphoryl groups at positions 1 and 4'. This hydrophilic backbone is attached to four acyl chains by ester (positions 3 and 3') and amide linkages (positions 2 and 2'). These chains can be further substituted to provide lipid A molecules with up to seven acyl substituents.[67] For *Salmonella minnesota* Re 595 mutant, non-stoichiometric substitutions are shown with dashed bonds.

As mentioned earlier, LPS (mainly via its lipid A component) is capable of inducing the sepsis syndrome. LPS-induced sepsis is the consequence of dysregulation of an initial, appropriate host immune response. Cells of the innate immune system, such as monocytes and macrophages, can recognize LPS through Toll-like receptor 4 (TLR-4) and protein complexes to initiate the secretion of a range of pro-inflammatory proteins, including interleukin-1β (IL-1β), IL-6, and tumor necrosis factor-α (TNF-α). Local inflammation of an infected tissue is of course necessary in combating infection; however, the systemic inflammatory reaction can become dysregulated and lead to sepsis.[34, 77]

It is known that endotoxic activity of lipid A is highly correlated to its molecular structure in order to be recognized by cell receptors. Diphosphorylated β(1-6)-linked D-glucosamine disaccharide backbone carrying six acyl chains, such as *E. coli*. lipid A, expresses the highest endotoxic activity. Any deviation from this structure reduces its activity, e.g. the number and length of acyl chains, the phosphorylation state, and the disaccharide residue. For example, monophosphoryl lipid A is about a 1000-fold less active than *E. coli*. lipid A. Synthetic tetra-acyl lipid A (compound 406) not only lacks endotoxic activity, but also inhibits normal lipid A signaling.[67]

Using a high vacuum beam system, we herein report the effects of VUV photons, oxygen and deuterium radicals on lipid A deactivation. Oxygen and hydrogen plasmas have been the choice of many plasma-sterilization studies because of their oxidative nature and high UV/VUV photon flux, respectively. We demonstrate that VUV-induced photolysis and radical-induced chemical etching are able to damage lipid A's molecular structure and reduce its endotoxic activity. These results contribute to the fundamental understanding of plasma-generated species interaction with biomolecules.

6.3 Materials, Experimental Setup, and Sample Characterization

The chemical structure of lipid A molecules used in this study is shown in Figure 6.1. Sample preparation procedures are described in detail in Chapter 3. The diphosphoryl lipid A, obtained by hydrolysis of *Salmonella minnesota* Re 595 mutant LPS, was observed as a mixture with various non-stoichiometric substitutions and molecular masses by a quadrupole time-of-flight (Q-ToF) mass spectrometer equipped with an electrospray ionization (ESI) source. The negative-ion ESI mass spectrum of unprocessed diphosphoryl lipid A is shown in Figure 6.2. Labeled major peaks indicate intact, deprotonated lipid A molecules, $[M-H]^-$. Figure 6.3 shows possible molecular structures with variations in non-stoichiometric substitutions. To obtain

clearer results, further ESI-MS measurements were carried out with synthetic monophosphoryl lipid A with a well-defined molecular mass and structure, as shown in Figure 6.1b.

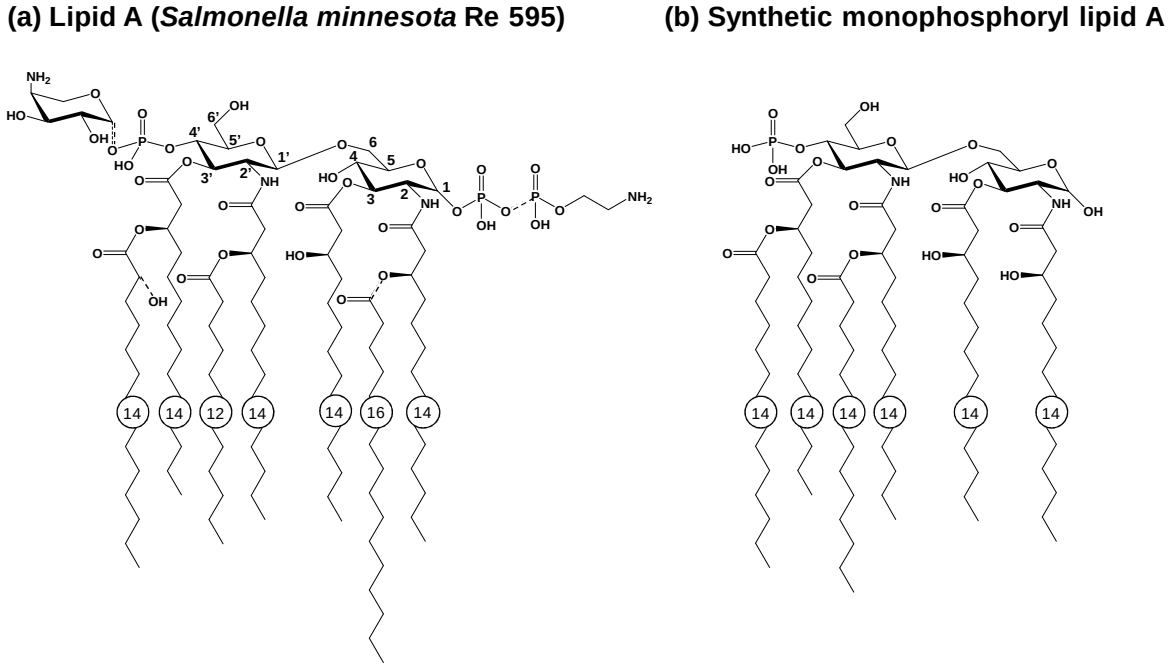

Figure 6.1 Chemical structure of (a) *Salmonella minnesota* Re 595 Lipid A, (b) synthetic monophosphoryl lipid A.

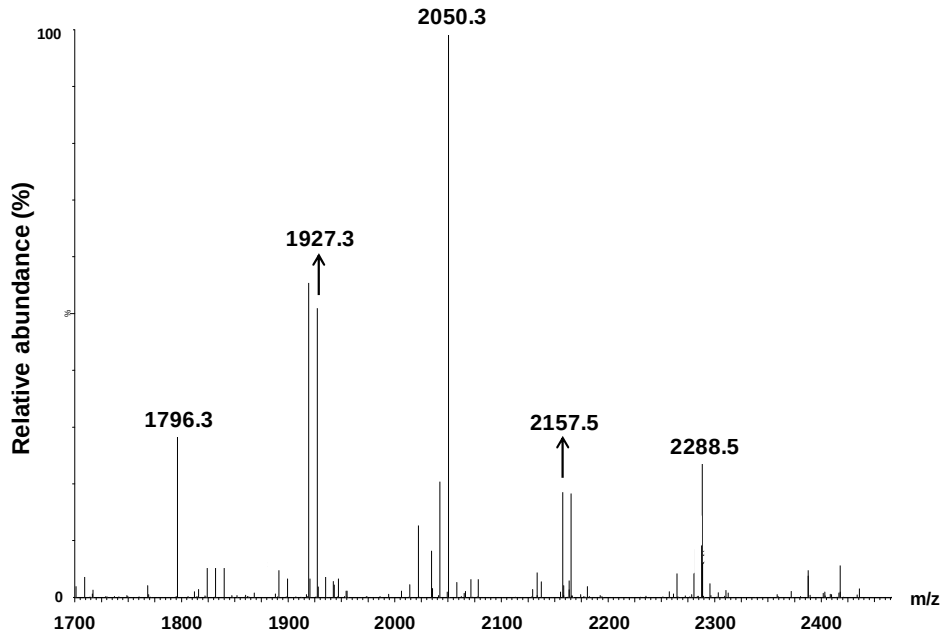

Figure 6.2 ESI mass spectrum of unprocessed diphosphoryl lipid A.

(a) $C_{94}H_{178}N_2O_{25}P_2$, exact mass: 1797.2

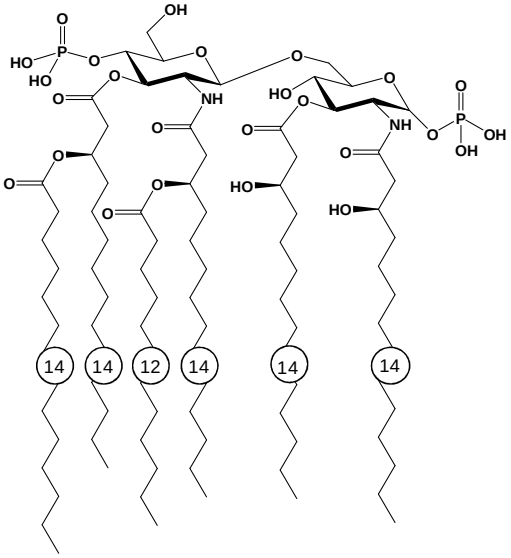

(b) $C_{99}H_{187}N_3O_{28}P_2$, exact mass: 1928.3

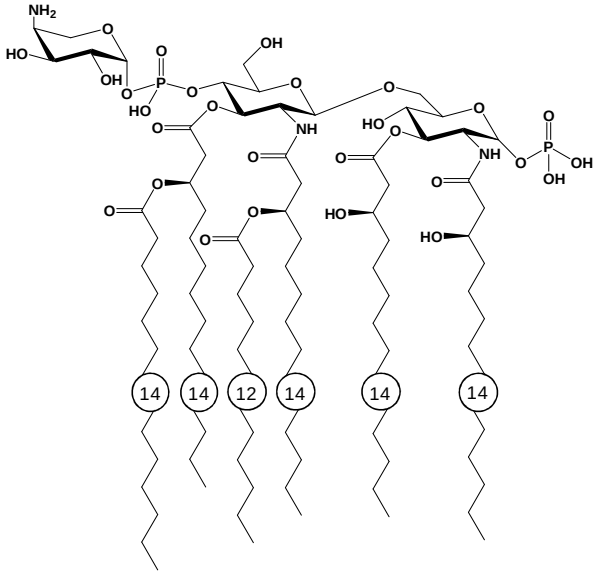

(c) $C_{110}H_{208}N_2O_{27}P_2$, exact mass: 2051.4

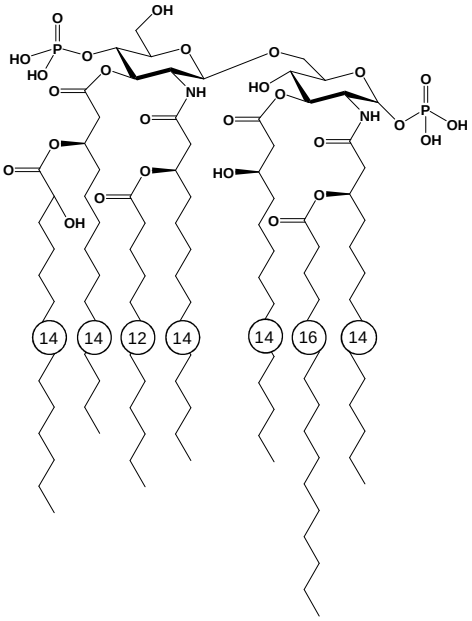

(d) $C_{101}H_{193}N_4O_{31}P_3$, exact mass: 2051.3

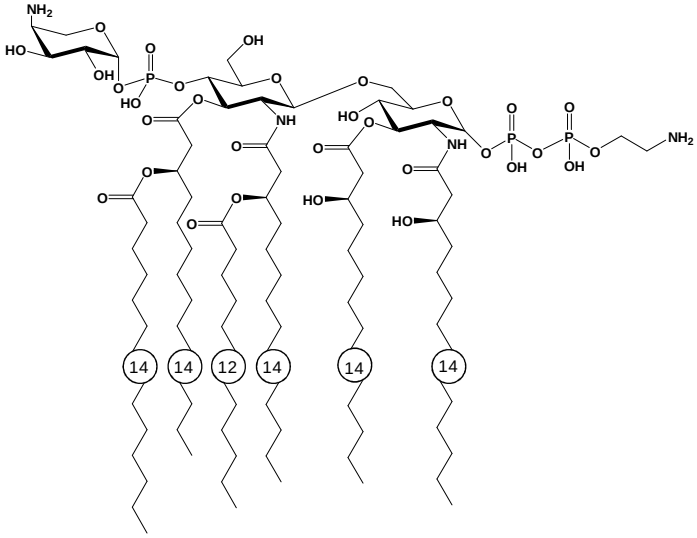

(e) $C_{112}H_{214}N_3O_{29}P_3$, exact mass: 2158.5 (f) $C_{117}H_{223}N_4O_{32}P_3$, exact mass: 2289.5

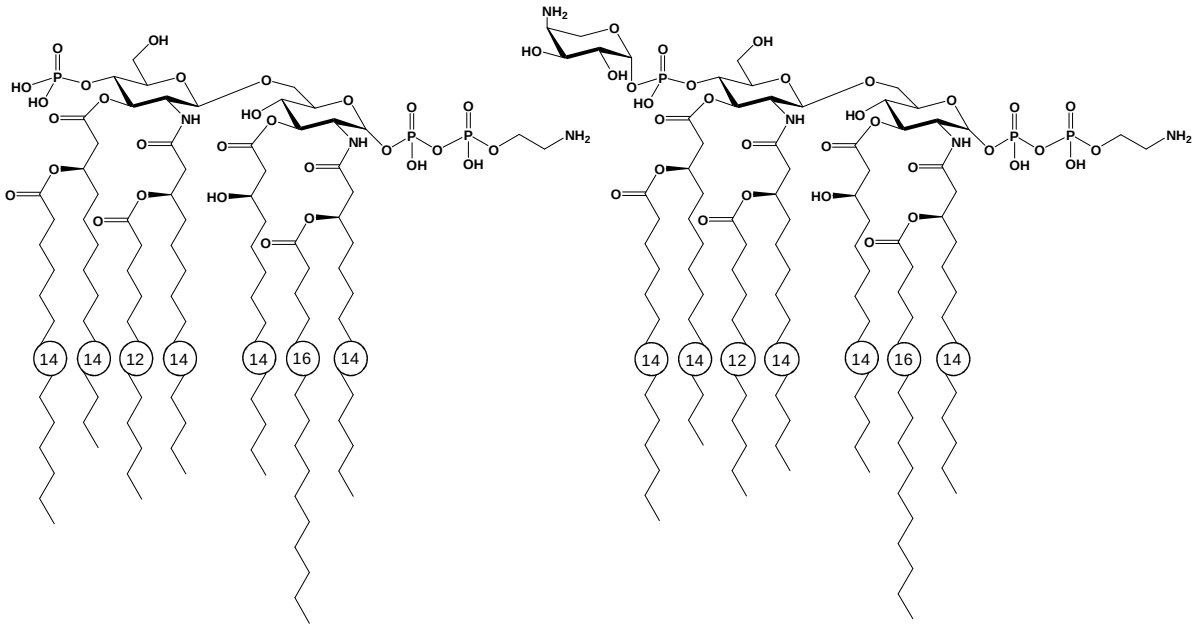

Figure 6.3 Chemical structure and molecular weight of *Salmonella minnesota* Re 595 Lipid A with variations in non-stoichiometric substitutions.

The surface morphology of spotted lipid A film was imaged by atomic force microscopy (AFM) in tapping mode. Figure 6.4 shows a typical image of lipid A prepared by spotting 10 µl of 1 mg·ml^{-1} lipid A solution. Spotting did not form a continuous lipid A film on the silicon substrate. Instead, lipid A formed island-like aggregates where some bare silicon surfaces were still exposed. The surface coverage was estimated to be 50%.

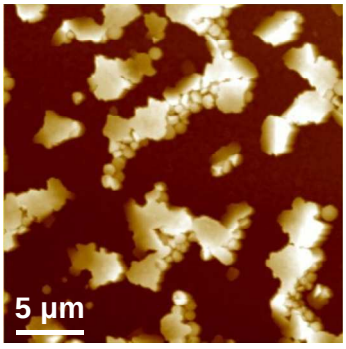

Figure 6.4 Spotted lipid A formed island-like aggregates and some bare silicon surfaces were still exposed (brown). The surface coverage was estimated to be 50%. The color scale of the image is 1.5 µm.

The details of the beam system are described in Chapter 2. The beam sources used in this study were the VUV source and the radical source. The schematic of the system setup is shown in Figure 6.5. The VUV source had a working distance of 5.4 cm to the sample position. The photon flux at the sample position was calculated to be ~1.37×10^{14} photons·cm^{-2}·s^{-1} (±10%). 1 h of VUV irradiation resulted in a fluence of ~4.9×10^{17} photons·cm^{-2} (±10%). VUV experiments were conducted at normal incidence. Oxygen and deuterium radicals were generated by a thermal gas cracker. The source was operated at a power of 60 W for both oxygen and deuterium. The absolute radical flux at the sample position was characterized by threshold ionization mass spectrometry (TIMS). The typical oxygen radical flux was ~7.5×10^{13} oxygen·cm^{-2}·s^{-1} (±10%), and the typical deuterium radical flux was ~4.6×10^{13} deuterium·cm^{-2}·s^{-1} (±10%).

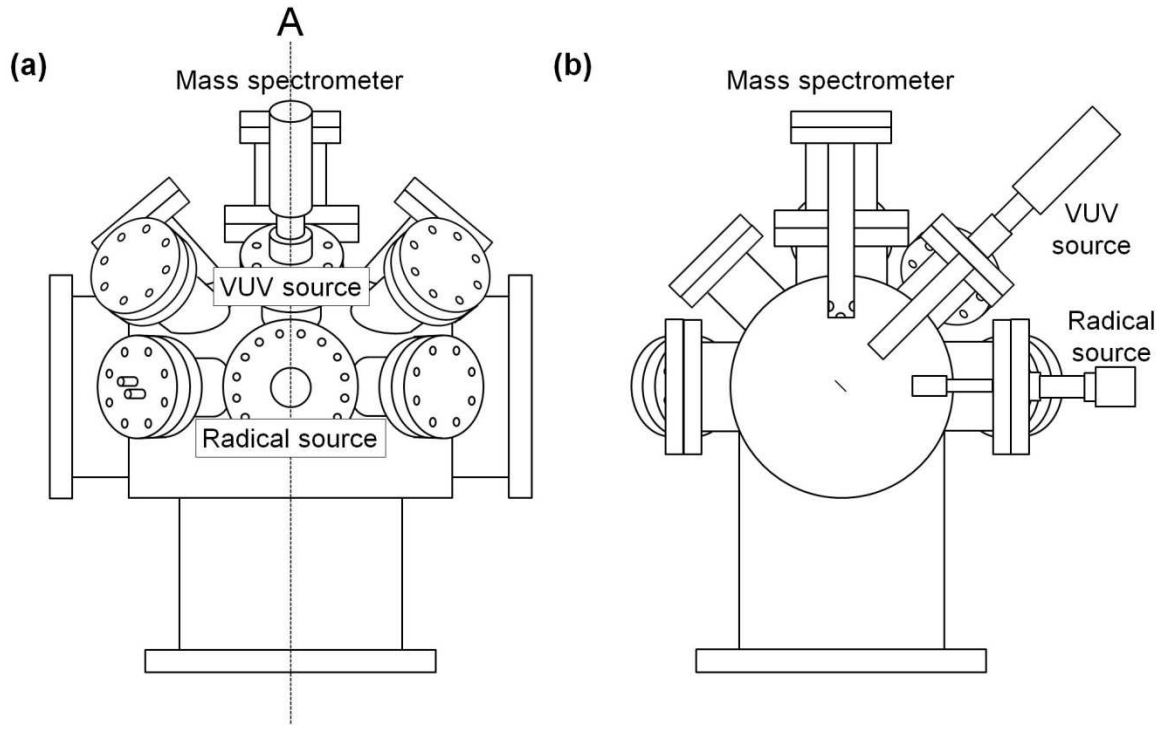

Figure 6.5 (a) Side view of the beam system (b) cross section view of the beam system at plane A labeled in (a).

The effects of beam exposures on lipid A samples were characterized with various analysis tools. Endotoxic activity measurements were conducted by the human whole blood tests. Bulk chemical modification was characterized with ex situ transmission Fourier transform infrared (FTIR) spectroscopy. VUV photolysis products were monitored by in situ mass spectrometry. The quartz crystal microbalance (QCM) was used to monitor the in situ mass removal during exposure. To obtain structural information of lipid A film bulk, unprocessed and VUV-exposed lipid A samples were analyzed using ESI-MS. Lastly, time-of-flight secondary ion mass spectrometry (ToF-SIMS) was performed with a secondary ion mass spectrometer to probe the film surface structural modification.

6.4 Endotoxic Activity Measurements

Figure 6.6 shows the endotoxic activity of unprocessed and processed lipid A samples, which was monitored by measuring the secreted IL-1β in human whole blood.

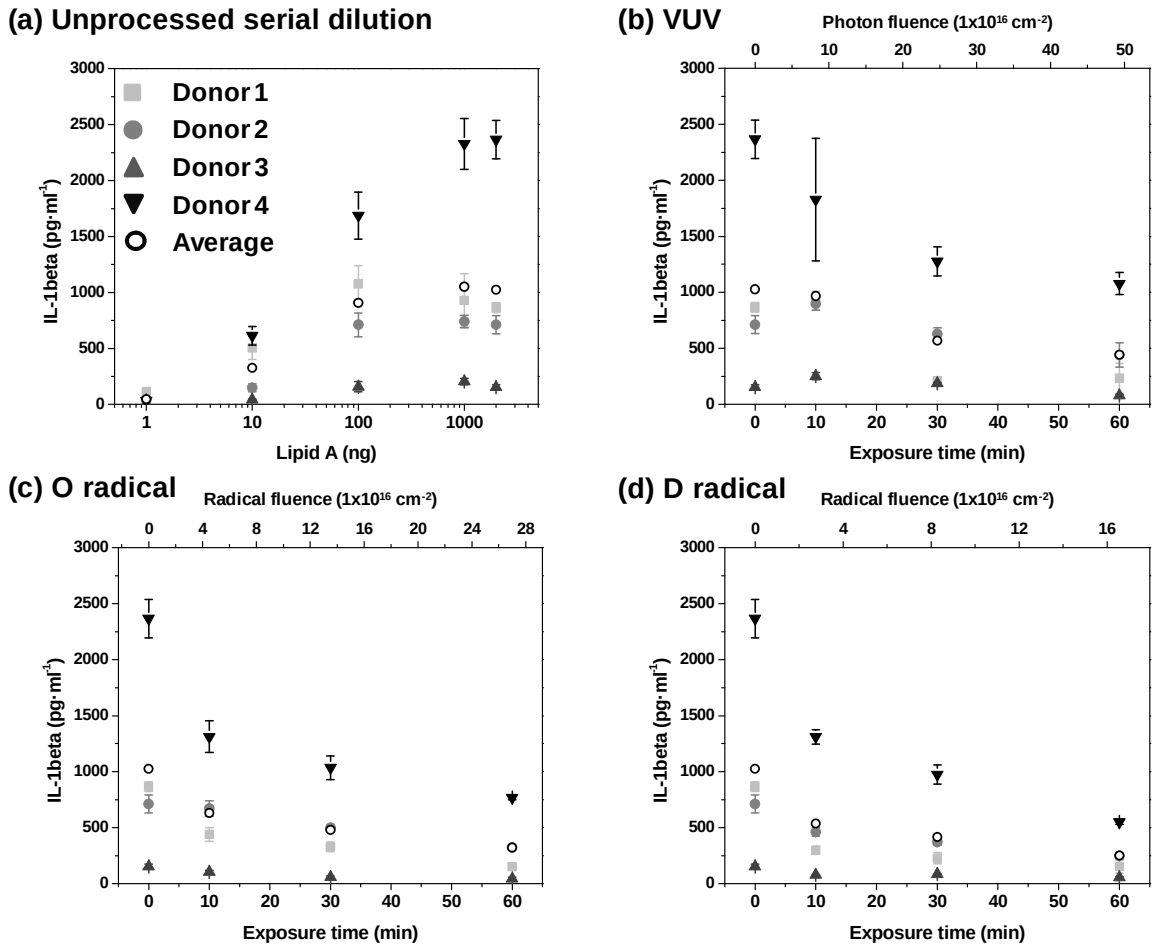

Figure 6.6 Endotoxic activity monitored by secreted IL-1β in human whole blood assay. Blood from 4 healthy donors were incubated with (a) unprocessed serial dilution, (b) VUV-processed, (c) O radical-processed, and (d) D radical-processed lipid A samples. The error bar for each data point stands for the standard deviation from 3 independent samples tested with blood from the same donor.

We report results obtained from 4 healthy blood donors. For each donor, tests on serial unprocessed lipid A samples were performed, as shown in Figure 6.6a. Samples were prepared by spotting serially diluted lipid A solution on UV/ozone-cleaned silicon substrates. Spotting 10 μl of 0.2 mg·ml^{-1} lipid A solution resulted in 2000 ng of lipid A films on the substrate. Similarly, 1 ng lipid A films were prepared by spotting 10 μl of 100 ng·ml^{-1} lipid A solution. UV/ozone-cleaned bare silicon did not activate IL-1β secretion. We note that the LPS/lipid A stimulation response from circulating leukocytes varies largely from individual to individual. As shown in Figure 6.6a, the secreted interleukin increases with increasing amount of lipid A and saturates at

~100 ng for donor 1 to 3 and ~1000 ng for donor 4. When the blood is stimulated with 2000 ng of lipid A, the difference between the highest responder (donor 4) and the lowest responder (donor 3) is about 15-fold. Wurfel et al. reported that under the same stimulation condition, IL-1β concentration, measured from 102 normal subjects, could differ by as much as 40-fold from the highest to the lowest responders, placing our results well within this range.[78]

Processed lipid A samples were prepared by spotting 10 μl of a 0.2 $mg \cdot ml^{-1}$ lipid A solution on UV/ozone cleaned silicon substrates and treated with various beam exposures. The results of endotoxic activity change after beam exposures are shown in Figure 6.6b, c, and d for VUV, oxygen radical, and deuterium radical exposures, respectively. After 60 min of VUV exposure (4.9×10^{17} photons$\cdot cm^{-2}$), the average IL-1β concentration decreases to ~45% of the unprocessed samples. For oxygen and deuterium radical exposures, the average IL-1β concentration decreases with increasing exposure time. 60 min of oxygen or deuterium radical exposure (2.7×10^{17} oxygen$\cdot cm^{-2}$; 1.7×10^{17} deutrium$\cdot cm^{-2}$) decreases the average IL-1β concentration to ~31 and ~25% with respect to the unprocessed samples. Photon and radical fluxes generated in our beam system are smaller compared to that generated by a typical plasma condition. A fluence received after 60 min of beam exposure is typically equivalent to a few minutes of a plasma exposure. [38, 82]

It is noted that there are larger variations for 10 min VUV exposures. For low responders, IL-1β secretion increases somewhat compared to unprocessed samples. We hypothesize that the increased IL-1β secretion is due to the NALP3-inflammasome pathway.[160] NALP3 belongs to the family of intracellular receptors. It can recognize various non-microbial “danger” or “damage” signals, such as monosodium urate crystals (MSU), calcium pyrophosphate dihydrate, and reactive oxygen species (ROS), to name a few. The measured IL-1β is the sum of both cell surface receptor TLR-4 pathway and intracellular receptor NALP3 pathway. Molecular fragments resulting from VUV exposures are suspected to induce the NALP3 pathway. In short term exposures, the suppression of TLR-4 pathway might not be sufficient to counteract the onset of NALP3 pathway, especially for low responders. Following this scenario, for longer exposure time, the TLR-4 pathway is further diminished due to the extensive damage of lipid A molecules, and thus the overall IL-1β secretion is inhibited.

We emphasize here that Lipid A films are not readily soluble in human whole blood, and thus the human whole blood assay used in this study mainly monitors the change of the lipid A film surface, where leukocytes contact the material. This assay suggests that under the same order of magnitude of total fluence, radicals have better efficacy in damaging the immediate surface of lipid A films. We will present and discuss the individual species effect in the following sections.

6.5 VUV-induced Photolysis

Transmission FTIR was used in this study to monitor the bulk chemical change caused by beam exposures. The FTIR spectra of lipid A film after VUV exposure are shown in Figure 6.7.

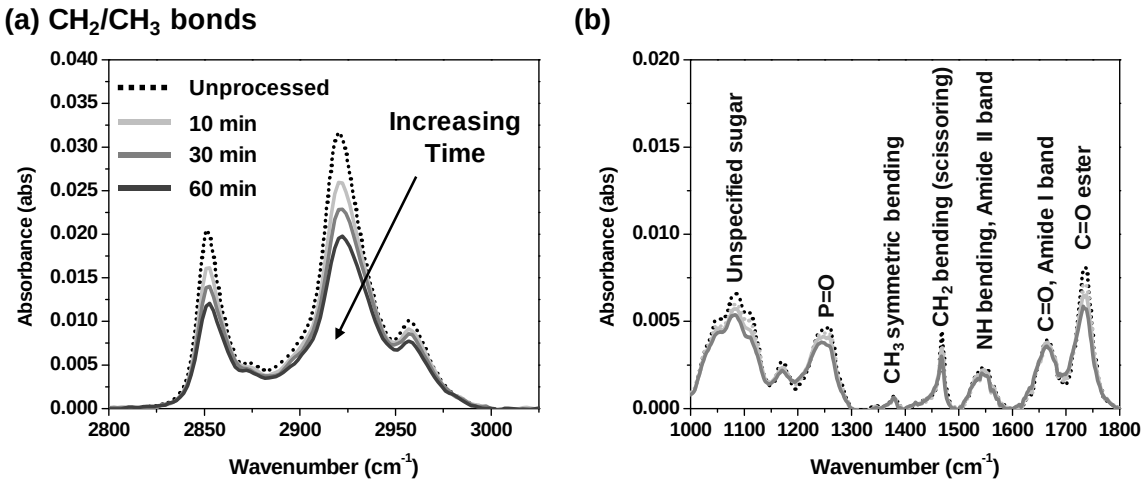

Figure 6.7 Transmission FTIR spectra of lipid A after VUV exposure: (a) CH_2/CH_3 bonds (2800-3025cm^{-1}), (b) 1000-1800 cm^{-1}. The absorbance scale is different in (a) from (b). Each condition is an average of three independent measurements.

The exposure time was increased from 10 to 60 min, resulting in a VUV fluence of 8.2×10^{16} to 4.9×10^{17} photons·cm^{-2}, respectively. The most prominent absorption peak loss is observed in the CH_2/CH_3 region (2800-3025 cm^{-1}), corresponding to the symmetric/asymmetric stretching of aliphatic chains in lipid A (Figure 6.7a). These aliphatic moieties are attached to the disaccharide backbone by amide and ester linkages (Figure 6.1a). Examining the absorption peaks for amides and esters, it is observed that while amide linkages remain relatively unchanged, the ester linkages suffer significant loss (Figure 6.7b). Besides ester and aliphatic moieties, signal loss is also observed from phosphate and sugar regions. Moreover, the absorption peak loss increases with exposure time.

Figure 6.8 shows the normalized absorption peak plotted against VUV exposure time for both ester C=O (1736cm^{-1}) and CH_2 asymmetric stretching (2920cm^{-1}). First, based on the loss fraction of CH_2 and ester peaks (~30%), we estimate VUV photons penetrate ~200 nm into the film after a 1 h exposure, roughly one third of the original thickness. This is consistent with the penetration depth of VUV photons in polymeric materials, from 15 to 250 nm, depending on VUV wavelength and polymer structure.[118] Second, ester and CH_2 peak loss is highly correlated, suggesting that damage of ester linkages results in desorption of aliphatic chains. Third, the loss rate decreases over time, indicating a higher material removal rate (etch yield) at the beginning of irradiation.

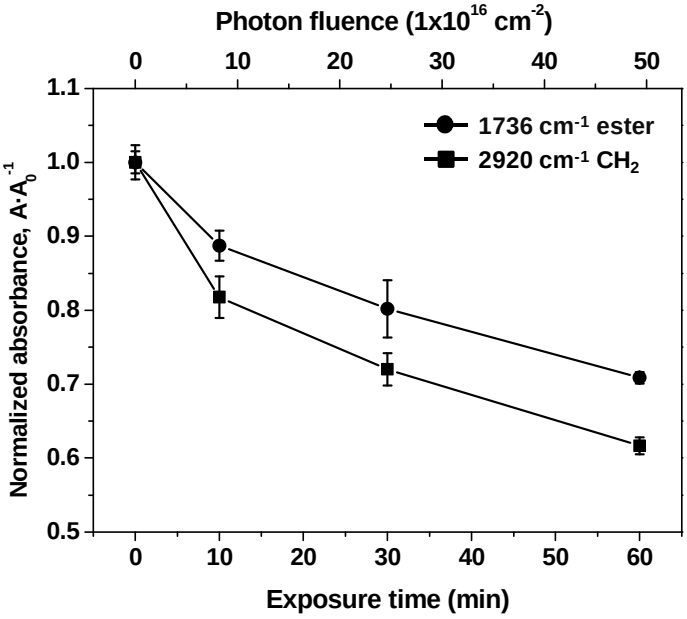

Figure 6.8 Normalized absorbance of ester C=O (1736 cm^{-1}) and CH_2 asymmetric stretching (2920 cm^{-1}) for different VUV exposure time.

An in situ QCM measurement of lipid A under VUV exposure is shown in Figure 6.9.

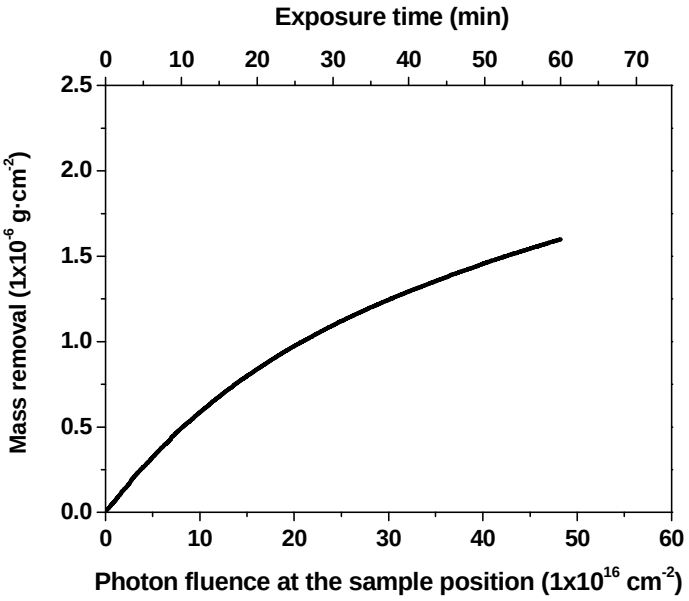

Figure 6.9 In situ QCM measurement of lipid A mass removal under VUV exposure. The slope of the QCM curve is proportional to the instantaneous etch yield. The etch yield is higher at the beginning of exposure and decreases with longer exposure time.

Mass removal is plotted versus VUV fluence at the sample position. The slope of the QCM curve is proportional to the instantaneous etch yield. The etch yield is higher at the beginning of exposure and decreases with longer exposure time. This is consistent with FTIR results (Figure 6.8). Accounting for the 50% surface coverage of lipid A film, we calculate the equivalent carbon etch yield under VUV irradiation. The initial etch yield is ~0.67 C·photon^{-1}, and it decreases to ~0.15 C·photon^{-1} towards the end of exposure.

The residual gas mass spectrum of lipid A is shown in Figure 6.10. The spectrum was taken after 1 min of VUV exposure with a VUV fluence of ~8×10^{15} photons·cm^{-2}. Except for subtraction of the background signal, no further signal processing was performed. We observe several main photolysis products, including H_2 (m/z = 2), H_2O (m/z = 18), CO (m/z = 28), CO_2 (m/z = 28, 44). Peak clusters from m/z = 40-100 are separated by about 14 amu intervals. We attribute these peaks to the cracking pattern of alkane/alkene with 11, 13, or 15 carbons.[70] The results from FTIR and in situ mass spectrometry indicate that VUV photons cleave the ester linkages to the penetration depth and generate CO_2 and corresponding aliphatic moieties of lipid A. Generation of H_2 and H_2O indicates that hydrogen abstraction and damage of sugar backbone also take place.

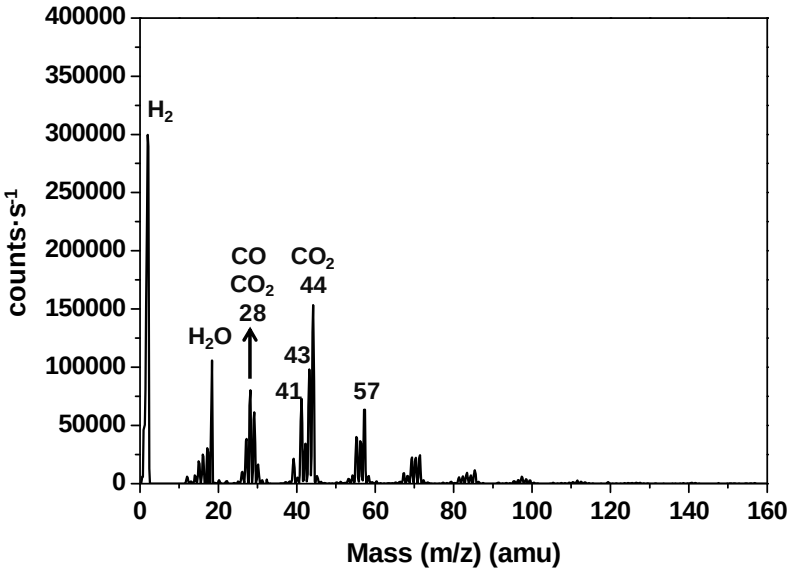

Figure 6.10 Residual gas mass spectrum of lipid A after 1 min of VUV exposure. The main photolysis products are H_2, H_2O, CO, CO_2, and desorbed aliphatic moieties.

ESI-MS was used to identify the compounds remaining on the silicon substrate after VUV exposure. The diphosphoryl lipid A, obtained by hydrolysis of Re mutant LPS, was observed as a mixture with various non-stoichiometric substitutions and molecular masses, as shown in Figure 6.2. In order to obtain a clearer result, we performed further ESI-MS measurements using synthetic monophosphoryl lipid A with a well-defined molecular mass and structure. Negative-ion ESI mass spectra of vacuum-processed and VUV-exposed synthetic lipid A are shown in Figure 6.11. The ion at m/z = 1745.3 corresponds to the intact, deprotonated lipid A, $[M-H]^-$. As shown in Figure 6.11, the abundance of intact lipid A recovered from the spotted

film decreases with VUV exposure. The loss rate of lipid A is most significant at the beginning of the exposure, consistent with previous FTIR and QCM measurements. ESI is a soft ionization method that, when operated in the negative ion mode, can transfer intrinsic negative ions from liquid phase (chloroform/methanol/water solution) to gas phase. Primarily, the molecules with phosphate groups were detected in the mass range 1100-2000 Da in our measurements. For 30 and 60 min VUV-exposed samples, solid residues that could not be resuspended were observed on the silicon substrate, indicating that some insoluble carbon-rich materials and/or cross-linking products were formed upon VUV exposure.

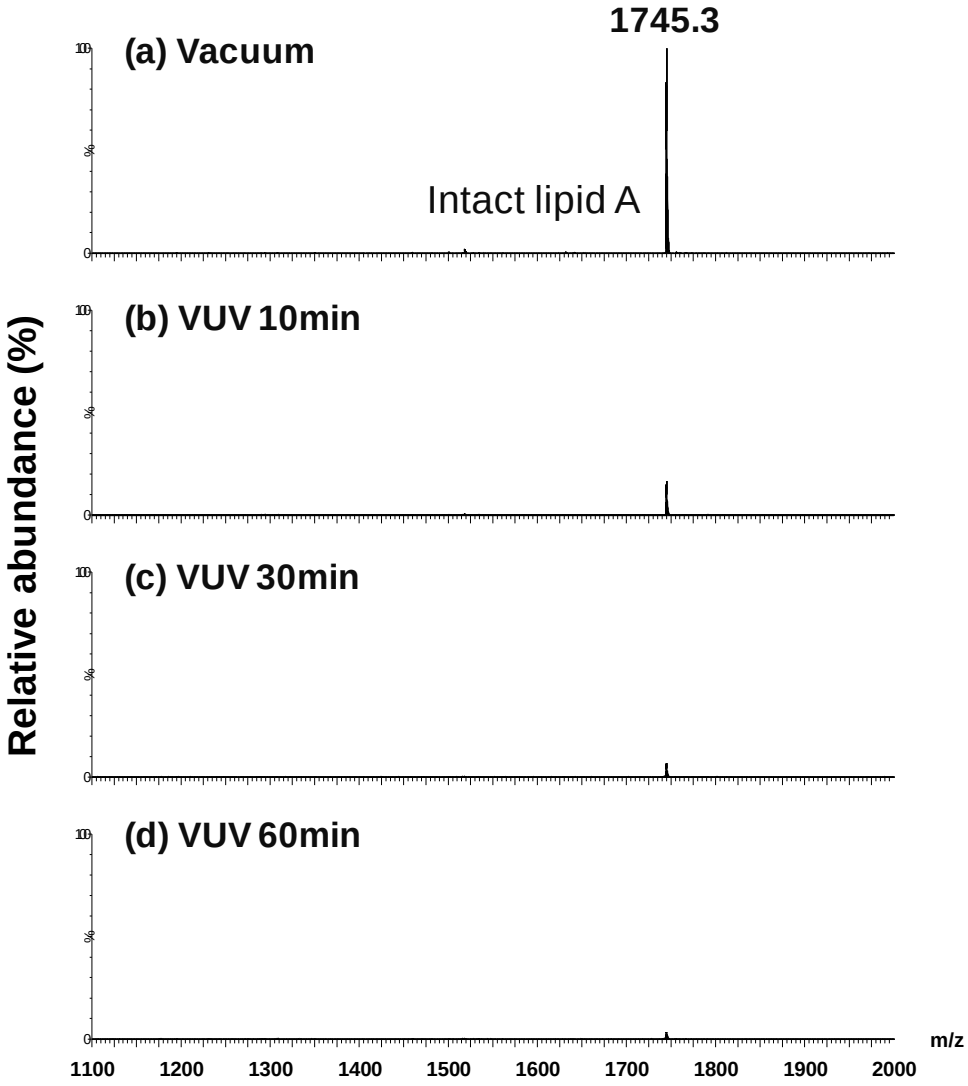

Figure 6.11 ESI mass spectra of monophosphoryl lipid A after (a) 60 min vacuum, (b) 10 min VUV, (c) 30 min VUV, and (d) 60 min VUV exposure. All the spectra are normalized to the highest intensity peak in the vacuum processed sample. The abundance of intact lipid A decreases after VUV exposure.

Altogether, the results obtained from FTIR, in situ QCM, in situ residual gas analysis, and ESI-MS show that VUV photons cause bulk modification to the penetration depth. 147 nm VUV mainly attacks the ester linkages and results in desorption of aliphatic chains. Loss of phosphate groups and damage of disaccharide backbones are also observed. The abundance of intact lipid A molecules in the film is greatly reduced after VUV exposure. The removal and damage of lipid A molecular structure contribute to the decrease of endotoxic activity, as shown in Figure 6.6b.

6.6 Oxygen and Deuterium Radical-induced Chemical Etching and Surface Modification

Radical exposures result in reactions at the surface of lipid A films, and thus the bulk properties are unaffected. Transmission FTIR is a bulk analysis technique, and measurements on radical-exposed samples (1 mg·ml^{-1}, 10 μl) show little change of absorption spectra, as shown in Figure 6.12.

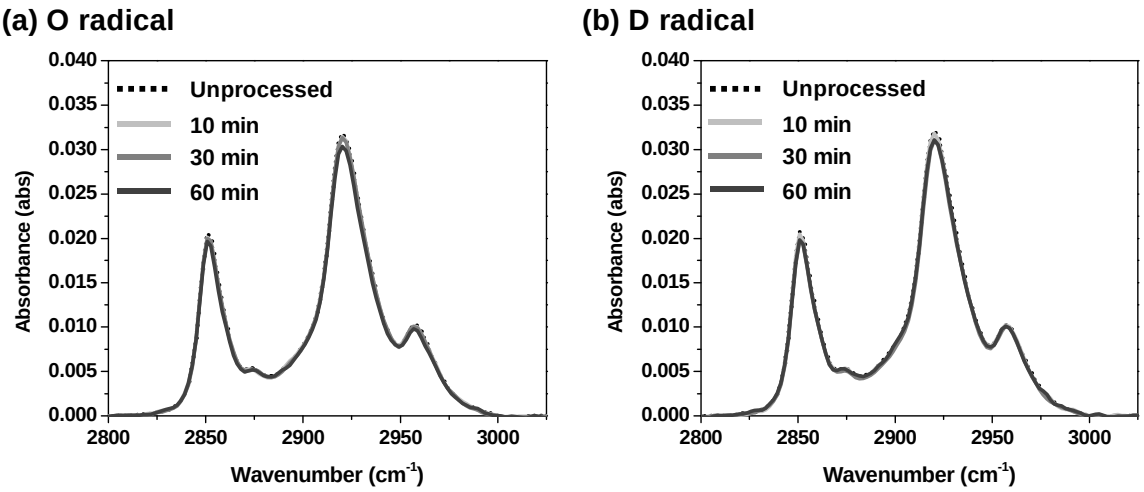

Figure 6.12 Transmission FTIR spectra of lipid A CH_2/CH_3 bonds (2800-3025cm^{-1}) after (a) O radical, (b) D radical exposure.

As shown in Figure 6.13, simultaneous VUV and radical exposures indicate that bulk chemical change is dominated by VUV photolysis. No enhanced bulk material removal is achieved by simultaneous exposure to radicals and VUV photons.

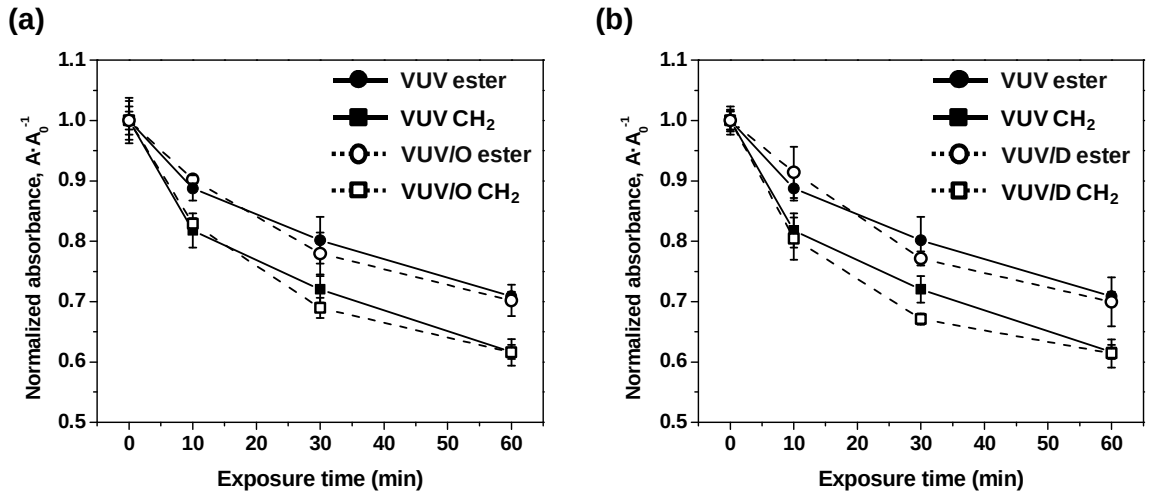

Figure 6.13 Normalized absorbance of ester C=O (1736 cm^{-1}) and CH_2 asymmetric stretching (2920 cm^{-1}) with different exposure time for (a) VUV-only and simultaneous VUV/O, (b) VUV-only and simultaneous VUV/D.

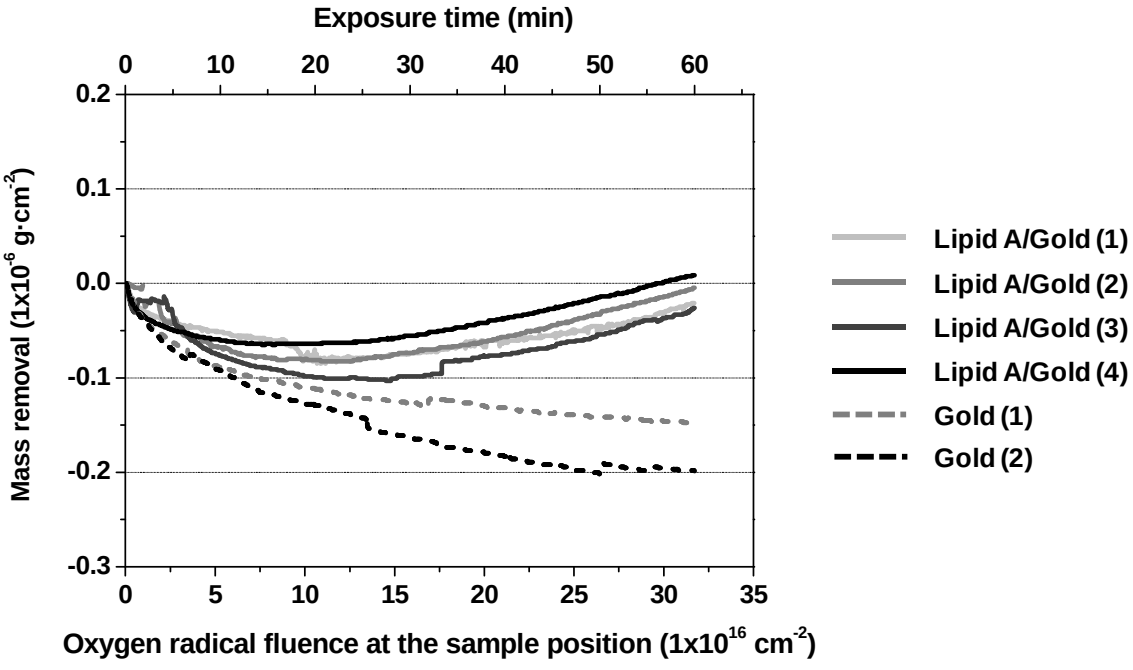

Figure 6.14 In situ QCM measurements of lipid A mass removal under oxygen radical exposure.

In situ QCM measurements of lipid A under oxygen radical exposure are shown in Figure 6.14. Mass removal is plotted versus oxygen radical fluence at the sample position. Mass addition (negative mass removal) is observed with pristine QCM sensors (gold electrode). It can be attributed to oxygen radical adsorption and oxidation of gold.[161] With lipid A spotted on QCM sensors, oxygen radical exposure causes mass addition followed by mass removal. The estimated surface coverage of spotted lipid A on QCM sensors is 50%. Under this condition, oxygen radicals etch away lipid A (mass removal) and adsorb/oxidize the exposed gold surface (mass addition) at the same time. The mass addition rate is higher than the mass removal rate in the beginning. After oxygen adsorption and gold oxidation are saturated, the net mass change is mostly due to chemical etching of lipid A. Assuming that the etch rate of lipid A is constant and accounting for the 50% surface coverage of lipid A film, we calculate the lipid A etch yield to be ~0.04 C·oxygen^{-1}. This is in reasonable agreement with published Kapton (polyimide) etch yields.[162]

Measurements of deuterium radical impact on lipid A film show a mass change within the uncertainty limit of our QCM setup, which is about 8.3×10^{-4} Hz·s^{-1}. Using this value as an upper limit, we estimate a maximum etch yield of 0.02 C·deuterium^{-1}. Hydrogen radical-induced chemical erosion of amorphous hydrogenated carbon (a-C:H) films has been extensively studied because of the interaction of hydrogen plasmas with carbon surfaces in thermonuclear fusion devices.[163] Utilizing a thermal deuterium beam, Vietzke et al. reported an etch yield of ~0.01 C·deuterium^{-1} at ~300 K.[164] Erradi et al. reported an etch rate of a-C:H films by hydrogen plasma-generated atomic hydrogen (1.9 hydrogen·nm^{-2}·s^{-1}) that was roughly 0.001 nm·s^{-1} at 305 K.[165] The calculated etch yield is ~0.05 C·hydrogen^{-1}, based on the estimated mass density of a-C:H films ~1.9 g·cm^{-3}.[166] Our estimated maximum etch yield is in reasonable agreement with literature.

The radical-induced etch yield is relatively low compared to measurements made with 147 nm VUV photons (the initial etch yield is ~0.67 C·photon^{-1}, and it decreases to ~0.15 C·photon^{-1} towards the end of exposure); however, radical-induced chemical etching is expected to modify the surface of lipid A films. ToF-SIMS was used to probe the film near-surface region (1-2 nm). Figure 6.15 shows the partial negative ion spectra of unprocessed lipid A film (*Salmonella minnesota* Re 595). Important fragments from intact lipid A molecules are observed, including phosphoryl groups: PO_2^- (m/z = 62.9), PO_3^- (m/z = 78.9), $H_2PO_4^-$ (m/z = 96.9), pyrophosphate groups: $HP_2O_6^-$ (m/z = 158.9), $H_3P_2O_7^-$ (m/z = 176.9), and fatty acid moieties: $C_{12}H_{23}O_2^-$ (m/z = 199.1), $C_{14}H_{27}O_2^-$ (m/z = 227.2). The peak assignment of phosphoryl and fatty acid fragments follows that of Kylián et al.[74] Pyrophosphate groups originate from the non-stoichiometric phosphorylethanolamine (pEtN) substitution (Figure 6.1a) and are assigned according to Seid et al. and Jones et al.[167, 168] Jones et al. have also suggested that the presence of pyrophosphate in diphosphorylated lipid A is a general phenomenon among Gram-negative bacteria.

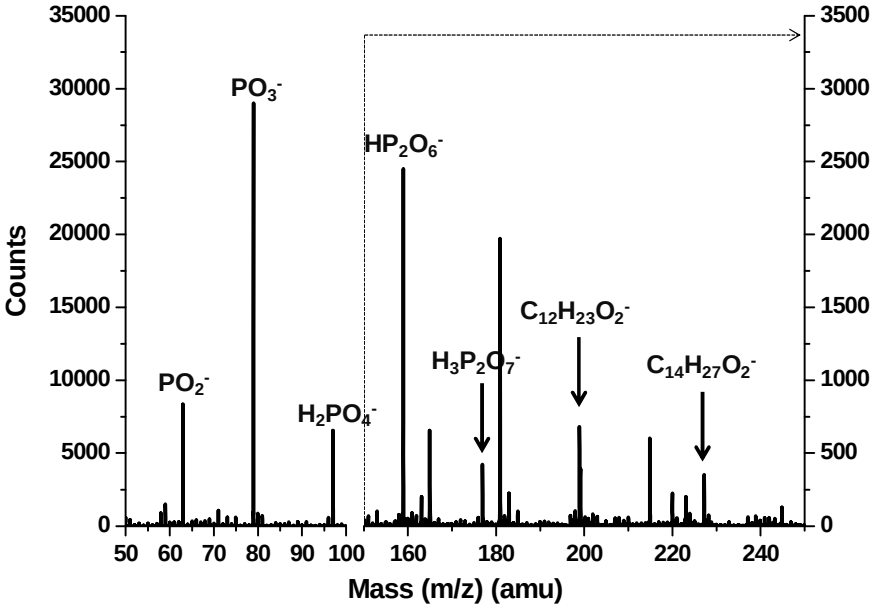

Figure 6.15 Partial negative ion ToF-SIMS spectra of unprocessed lipid A film. Note that the counts scale is different from m/z = 50-100 to m/z = 150-250.

Samples processed with VUV photons, oxygen and deuterium radicals were also analyzed by ToF-SIMS. Figure 6.16 shows the compiled results comparing the change of phosphates, pyrophosphates, and fatty acids, which are important factors governing the endotoxic activity of lipid A. As shown in the FTIR spectra (Figure 6.7), VUV exposure results in removal of CH_2/CH_3, esters, and phosphate groups from bulk material, which is also observed from surface sensitive SIMS measurements. Phosphates, pyrophosphates, and fatty acid peaks all decrease after 60 min of VUV exposures. In spite of low etch yield, oxygen and deuterium radical-exposed samples show significant modification at lipid A film surface. Phosphates, pyrophosphates, and fatty acid groups all decrease to an extent even lower than that of VUV-processed samples. Specifically, oxygen radical attacks the aliphatic moieties, which leaves little intact fatty acids on the film surface. ToF-SIMS measurements strongly support the results obtained from the human whole blood assay, in which the entodoxic activity of lipid A is greatly reduced after radical exposures (Figure 6.6c and d).

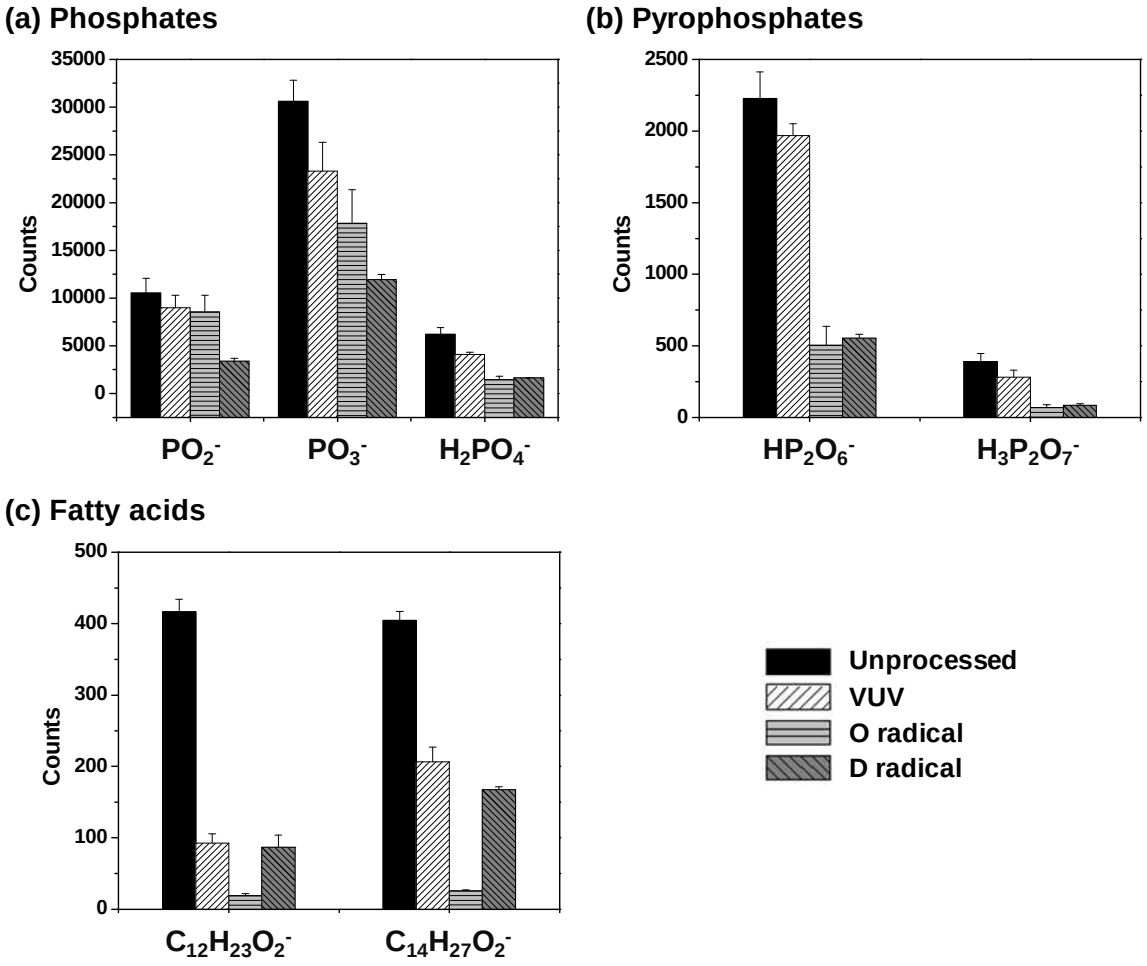

Figure 6.16 The change of characteristic ToF-SIMS peaks of (a) phosphates, (b) pyrophosphates, and (c) fatty acids with various exposure protocols. The exposure time for each condition was 60 min, resulting in the species fluence of 4.9×10^{17} photons·cm^{-2}, 2.7×10^{17} oxygen·cm^{-2}, and 1.7×10^{17} deuterium·cm^{-2}. The results indicate surface modification caused by VUV photons and radicals.

6.7 Discussion

We have shown that 147 nm VUV photons, oxygen radicals, and deuterium radicals can cause modification and mass removal of lipid A, which contribute to the decrease of endotoxic activity. The underlying mechanism for each species can be understood from extensive studies on modification and erosion/etching of polymers and a-C:H materials.

As mentioned earlier, VUV photons can penetrate into the bulk of polymer film, up to a few hundred nanometers, depending on the absorption coefficient of the polymer at specific wavelengths.[118] Yuan et al. reported that VUV exposure on poly(methyl methacrylate)

(PMMA) results in mainly Norrish type I ester side group photolysis.[169] Volatile products, such as CO, CO_2, formaldehyde, methyl formate, and methane were detected.[115, 116] It was also recognized in the semiconductor industry that plasma-generated VUV causes severe degradation of 193 nm photoresist, a methacrylate-based polymer. Loss of carbonyl groups, such as ester and lactone, was observed.[50, 80, 81] Damage of ester linkages then leads to desorption of pendant groups.[170] This is because the ester and lactone species have higher photon absorption cross sections than alkane and alkene in the VUV region.[152-155] VUV penetration in methacrylate-based photoresist has been simulated and verified by experiments.[119] Those results are consistent with what we have observed in lipid A photolysis. For 147 nm photons, we estimate a penetration depth of ~200 nm in lipid A, based on the loss fraction of CH_2 and ester FTIR absorption peaks. Damage of ester linkages corresponds well with the loss of aliphatic moieties, which were detected as photolysis products. The higher etch yield at the beginning of the exposure can be explained by photons rapidly cleaving the ester linkages in the near-surface region of lipid A films. Desorption of aliphatic groups allow photons to further penetrate and release materials in the bulk, since the remaining bonds (C-C, C-H, and amides) have a lower absorption cross section at 147 nm.[152-155, 171] The decreasing etch yield is the result that fewer ester groups are available and VUV photons are ultimately absorbed by these remaining bonds when photons penetrate deeper into the film. Photolysis-induced damage of lipid A is similar to that of methacrylate-based polymers. It suggests the similarity of ester-containing materials under VUV exposure, where damage of ester linkages and removal of pendant groups are the main photolysis mechanisms.

In contrast, radical reaction takes place at the very surface of lipid A films, so the bulk properties are unaffected. Polymer degradation upon oxygen radical exposure is initiated by the hydrogen abstraction pathway. Abstraction of hydrogen by oxygen radicals forms radical sites ($R\cdot$) and hydroxyl radicals ($OH\cdot$). These radical sites ($R\cdot$) can react with subsequent oxygen radicals yielding alkoxy radicals ($RO\cdot$), which are the precursors of polymer chain scission. The radical sites ($R\cdot$) can also react with ground state molecular oxygen to form peroxy radicals ($ROO\cdot$), when the relative density of atomic oxygen is low. These peroxy radicals can subsequently form hydroperoxides (ROOH) through hydrogen transfer from the same or nearby chain and create new alkyl radical sites ($R'\cdot$) to propagate the oxidation reaction. Hydroperoxides can also be reorganized into more stable functionalities such as ketones, aldehydes, and vinyl groups. These reactions lead to polymer chain scission and mass removal through volatile products, such as CO and CO_2.[172-175] The nature of oxygen-containing functional groups on the surface has been probed with x-ray photoelectron spectroscopy and SIMS, which indicate the surface is degraded and oxidized.[162, 174] The etch rate is dependent on chemical structure of polymers and surface temperature.[162, 176] The lipid A etch yield measured in our setup is ~0.04 $C\cdot oxygen^{-1}$, which is in reasonable agreement with published Kapton (polyimide) etch yields.[162] The intact fatty acid moieties are almost fully diminished from the film surface after atomic oxygen exposure (Figure 6.16c), suggesting that oxygen radicals readily attack and damage these aliphatic chains.

On the other hand, hydrogen radical-induced chemical erosion of a-C:H films can be used to understand the modification and mass removal of lipid A. Vietzke et al. reported that the main reaction product of a-C:H films upon hydrogen radical exposure was CH_3 radicals. Higher hydrocarbons such as C_2H_x and C_3H_x were also observed. In the case of atomic deuterium, exposures resulted in isotope exchange and predominant formation of deuterocarbons and

HD.[177, 178] The important reactions include abstraction of bonded hydrogen from a sp^3 CH_x group, hydrogenation of sp and sp^2 unsaturated carbon atoms to sp^3 hybridization, and chemical erosion through volatile products. The hydrogen abstraction proceeds directly between a bonded hydrogen atom and the incoming gas phase hydrogen or deuterium via an Eley-Rideal mechanism. The radical intermediate, produced during hydrogen abstraction, can recombine with another hydrogen or deuterium, or de-excite by releasing a nearby CH_3 terminal group at an elevated temperature.[163] It was also proposed that the recombination energy could be transferred to an adjacent C-C bond, resulting in cleavage of this bond. The reaction proceeds, forming CH_3/CD_3 or other hydrocarbons/deuterocarbons, and leads to chemical erosion.[178] The etch yield is temperature dependent and goes through a maximum around 650-750 K.[165, 179-181] Besides erosion, a modified layer of a thickness ~1.4 nm at the film surface was observed by ellipsometry.[165, 182] We estimate a maximum etch yield of lipid A to be ~0.02 C·deuterium^{-1}, which is in reasonable agreement with the measured etch yield reported at a temperature ~300 K.[164, 165]

F. Rossi and colleagues studied the effect of a low pressure microwave discharge afterglow on LPS and lipid A with different gas mixtures.[38, 72, 74, 75] They found that the only parameter corresponding to the change of endotoxic activity was the presence of atomic hydrogen. They suggested that VUV emitted by hydrogen-containing plasmas played a key role in deactivation. In this study, we have shown that not only VUV-induced photolysis is important, but also radical-induced chemical etching and modification are crucial. It is evident that VUV photons cause modification and material removal from the bulk of lipid A films, while the radical effect is mainly at the film surface. SIMS measurements suggest that the determining factors of lipid A activity, including the intact aliphatic chains, the phosphate and pyrophosphate groups, are all decreased after processing. Radicals cause a higher degree of surface modification compared to VUV photons, even though the overall etch yield is much lower. This observation is consistent with the surface-sensitive endotoxic activity assay, showing that radicals have better efficacy (as compared to VUV photons) in reducing the secretion of IL-1β. The partial structure of lipid A left after O/D radical beam exposures is much less active compared to intact lipid A structure. The effects of other plasma species, such as energetic ions, have to be further pursued in order to fully understand plasma and biomolecule interactions.

6.8 Conclusion

Results from vacuum beam experiments demonstrate the important aspects of lipid A deactivation under hydrogen and oxygen plasma conditions, focusing on the effects of VUV photons, oxygen and deuterium radicals. The sample analysis focuses on the change of characteristic factors governing endotoxic activity: the aliphatic/fatty acid moieties and phosphoryl groups.

VUV-induced photolysis certainly plays an important role. VUV photons cause bulk modification of exposed film to the penetration depth (~200 nm). The most prominent effect is damaging ester linkages and thus leading to desorption of aliphatic chains. Loss of phosphate groups and glucosamine backbone is also observed. The abundance of intact lipid A molecules in the film is greatly reduced after VUV exposure. By contrast, radicals cause chemical etching and modification at the surface of lipid A films. Although the etch yield is lower than that of VUV-

induced photolysis, SIMS analysis reveals that phosphate moieties and intact aliphatic chains are greatly reduced at the film surface. Human whole blood assay used in this study shows that radical exposures render a greater degree of bioactivity reduction as compared with VUV photons. This is consistent with the SIMS measurements showing that radicals cause a higher degree of surface modification.

In conclusion, plasma technology is clearly a promising option for “soft” surface sterilization and deactivation, and the results presented here show that both VUV photons and radicals can deactivate endotoxins with minimal surface damage. However, plasma technology can access a very large range of conditions, including operating at atmospheric pressure. While clearly promising, the field is still very young, and further studies of plasma interaction with biomolecules are needed to better anchor applications with scientific principles.

Chapter 7
Conclusion

By using a high vacuum beam system, this work studies the fundamental interactions of plasma-generated species and materials for two important applications, manufacturing of semiconductor devices and surface deactivation of virulent biomolecules. This chapter summarizes both studies and provides outlooks for further pursuits.

7.1 Concluding Remarks: Plasma-induced Surface Roughening of 193 nm Photoresist

The first part of this dissertation demonstrates the effects of ion bombardment, vacuum ultraviolet (VUV) irradiation, electron exposure, and moderate substrate heating in 193 nm photoresist (PR) surface roughening.

150 eV Ar ion bombardment results in physical sputtering and formation of a carbon-rich layer at the PR surface. The thickness of this surface layer is about 2 nm. Because of the similar film density and formation mechanism as tetrahedral amorphous carbon (ta-C) films grown by depositing carbon ions or Ar ion plating at comparable ion energy, this ion-modified layer is expected to bear an intrinsic compressive stress, roughly a few GPa.

In contrast, VUV irradiation modifies the PR film up to the penetration depth of photons, estimated to be ~100 nm. Oxygen-containing moieties, such as esters and lactones, are primarily damaged due to their higher photon absorption cross sections compared to C-C and C-H bonds in the VUV region of interest in this study. The damage of ester linkages then leads to desorption of pendant groups. 2-methyl-2-adamantyl methacrylate (MAMA), the leaving group of 193 nm PR, is especially sensitive to VUV exposure. Due to a terminal methyl group, the formation of a C=C double bond after cleavage of the tertiary carbon adamantyl ester of MAMA is stable. An increased adamantane vapor pressure enhances desorption and detachment of the adamantyl leaving group at higher substrate temperatures. The combined effects of polymer main chain scissioning, loss of bulky adamantyl group, and detached pendant groups acting as plasticizers in the film lead to a decreased polymer glass transition temperature (T_g) and elastic modulus (E_s).

1 keV electrons can also render bulk modification of exposed PR, up to ~100 nm. Electron-induced damage is dependent on electron fluence. Rapid depletion of oxygen-

containing bonds leads to bulk scissioning of exposed PR and decreases its T_g and E_s (< 1 $mC \cdot cm^{-2}$). On the other hand, electron-induced cross-linking starts to dominate with a higher electron fluence (> 4 $mC \cdot cm^{-2}$), where gradual abstraction of hydrogen occurs. This increases the E_s of PR.

In spite of the individual effect of ions, VUV photons, and electrons, enhanced PR surface roughening is only observed when a simultaneous exposure provides a combination of an ion-modified surface layer on top of a scissioned/softened bulk layer. This study applies a bi-layer wrinkling mechanism to qualitatively interpret the observed phenomena. The ion-modified layer undergoes both in-plane and out-of-plane displacement to relax its compressive stress. The "wrinkles" are magnified when the E_s of the bottom layer is decreased by either VUV photons or low fluence electrons.

In summary, this dissertation shows that PR structure can couple to plasma etch processes and strongly alter the post-etch morphology. While critical dimension control is a major challenge for continuous miniaturizing of semiconductor devices, close collaboration between the lithography and plasma etch community is of critical importance. It is demonstrated in the present study that the composition and structure of PRs are crucial for future design of organic mask materials and plasma processes. Although this work chose to study the roughening mechanism of current 193 nm PR, it is also highly relevant to future generation of nanoscale patterning, such as extreme ultraviolet (EUV) lithography and directed self-assembly (DSA), in which similar polymers are used.[6, 183] Lastly, during actual plasma etch processes where complex plasma chemistries are involved, additional roughening mechanisms may be in play and require further studies.

7.2 Concluding Remarks: Plasma-induced Lipid A Deactivation

The second part of this dissertation discusses the effects of VUV photons and radicals in lipid A deactivation under relevant oxygen and hydrogen plasma conditions. Using a surface-sensitive human whole blood-based assay, the present study shows that VUV photons, oxygen and deuterium radicals can cause deactivation of lipid A film through different mechanisms.

Similar to previous 193 nm PR studies, VUV photons are able to induce bulk modification of lipid A film up to the penetration depth of photons, ~200 nm. VUV photons primarily cleave ester linkages and lead to desorption of aliphatic chains. Loss of phosphate groups and glucosamine backbone is also observed. It suggests that damage of ester linkages and removal of pendant groups are the main VUV-induced photolysis mechanisms for ester-containing materials.

In contrast, radicals react at the lipid A film surface, form volatile products, and lead to slow chemical etching. The etch yield of radicals is one order of magnitude lower than that caused by VUV-induced photolysis. In spite of its low etch yield, radical exposure strongly modifies lipid A film surface. This is supported by secondary ion mass spectrometry, showing that the phosphate and fatty acid groups are greatly reduced compared to unprocessed and VUV-processed samples. This finding stresses the importance of radicals in lipid A deactivation

resulting from oxygen and hydrogen-containing plasmas, which was neglected in previous literature.[38, 75]

Besides VUV and radicals, surfaces immersed in low-pressure plasmas also receive bombardment of ions bearing plasma potential, about 15 eV, in the absence of external bias. The role of low energy ions and their synergy with photons and radicals have to be further established. The current endotoxic activity assay is limited to characterizing the surface of the film due to low solubility of lipid A in human whole blood. Furthermore, IL-1β secretion is not specific to the transmembrane Toll-like receptor 4 (TLR-4) pathway. For example, NALP3 inflammasome, one of the intracellular NOD-like receptors (NLRs), can also induce IL-1β secretion upon activation.[160, 184, 185] NALP3 can be activated by a wide variety of stimuli, including viral DNAs, bacterial toxins, and nonmicrobial “danger” or “damage” signals, such as monosodium urate crystals (MSU), calcium pyrophosphate dihydrate, aluminum salts, and reactive oxygen species (ROS), to name a few. It is proposed that ROS is a common NALP3 activator, which are either directly sensed by NALP3 or indirectly sensed through cytoplasmic proteins that modulate the inflammasome activity.[184] It is thus reasonable to postulate that fragments or reaction products of lipid A generated upon plasma species exposure might stimulate NALP3 pathway and increase overall IL-1β secretion. An increased IL-1β level has been observed with short term VUV exposure (Figure 6.6b) and preliminary results from indirect air dielectric-barrier discharge (DBD) treatment of lipid A. One has to pay extra attention in data interpretation because not only the interplay of immune response/signaling is delicate but also immunology is an actively evolving field. More sophisticated analytical assays are required to elaborate on the involved molecular/cellular pathways and the generated reaction products.

In summary, this work contributes to the fundamental understanding of plasma interaction with biomolecules. Through different mechanisms, VUV photons and radicals are shown to cause structural change of lipid A and thus alter its biological functions. The principle of this study is also relevant to the broader scope of plasma applications on biological targets, including treatment for skin diseases, cancers, and chronic wounds.[43-49]

Appendix A

NTI Low Energy Ion Gun Test

During low temperature plasma processes, positive ions are usually among the species reaching the exposed surface. In a low-pressure plasma, under conditions in which the sheaths are collisionless or nearly so, the ions impacting surfaces are accelerated to the plasma potential, ~15 eV, even in the absence of any external bias to the surface. Although it might be expected that ion kinetic energy impacting surfaces exposed to atmospheric pressure plasmas is sufficiently low to not be of importance, recent results suggest this may not be correct. In a recent publication modeling atmospheric pressure plasma-surface interactions, ions up to 60 eV were predicted to be delivered to the liquid interface of a wet wound by a direct air dielectric-barrier discharge (DBD).[186] This surprisingly high ion kinetic energy at surfaces exposed to atmospheric pressure plasmas suggests that ion energy effects cannot be neglected at atmospheric pressure. It is thus of potential practical interest to study low energy ion effect and ion synergies with other species to better understand plasma interaction with biological targets.

The Kaufman-type ion source used in previous photoresist study is not capable of delivering ions to surfaces with kinetic energy below 100 eV. Thus, a low energy ion source (Model 1402, Nonsequitur Technologies, Bend, OR, USA) was installed to test its capability. The ion gun was mounted on flange 6 and the ion current at the sample position was measured with a home-built Faraday cup (aperture size ~19.6×10^{-4} cm^2) mounted on flange 10 (Figure 2.1). The gun had a working distance ~3.2 cm to the sample surface. Ar gas was fed into the ion source region by a leak valve. A typical gas pressure of 30 mTorr was maintained in the source region. Electrons emitted from the energized filament generate Ar ions by electron impact ionization. The emission voltage was preset by the manufacturer to 100 V. Ions were extracted from the source region by a negatively biased extraction electrode. These ions were focused onto a beam shaping/differential focus aperture by the condenser lens. The focus lens served as the final step to deliver the ion beam onto the sample. The beam energy, extractor voltage, condenser voltage, and focus voltage could be independently controlled. For low energy ion beam applications, the focus lens was operated in an acceleration mode (negative voltage). A deflection octupole could also be used to raster the ion beam. A 100 $L\cdot s^{-1}$ turbo pump (TV 141 Navigator, Varian, Inc., now Agilent Technologies, Santa Clara, CA, USA) was used to differentially pump the condenser section.

Table A.1 Ion gun settings and performance.

Beam Energy (eV)	Ion chamber pressure (mTorr)	Extractor (V)	Condenser (V)	Focus (V)	Measured current at the sample position (nA)	Ion flux (ions·cm^{-2}·s^{-1})	Measured etch yield (Au·ion^{-1})
300	30	1100	110	-390	14.2	4.5×10^{13}	1.38
200	30	1100	110	-360	13.4	4.3×10^{13}	0.88
150	30	1100	92	-300	10.2	3.2×10^{13}	0.73
100	30	1100	97	-200	5.6	1.8×10^{13}	0.26
75	30	1100	97	-250	6.3	2.0×10^{13}	0.12
60	20/30	1100/1100	97/97	-200/-200	1.7/3.1	5.6×10^{12}/1.0×10^{13}	0.14/0.22
50	20/30	1100/1100	90/90	-200/-200	0.8/1.7	2.5×10^{12}/5.5×10^{12}	0.17/0.26

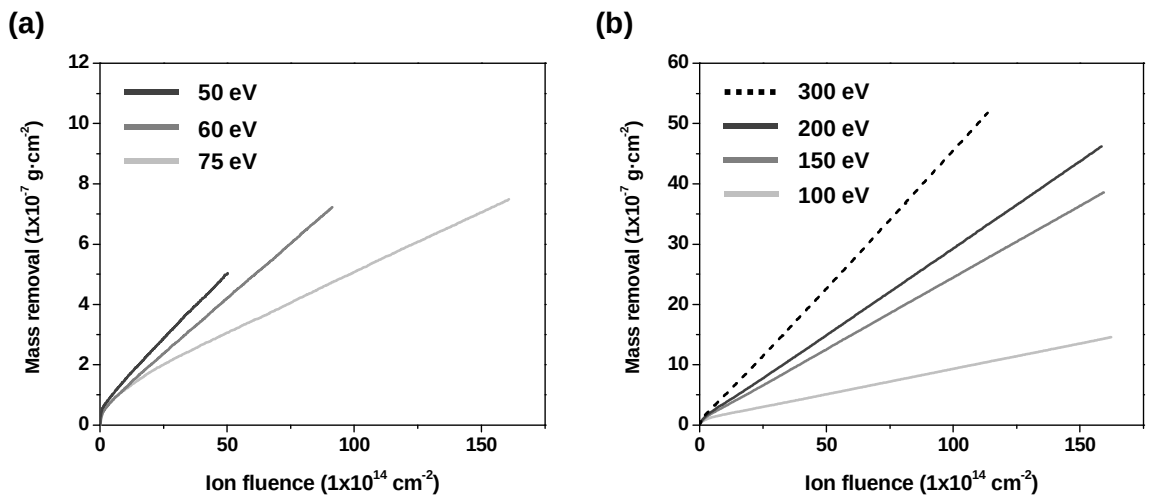

Figure A.1 QCM measurements of gold sputtering under Ar ion bombardment with different ion energies (a) 50, 60, and 75 eV (b) 100, 150, 200, and 300 eV. The pressure in the ion chamber was 30 mTorr.

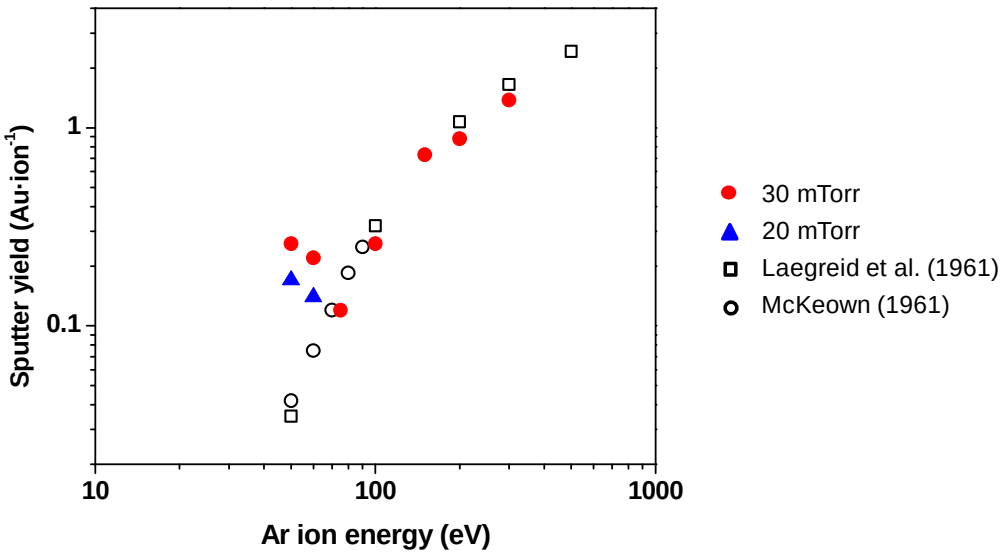

Figure A.2 Measured sputtering yields at various ion beam energies.[187, 188]

The tests were conducted with pristine quartz crystal microbalance (QCM) sensors (gold electrode) to measure the ion sputtering yield of gold. The optimized operation parameters, measured ion beam current and etch yield for each condition are summarized in Table A.1. The in situ QCM data are shown in Figure A.1. The measured sputtering yields are plotted with available literature values and shown in Figure A.2.[187-189] The measurements with and without beam raster are fairly similar, suggesting that the ion beam spot size was larger than the QCM sensor area and the ion current was fairly uniform.

Compared to the Kaufman-type ion source which can deliver an ion flux of ~2.8×10^{14} ions·cm^{-2}·s^{-1} (±10%) at the sample position, the ion flux from the NTI gun is much lower. At a 300 eV beam energy, the measured ion flux was ~4.5×10^{13} ions·cm^{-2}·s^{-1}. The measured ion current decreases with decreasing beam energy, possibly due to the space charge repulsion in the beam. At 50 eV ion beam energy, the ion flux was lower than 1×10^{13} ions·cm^{-2}·s^{-1}. Such a low ion current raises the issue that an impractically prolonged exposure might be required to match the total ion fluence with that in a plasma exposure. This may limit the value of the device.

The other issue is the deviation of apparent sputtering yields from literature values. As shown in Figure A.2, the measured sputtering yields agree with literature values well when the ion energy is higher than about 75 eV. However, for 50 and 60 eV ions, the apparent measured sputtering yields are much higher than literature values. One possible reason for this observation is charge exchange between neutral Ar atoms and Ar ions in the condenser section (differential pumping region) of the gun. Charge exchange generates fast neutral atoms in the beam. The resulting fast neutrals would have the same speed and sputtering yield as Ar ions but would not be measured in the Faraday cup. The QCM measures the overall mass removal while the Faraday cup only measures the ion current. Thus, a calculated apparent sputtering yield based on measured ion current would be significantly higher if the mass removal is caused by a mixed beam of ions and fast neutrals. Measurements conducted with a lower source region pressure, 20 mTorr, shows that the calculated apparent sputtering yield decreases compared to the 30 mTorr cases for 50 and 60 eV ions. A lower pressure implies fewer charge exchange collisions. This result therefore suggests that charge exchange is very likely the main mechanism of apparent sputtering yield deviation for low energy ions (< 60 eV). Currently, a new design of differential pumping is tested by NTI.

In summary, the tested ion gun is fully functional with ion energies higher than 75 eV. For ion energy below about 60 eV, which is mostly relevant to atmospheric pressure plasma applications on biological targets, the gun produces a beam of mixed ions and fast neutrals. Assuming the fast neutrals and ions have the same sputtering behavior, studies can still be conducted with NTI ion gun. One has to be mindful of total ion fluence/exposure time in order to directly compare results obtained from plasma exposures.

Appendix B

Lipid A Deactivation by Indirect Air Dielectric Barrier Discharge and UV/ozone cleaner

An atmospheric pressure, indirect air dielectric barrier discharge (DBD), also called surface micro-discharge (SMD), has been used in the Graves lab to study gas phase and liquid phase (when present) chemistry and in some cases, the resulting surface and aqueous antimicrobial effects.[190-193] It was found that when the input power was lower than ~0.1 $W \cdot cm^{-2}$, the gas phase ozone density increased monotonically to a concentration over 1000 ppm in a confined volume. Besides ozone, the presence of various other species, including N_2O and N_2O_5, were also predicted by simulation and characterized by transmission Fourier transform infrared (FTIR) spectroscopy. In contrast, when the input power was higher than ~0.1 $W \cdot cm^{-2}$, the ozone density started to decrease after a few tens of seconds. This was provisionally attributed to ozone quenching reactions with nitrogen oxides that were created by vibrationally excited nitrogen molecules reacting with O atoms at a higher power density. Under these conditions, the density of NO_2 increased as well as HNO_3.[193] In other words, the low-power mode is ozone-rich and the high-power mode is NO_x rich.

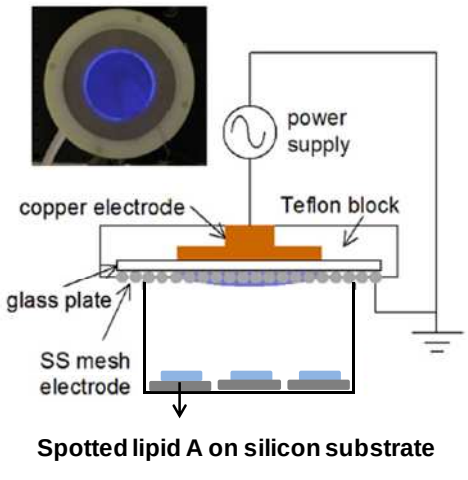

Figure B.1 Schematic of the indirect air DBD device. Adapted from reference [190].

Preliminary experiments were carried out to study lipid A deactivation by indirect air DBD in a confined reactor. The schematic of the system setup is shown in Figure B.1. More details of the device can be found in references [190], [191], and [193]. The distance between samples and the stainless steel mesh was about 40 mm. Two sets of DBD conditions were chosen: low-power mode (0.05 $W \cdot cm^{-2}$) and high-power mode (0.25 $W \cdot cm^{-2}$). Samples were also processed with a commercial UV/ozone cleaning system (UVOCS®, Lansdale, PA, USA) operated under ambient condition. The ozone was generated by a low-pressure quartz mercury vapor lamp in the UV/ozone cleaner. Processed samples (0.2 $mg \cdot ml^{-1}$, 10 μl) were then characterized by ex situ FTIR and human whole blood tests.

Figure B.2 shows the FTIR spectra (CH_2/CH_3 region) of samples processed with DBD in both low-power and high-power mode along with samples treated by the UV/ozone cleaner. While both DBD modes result in minimal change of processed samples, the UV/ozone cleaner shows a high level of mass removal.

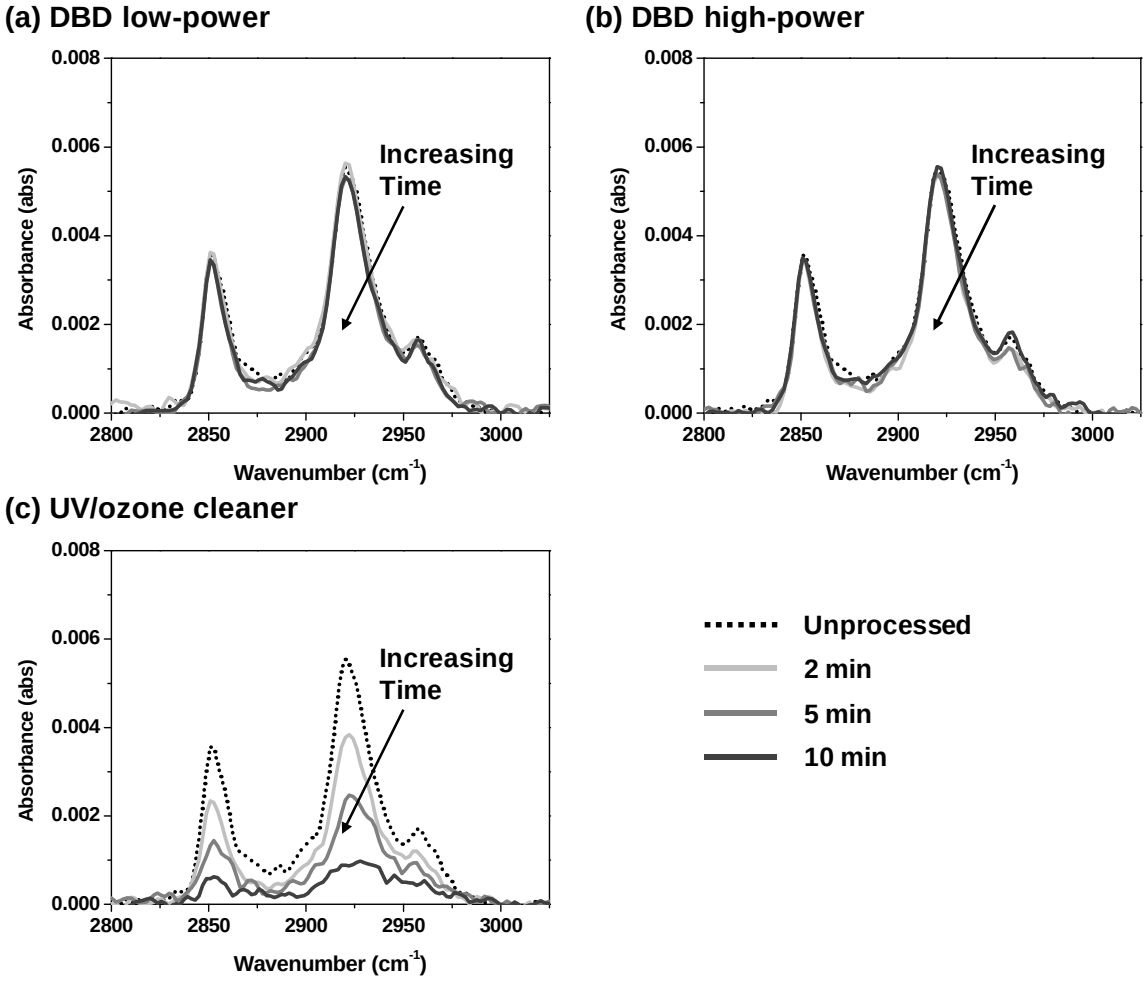

Figure B.2 Transmission FTIR spectra of lipid A CH_2/CH_3 bonds (2800-3025cm^{-1}) after various exposure protocols: (a) DBD low-power, (b) DBD high-power (c) UV/ozone cleaner. Each condition is an average of three independent measurements.

Figure B.3 shows the endotoxic activity of processed lipid A samples, which was monitored by measuring the secreted IL-1β in human whole blood from 1 healthy donor. For most conditions, the suppression of IL-1β is not observed. The results obtained from samples processed with the UV/ozone cleaner are especially surprising. The IL-1β secretion change with different exposure times does not correlate with the observed dramatic mass reductions observed with FTIR in Figure B.2.

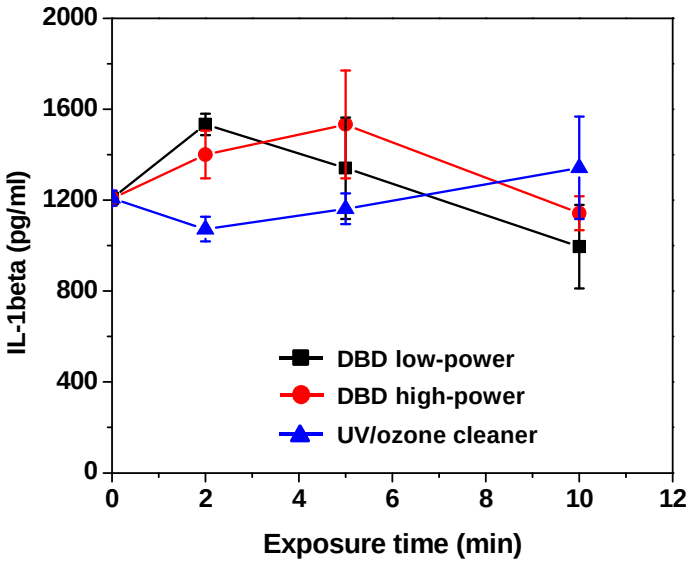

Figure B.3 Endotoxic activity monitored by secreted IL-1β in human whole blood assay. Measurements were conducted with blood from 1 healthy donor. The error bar for each data point stands for the standard deviation from 3 independent samples.

We note that the experimental conditions here (e.g. the operation pressure, the reactive species involved, the flux of reactive species) are very different from the low pressure studies reported in Chapter 6. While these preliminary results suggest that indirect DBD may not be a promising option for surface deactivation of lipid A, the UV/ozone cleaner results are surprising and counter-intuitive. The low-pressure plasma/beam results suggest that removal and alteration of lipid A will generally reduce the immune response, but the UV/ozone exposure removes a significant fraction of the film without altering the apparent endotoxic activity of the remaining film. As discussed in Chapter 6 and 7, the immune response is complex and not fully understood. It consists of various coupled, intertwined pathways. One possibility is that simple mass removal of lipid A may not be sufficient to reduce its endotoxic activity because the remaining residues or byproducts activate other pathways, and thus the overall inflammation response is not mitigated. This also highlights the challenge of deactivating virulent biomolecules in a clinical setting. Further studies on molecular/cellular level mechanisms are required in order to further pursuit atmospheric pressure plasma applications on biological targets.

Appendix C

Anti-inflammatory Effects of Indirect Air Dielectric Barrier Discharge-treated Water

Some published studies have shown that oxidized low-density lipoproteins (OxLDL) and "ozonized" amino acids present anti-inflammatory effects that suppress generation of cytokines from cells.[194, 195] Huth et al. prepared ozonized media with gaseous ozone generated in an ozone generator. Upon stimulation by tumor necrosis factor (TNF), cells pre-incubated with ozonized media showed a suppressed activation of transcription factor NF-κB and secretion of Interleukin-1β (IL-1β). The authors showed that ozonized amino acids, such as cysteine and tryptophan, are important components responsible for the anti-inflammatory effects.[195]

When operated at low power (~0.1 $W \cdot cm^{-2}$), indirect air dielectric barrier discharge (DBD) can be used to generate mainly ozone. Aqueous solutions treated by DBD operated at low power can result in high concentration of aqueous ozone.[193] It is suspected that DBD-treated water may lead to a similar anti-inflammatory effect as reported by Huth et al.[195]

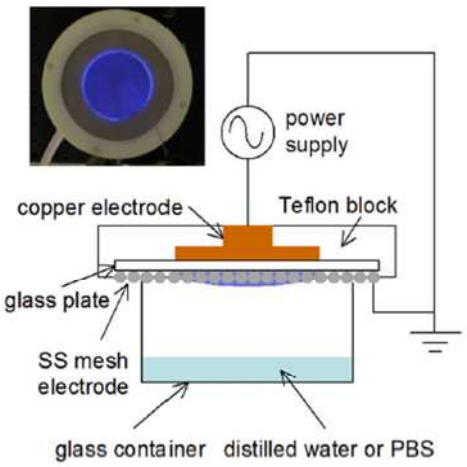

Figure C.1 Schematic of the indirect air DBD device.[190]

Figure C.1 shows the schematic of the setup. 5 ml of phosphate-buffered saline solution (PBS, catalog number: 10010, Life Technologies, Grand Island, NY, USA) or RPMI medium 1640 (catalog number: 21870, Life Technologies) was placed in a small petri dish and treated with DBD for 10 min. The solution was mixed with fresh human whole blood shortly after generation. The DBD operation power was fixed at 0.05 $W \cdot cm^{-2}$. The gap between the liquid surface and the stainless steel mesh was about 5 mm. The protocol of human whole blood test is shown in Figure C.2. 500 µl of fresh human whole blood was pre-incubated with 500 µl DBD-treated solution for 45 min. 5 µl of lipopolysaccharide (LPS) solution (1 $\mu g \cdot ml^{-1}$) was then used to stimulate leukocytes in whole blood. After another 22-h incubation, the supernatants were collected after centrifugation for 10 min at 400×g and stored at -20 °C until IL-1β contents were determined by a commercial enzyme-linked immunosorbent assay (ELISA) from Life Technologies.

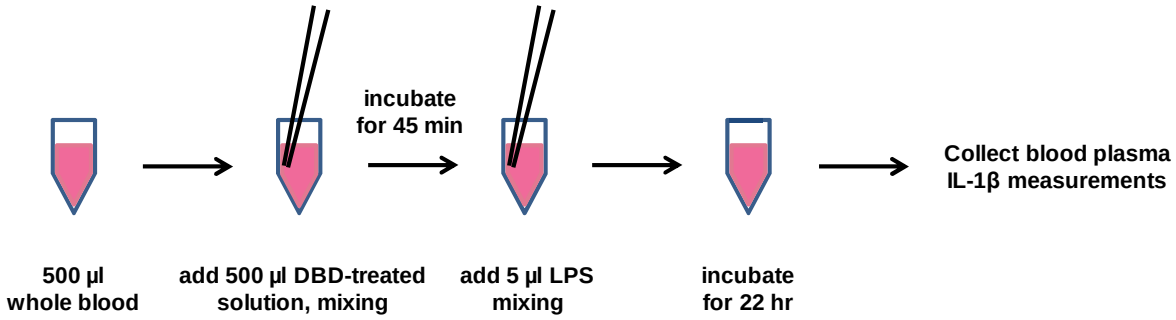

Figure C.2 The protocol of air DBD-treated solution tests.

Table C.1 Experimental conditions used in this study. Four samples were prepared for each condition. Three were for human whole blood tests and one was for cell viability determination by trypan blue exclusion.

Sample condition	Liquid Medium	DBD-treated water (500 µl)	LPS (5 µl, 1 $\mu g \cdot ml^{-1}$)
1	PBS	-	-
2	PBS	-	+
3	PBS	+	-
4	PBS	+	+
5	RPMI	-	-
6	RPMI	-	+
7	RPMI	+	-
8	RPMI	+	+

Experimental conditions are tabulated in Table C.1. Figure C.3 shows the IL-1β expression resulting from various treatments. Blood cell viability was monitored by trypan blue exclusion with a hemacytometer. No obvious cell death was observed after incubation.

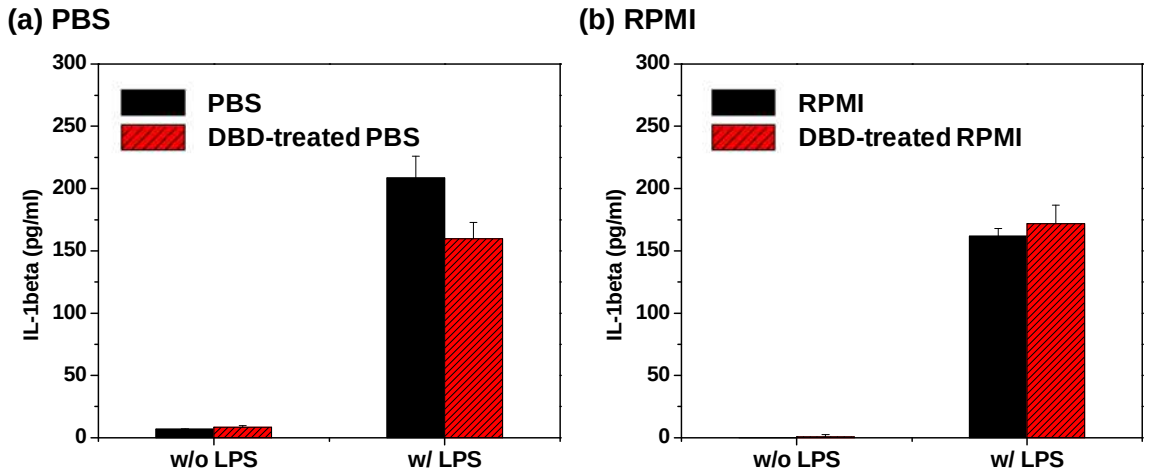

Figure C.3 Endotoxic activity monitored by secreted IL-1β in human whole blood assay. The liquid media were (a) PBS and (b) RPMI. Measurements were conducted with blood from 1 healthy donor. The error bar for each condition stands for the standard deviation from 3 independent samples.

Pristine PBS and RPMI without LPS do not stimulate IL-1β secretion. Without stimuli LPS, DBD-treated PBS and RPMI also show minimal inflammatory effects. On the other hand, the presence of LPS induces IL-1β expression through the Toll-like receptor 4 (TLR-4) pathway. For blood pre-incubated with DBD-treated PBS, the IL-1β concentration is suppressed to about 75% of that pre-incubated with untreated PBS. The result can be attributed to aqueous ozone oxidizing amino acids in blood serum. These modified amino acid molecules then interact with cellular signaling pathways and inhibit the secretion of IL-1β.[195] On the other hand, DBD-treated RPMI shows no clear anti-inflammatory effect. We observed that the color of RPMI faded after DBD treatment. It is suspected that aqueous ozone is consumed by reacting with phenol red (pH indicator in RPMI) and thus DBD-treated RPMI has no effect in IL-1β generation. Future experiments should verify this speculation by using RPMI without phenol red.

While disinfection effects of plasma or DBD-treated solutions have been demonstrated previously, the possible therapeutic effects of discharge-activated water suggest a new direction for exciting applications. However, these results are preliminary and require further studies. New assays have to be applied to identify the detailed inhibition mechanisms and anti-inflammatory products generated by aqueous ozone or other discharge-generated species. In addition, more recent work in the laboratory has demonstrated the importance of mass transfer (i.e. gas-liquid mixing) to ensure proper transfer of gas phase ozone species into the liquid.[193] One has to be mindful of experimental procedures to ensure the consistency and reproducibility of results.

References

[1] *Principles of Plasma Discharges and Materials Processing*, 2 ed., M. A. Lieberman, A. J. Lichtenberg, Wiley-InterScience, **2005**.

[2] G. E. Moore, *Electronics* **1965**, *38*, 114.

[3] C. Auth, C. Allen, A. Blattner, D. Bergstrom, M. Brazier, M. Bost, M. Buehler, V. Chikarmane, T. Ghani, T. Glassman, R. Grover, W. Han, D. Hanken, M. Hattendorf, P. Hentges, R. Heussner, J. Hicks, D. Ingerly, P. Jain, S. Jaloviar, R. James, D. Jones, J. Jopling, S. Joshi, C. Kenyon, H. Liu, R. McFadden, B. McIntyre, J. Neirynck, C. Parker, L. Pipes, I. Post, S. Pradhan, M. Prince, S. Ramey, T. Reynolds, J. Roesler, J. Sandford, J. Seiple, P. Smith, C. Thomas, D. Towner, T. Troeger, C. Weber, P. Yashar, K. Zawadzki, K. Mistry, in 2012 IEEE Symposium on VLSI Technology, Honolulu, HI, 2012, p. 131.

[4] *Optical Lithography : Here is Why*, B. J. Lin, SPIE, Bellingham, **2010**.

[5] R. H. French, H. V. Tran, "*Immersion Lithography: Photomask and Wafer-Level Materials*", in *Annual Review of Materials Research*, Annual Reviews, Palo Alto, **2009**, *39*, 93.

[6] S.-Y. Moon, J.-M. Kim, *J. Photochem. Photobiol. C: Photochem. Rev.* **2007**, *8*, 157.

[7] H. Ito, *Adv. Polym. Sci.* **2005**, *172*, 37.

[8] S. Takechi, M. Takahashi, A. Kotachi, K. Nozaki, E. Yano, I. Hanyu, *J. Photopolym. Sci. Tec.* **1996**, *9*, 475.

[9] H. Abe, M. Yoneda, N. Fujiwara, *Jpn. J. Appl. Phys.* **2008**, *47*, 1435.

[10] H. Namatsu, M. Nagase, T. Yamaguchi, K. Yamazaki, K. Kurihara, *J. Vac. Sci. Technol. B* **1998**, *16*, 3315.

[11] J. Kim, Y. S. Chae, W. S. Lee, J. W. Shon, C. J. Kang, W. S. Han, J. T. Moon, *J. Vac. Sci. Technol. B* **2003**, *21*, 790.

[12] D. L. Goldfarb, A. P. Mahorowala, G. M. Gallatin, K. E. Petrillo, K. Temple, M. Angelopoulos, S. Rasgon, H. H. Sawin, S. D. Allen, M. C. Lawson, R. W. Kwong, *J. Vac. Sci. Technol. B* **2004**, *22*, 647.

[13] N. Negishi, H. Takesue, M. Sumiya, T. Yoshida, Y. Momonoi, M. Izawa, *J. Vac. Sci. Technol. B* **2005**, *23*, 217.

[14] S. Engelmann, R. L. Bruce, T. Kwon, R. Phaneuf, G. S. Oehrlein, Y. C. Bae, C. Andes, D. Graves, D. Nest, E. A. Hudson, P. Lazzeri, E. Iacob, M. Anderle, *J. Vac. Sci. Technol. B* **2007**, *25*, 1353.
[15] S. Engelmann, R. L. Bruce, F. Weilnboeck, M. Sumiya, T. Kwon, R. Phaneuf, G. S. Oehrlein, C. Andes, D. Graves, D. Nest, E. A. Hudson, *J. Vac. Sci. Technol. B* **2009**, *27*, 1165.
[16] E. Pargon, M. Martin, J. Thiault, O. Joubert, J. Foucher, T. Lill, *J. Vac. Sci. Technol. B* **2008**, *26*, 1011.
[17] S.-D. Kim, H. Wada, J. C. S. Woo, *IEEE Trans. Semicond. Manuf.* **2004**, *17*, 192.
[18] *International Technology Roadmap for Semiconductors, 2011 Edition*.
[19] H. Gokan, S. Esho, Y. Ohnishi, *J. Electrochem. Soc.* **1983**, *130*, 143.
[20] R. M. Klevens, J. R. Edwards, C. L. Richards, T. C. Horan, R. P. Gaynes, D. A. Pollock, D. M. Cardo, *Public Health Rep.* **2007**, *122*, 160.
[21] "*Annual Epidemiological Report on Communicable Diseases in Europe 2008*", European Centre for Disease Prevention and Control, Stockholm, **2008**.
[22] A. M. Miniño, S. L. Murphy, J. Xu, K. D. Kochanek, *Natl. Vital Stat. Rep.* **2011**, *59*, 1.
[23] R. D. Scott, "*The direct medical costs of healthcare-associated infections in U.S. hospitals and the benefits of prevention*", Centers for Disease Control and Prevention, **2009**.
[24] W. A. Rutala, D. J. Weber, Healthcare Infection Control Practices Advisory Committee, "*Guideline for Disinfection and Sterilization in Healthcare Facilities, 2008*", **2008**.
[25] D. J. Weber, W. A. Rutala, M. B. Miller, K. Huslage, E. Sickbert-Bennett, *Am. J. Infect. Control* **2010**, *38*, S25.
[26] P. Corne, S. Godreuil, H. Jean-Pierre, O. Jonquet, J. Campos, E. Jumas-Bilak, S. Parer, H. Marchandin, *J. Hosp. Infect.* **2005**, *61*, 20.
[27] R. Bou, A. Aguilar, J. Perpiñán, P. Ramos, M. Peris, L. Lorente, A. Zúñiga, *J. Hosp. Infect.* **2006**, *64*, 129.
[28] A. M. Wendelboe, J. Baumbach, D. B. Blossom, P. Frank, A. Srinivasan, C. M. Sewell, *J. Urology* **2008**, *180*, 588.
[29] P. K. Tosh, M. Disbot, J. M. Duffy, M. L. Boom, G. Heseltine, A. Srinivasan, C. V. Gould, S. I. Berríos-Torres, *Infect. Control Hosp. Epidemiol.* **2011**, *32*, 1179.
[30] R. L. Baxter, H. C. Baxter, G. A. Campbell, K. Grant, A. Jones, P. Richardson, G. Whittaker, *J. Hosp. Infect.* **2006**, *63*, 439.
[31] H. Murdoch, D. Taylor, J. Dickinson, J. T. Walker, D. Perrett, N. D. H. Raven, J. M. Sutton, *J. Hosp. Infect.* **2006**, *63*, 432.
[32] I. P. Lipscomb, A. K. Sihota, C. W. Keevil, *J. Clin. Microbiol.* **2006**, *44*, 3728.
[33] M. J. Alfa, N. Olson, A. Al-Fadhaly, *J. Hosp. Infect.* **2010**, *74*, 168.
[34] J. Cohen, *Nature* **2002**, *420*, 885.
[35] *Endotoxins: Pyrogens, LAL Testing and Depyrogenation*, 3rd ed., K. L. Williams, Eds., Informa Healthcare USA, Inc., New York, **2007**.
[36] W. A. Rutala, D. J. Weber, *Infect. Control Hosp. Epidemiol.* **2010**, *31*, 107.
[37] M. Moisan, J. Barbeau, S. Moreau, J. Pelletier, M. Tabrizian, L. H. Yahia, *Int. J. Pharm.* **2001**, *226*, 1.
[38] A. von Keudell, P. Awakowicz, J. Benedikt, V. Raballand, A. Yanguas-Gil, J. Opretzka, C. Flötgen, R. Reuter, L. Byelykh, H. Halfmann, K. Stapelmann, B. Denis, J. Wunderlich,

P. Muranyi, F. Rossi, O. Kylián, N. Hasiwa, A. Ruiz, H. Rauscher, L. Sirghi, E. Comoy, C. Dehen, L. Challier, J. P. Deslys, *Plasma Process. Polym.* **2010**, *7*, 327.
[39] B. Elmoualij, O. Thellin, S. Gofflot, E. Heinen, P. Levif, J. Séguin, M. Moisan, A. Leduc, J. Barbeau, W. Zorzi, *Plasma Process. Polym.* **2012**, *9*, 612.
[40] S. Lerouge, M. R. Wertheimer, R. Marchand, M. Tabrizian, L. H. Yahia, *J. Biomed. Mater. Res.* **2000**, *51*, 128.
[41] M. C. Krebs, P. Bécasse, D. Verjat, J. C. Darbord, *Int. J. Pharm.* **1998**, *160*, 75.
[42] M. Laroussi, *Plasma Process. Polym.* **2005**, *2*, 391.
[43] M. Laroussi, *IEEE Trans. Plasma Sci.* **1996**, *24*, 1188.
[44] G. Fridman, A. Shereshevsky, M. M. Jost, A. D. Brooks, A. Fridman, A. Gutsol, V. Vasilets, G. Friedman, *Plasma Chem. Plasma Process.* **2007**, *27*, 163.
[45] G. Fridman, G. Friedman, A. Gutsol, A. B. Shekhter, V. N. Vasilets, A. Fridman, *Plasma Process. Polym.* **2008**, *5*, 503.
[46] M. G. Kong, G. Kroesen, G. Morfill, T. Nosenko, T. Shimizu, J. van Dijk, J. L. Zimmermann, *New J. Phys.* **2009**, *11*, 115012.
[47] G. Isbary, G. Morfill, H. U. Schmidt, M. Georgi, K. Ramrath, J. Heinlin, S. Karrer, M. Landthaler, T. Shimizu, B. Steffes, W. Bunk, R. Monetti, J. L. Zimmermann, R. Pompl, W. Stolz, *Brit. J. Dermatol.* **2010**, *163*, 78.
[48] J. Heinlin, G. Isbary, W. Stolz, G. Morfill, M. Landthaler, T. Shimizu, B. Steffes, T. Nosenko, J. L. Zimmermann, S. Karrer, *J. Eur. Acad. Dermatol. Venereol.* **2011**, *25*, 1.
[49] M. Vandamme, E. Robert, S. Lerondel, V. Sarron, D. Ries, S. Dozias, J. Sobilo, D. Gosset, C. Kieda, B. Legrain, J.-M. Pouvesle, A. Le Pape, *Int. J. Cancer* **2012**, *130*, 2185.
[50] F. Weilnboeck, R. L. Bruce, S. Engelmann, G. S. Oehrlein, D. Nest, T.-Y. Chung, D. Graves, M. Li, D. Wang, C. Andes, E. A. Hudson, *J. Vac. Sci. Technol. B* **2010**, *28*, 993.
[51] F. Weilnboeck, N. Kumar, G. S. Oehrlein, T.-Y. Chung, D. Graves, M. Li, E. A. Hudson, E. C. Benck, *J. Vac. Sci. Technol. B* **2012**, *30*, 031807.
[52] H. Shi, H. Huang, J. Bao, J. Liu, P. S. Ho, Y. Zhou, J. T. Pender, M. D. Armacost, D. Kyser, *J. Vac. Sci. Technol. B* **2012**, *30*, 011206.
[53] J. W. Coburn, H. F. Winters, *J. Appl. Phys.* **1979**, *50*, 3189.
[54] G. P. Kota, J. W. Coburn, D. B. Graves, *J. Vac. Sci. Technol. A* **1998**, *16*, 2215.
[55] F. Greer, J. W. Coburn, D. B. Graves, *J. Vac. Sci. Technol. A* **2000**, *18*, 2288.
[56] J. P. Chang, H. H. Sawin, *J. Vac. Sci. Technol. B* **2001**, *19*, 1319.
[57] Y. Kimura, PhD Thesis, University of California, Berkeley, **2005**.
[58] D. Nest, PhD Thesis, University of California, Berkeley, **2009**.
[59] M. J. Titus, PhD Thesis, University of California, Berkeley, **2010**.
[60] H. Singh, J. W. Coburn, D. B. Graves, *J. Vac. Sci. Technol. A* **2000**, *18*, 299.
[61] D. C. Frost, C. A. McDowell, *J. Am. Chem. Soc.* **1958**, *80*, 6183.
[62] P. T. Smith, *Physical Review* **1930**, *36*, 1293.
[63] "Ground Levels and Ionization Energies for the Neutral Atoms", NIST Standard Reference Data.
[64] D. Rapp, P. Englander-Golden, *J. Chem. Phys.* **1965**, *43*, 1464.
[65] M. B. Shah, D. S. Elliott, H. B. Gilbody, *J. Phys. B: At. Mol. Phys.* **1987**, *20*, 3501.
[66] W. R. Thompson, M. B. Shah, H. B. Gilbody, *J. Phys. B: At. Mol. Opt. Phys.* **1995**, *28*, 1321.
[67] C. Erridge, E. Bennett-Guerrero, I. R. Poxton, *Microbes Infect.* **2002**, *4*, 837.

[68] E. T. Rietschel, H.-W. Wollenweber, R. Russa, H. Brade, U. Zähringer, *Rev. Infect. Dis.* **1984**, *6*, 432.
[69] *Fundamentals of Fourier Transform Infrared Spectroscopy*, 2nd ed., B. C. Smith, CRC Press, **2011**.
[70] NIST Mass Spec Data Center, "Mass Spectra" in NIST Chemistry WebBook, NIST Standard Reference Database Number 69, Eds. P.J. Linstrom and W.G. Mallard, National Institute of Standards and Technology, Gaithersburg MD, 20899, http://webbook.nist.gov, (retrieved 2012).
[71] *Mass Spectrometry*, 2nd ed., J. H. Gross, Springer, **2010**.
[72] O. Kylián, M. Hasiwa, F. Rossi, *IEEE Trans. Plasma Sci.* **2006**, *34*, 2606.
[73] M. Hasiwa, K. Kullmann, S. von Aulock, C. Klein, T. Hartung, *Biomaterials* **2007**, *28*, 1367.
[74] O. Kylián, M. Hasiwa, D. Gilliland, F. Rossi, *Plasma Process. Polym.* **2008**, *5*, 26.
[75] F. Rossi, O. Kylián, H. Rauscher, M. Hasiwa, D. Gilliland, *New J. Phys.* **2009**, *11*, 115017.
[76] S. Hoffmann, A. Peterbauer, S. Schindler, S. Fennrich, S. Poole, Y. Mistry, T. Montag-Lessing, I. Spreitzer, B. Löschner, M. van Aalderen, R. Bos, M. Gommer, R. Nibbeling, G. Werner-Felmayer, P. Loitzl, T. Jungi, M. Brcic, P. Brügger, E. Frey, G. Bowe, J. Casado, S. Coecke, J. de Lange, B. Mogster, L. M. Naess, I. S. Aaberge, A. Wendel, T. Hartung, *J. Immunol. Methods* **2005**, *298*, 161.
[77] *Janeway's Immnobiology*, K. Murphy, P. Travers, M. Walport, Garland Science, Taylor & Francis Group, LLC, New York and London, **2008**.
[78] M. M. Wurfel, W. Y. Park, F. Radella, J. Ruzinski, A. Sandstrom, J. Strout, R. E. Bumgarner, T. R. Martin, *J. Immunol.* **2005**, *175*, 2570.
[79] C. W. Thurm, J. F. Halsey, "*Measurement of Cytokine Production Using Whole Blood*", in *Current Protocols in Immunology*, John Wiley & Sons, Inc., **2005**, 7.18B.1.
[80] D. Nest, D. B. Graves, S. Engelmann, R. L. Bruce, F. Weilnboeck, G. S. Oehrlein, C. Andes, E. A. Hudson, *Appl. Phys. Lett.* **2008**, *92*, 153113.
[81] D. Nest, T.-Y. Chung, D. B. Graves, S. Engelmann, R. L. Bruce, F. Weilnboeck, G. S. Oehrlein, D. Wang, C. Andes, E. A. Hudson, *Plasma Process. Polym.* **2009**, *6*, 649.
[82] M. J. Titus, D. G. Nest, T.-Y. Chung, D. B. Graves, *J. Phys. D: Appl. Phys.* **2009**, *42*, 245205.
[83] G. S. Oehrlein, R. J. Phaneuf, D. B. Graves, *J. Vac. Sci. Technol. B* **2011**, *29*, 010801.
[84] T. Yunogami, T. Mizutani, K. Suzuki, S. Nishimatsu, *Jpn. J. Appl. Phys.* **1989**, *28*, 2172.
[85] M. R. Wertheimer, A. C. Fozza, A. Holländer, *Nucl. Instrum. Methods Phys. Res. B* **1999**, *151*, 65.
[86] Y. Ishikawa, Y. Katoh, M. Okigawa, S. Samukawa, *J. Vac. Sci. Technol. A* **2005**, *23*, 1509.
[87] M. J. Titus, D. Nest, D. B. Graves, *Appl. Phys. Lett.* **2009**, *94*, 171501.
[88] F.-E. Truica-Marasescu, PhD Thesis, Université de Montréal, **2005**.
[89] A. P. Mahorowala, K.-J. Chen, R. Sooriyakumaran, A. Clancy, D. Murthy, S. Rasgon, *Proc. SPIE* **2005**, *5753*, 380.
[90] H. Kawahira, N. N. Matsuzawa, E. Matsui, A. Ando, K. M. A. Salam, M. Yoshida, Y. Yamaguchi, K. Kugimiya, T. Tatsumi, H. Nakano, T. Iwai, M. Irie, *Proc. SPIE* **2006**, *6153*, 615319.

[91] M.-C. Kim, D. Shamiryan, Y. Jung, W. Boullart, C.-J. Kang, H.-K. Cho, *J. Vac. Sci. Technol. B* **2006**, *24*, 2645.
[92] E. Pargon, M. Martin, K. Menguelti, L. Azarnouche, J. Foucher, O. Joubert, *Appl. Phys. Lett.* **2009**, *94*, 103111.
[93] E. Pargon, K. Menguelti, M. Martin, A. Bazin, O. Chaix-Pluchery, C. Sourd, S. Derrough, T. Lill, O. Joubert, *J. Appl. Phys.* **2009**, *105*, 094902.
[94] J. J. Ritsko, L. J. Brillson, R. W. Bigelow, T. J. Fabish, *J. Chem. Phys.* **1978**, *69*, 3931.
[95] V. M. Bermudez, *J. Vac. Sci. Technol. B* **1999**, *17*, 2512.
[96] L. Sanche, *Nucl. Instrum. Methods Phys. Res. B* **2003**, *208*, 4.
[97] The Stopping and Range of Ions in Matter http://www.srim.org/.
[98] W. En, N. W. Cheung, *IEEE Trans. Plasma Sci.* **1996**, *24*, 1184.
[99] P. Martens, S. Yamamoto, K. Edamatsu, Y. Uetani, L. Pain, R. Palla, M. Ross, W. Livesay, *Proc. SPIE* **2001**, *4345*, 138.
[100] M.-S. Kim, J.-W. Park, H.-J. Kim, B.-J. Jun, M.-G. Gil, B.-H. Kim, M. Ross, W. Livesay, *Proc. SPIE* **2001**, *4345*, 737.
[101] M. Padmanaban, E. Alemy, R. R. Dammel, W.-K. Kim, T. Kudo, S.-H. Lee, D. McKenzie, A. Orsi, D. Rahman, W.-L. Chen, R. M. Sadjadi, W. Livesay, M. Ross, *Proc. SPIE* **2002**, *4690*, 606.
[102] B. J. Bachman, M. J. Vasile, *J. Vac. Sci. Technol. A* **1989**, *7*, 2709.
[103] P. Gröning, O. M. Küttel, M. Collaud-Coen, G. Dietler, L. Schlapbach, *Appl. Surf. Sci.* **1995**, *89*, 83.
[104] B. Pignataro, M. E. Fragalà, O. Puglisi, *Nucl. Instrum. Methods Phys. Res. B* **1997**, *131*, 141.
[105] J. Zekonyte, J. Erichsen, V. Zaporojtchenko, F. Faupel, *Surf. Sci.* **2003**, *532*, 1040.
[106] Y. Koval, *J. Vac. Sci. Technol. B* **2004**, *22*, 843.
[107] J. Zekonyte, V. Zaporojtchenko, F. Faupel, *Nucl. Instrum. Methods Phys. Res. B* **2005**, *236*, 241.
[108] R. L. Bruce, S. Engelmann, T. Lin, T. Kwon, R. J. Phaneuf, G. S. Oehrlein, B. K. Long, C. G. Willson, J. J. Végh, D. Nest, D. B. Graves, A. Alizadeh, *J. Vac. Sci. Technol. B* **2009**, *27*, 1142.
[109] J. J. Végh, D. Nest, D. B. Graves, R. L. Bruce, S. Engelmann, T. Kwon, R. J. Phaneuf, G. S. Oehrlein, B. K. Long, C. G. Willson, *Appl. Phys. Lett.* **2007**, *91*, 233113.
[110] G. K. Choudhary, J. J. Végh, D. B. Graves, *J. Phys. D: Appl. Phys.* **2009**, *42*, 242001.
[111] D. R. McKenzie, D. Muller, B. A. Pailthorpe, *Phys. Rev. Lett.* **1991**, *67*, 773.
[112] M. Weiler, S. Sattel, T. Giessen, K. Jung, H. Ehrhardt, V. S. Veerasamy, J. Robertson, *Phys. Rev. B* **1996**, *53*, 1594.
[113] J. Schwan, S. Ulrich, H. Roth, H. Ehrhardt, S. R. P. Silva, J. Robertson, R. Samlenski, R. Brenn, *J. Appl. Phys.* **1996**, *79*, 1416.
[114] T.-C. Lin, R. L. Bruce, G. S. Oehrlein, R. J. Phaneuf, H.-C. Kan, *Appl. Phys. Lett.* **2012**, *100*, 233113.
[115] N. Ueno, T. Mitsuhata, K. Sugita, K. Tanaka, *ACS Sym. Ser.* **1989**, *412*, 424.
[116] V. E. Skurat, Y. I. Dorofeev, *Angew. Makromol. Chem.* **1994**, *216*, 205.
[117] E. Pargon, L. Azarnouche, M. Fouchier, K. Menguelti, R. Tiron, C. Sourd, O. Joubert, *Plasma Process. Polym.* **2011**, *8*, 1184.
[118] F.-E. Truica-Marasescu, M. R. Wertheimer, *Macromol. Chem. Phys.* **2005**, *206*, 744.
[119] M. J. Titus, D. G. Nest, D. B. Graves, *J. Phys. D: Appl. Phys.* **2009**, *42*, 152001.

[120] N. Bowden, S. Brittain, A. G. Evans, J. W. Hutchinson, G. M. Whitesides, *Nature* **1998**, *393*, 146.
[121] N. Bowden, W. T. S. Huck, K. E. Paul, G. M. Whitesides, *Appl. Phys. Lett.* **1999**, *75*, 2557.
[122] D. B. H. Chua, H. T. Ng, S. F. Y. Li, *Appl. Phys. Lett.* **2000**, *76*, 721.
[123] D.-Y. Khang, H. Jiang, Y. Huang, J. A. Rogers, *Science* **2006**, *311*, 208.
[124] H. Jiang, D.-Y. Khang, J. Song, Y. Sun, Y. Huang, J. A. Rogers, *Proc. Natl. Acad. Sci. U.S.A.* **2007**, *104*, 15607.
[125] P.-C. Lin, S. Yang, *Appl. Phys. Lett.* **2007**, *90*, 241903.
[126] P. J. Yoo, H. H. Lee, *Phys. Rev. Lett.* **2003**, *91*, 154502.
[127] J. R. Serrano, Q. Xu, D. G. Cahill, *J. Vac. Sci. Technol. A* **2006**, *24*, 324.
[128] R. Huang, *J. Mech. Phys. Solids* **2005**, *53*, 63.
[129] Z. Y. Huang, W. Hong, Z. Suo, *J. Mech. Phys. Solids* **2005**, *53*, 2101.
[130] R. Huang, S. H. Im, *Phys. Rev. E* **2006**, *74*, 026214.
[131] R. L. Bruce, F. Weilnboeck, T. Lin, R. J. Phaneuf, G. S. Oehrlein, B. K. Long, C. G. Willson, J. J. Végh, D. Nest, D. B. Graves, *J. Appl. Phys.* **2010**, *107*, 084310.
[132] M. A. McCord, T. H. Newman, *J. Vac. Sci. Technol. B* **1992**, *10*, 3083.
[133] H. Hiraoka, *IBM J. Res. Dev.* **1977**, *21*, 121.
[134] M. Hatzakis, *J. Electrochem. Soc.* **1969**, *116*, 1033.
[135] A. C. F. Hoole, M. E. Welland, A. N. Broers, *Semicond. Sci. Technol.* **1997**, *12*, 1166.
[136] S. O. Cho, H. Y. Jun, *Nucl. Instrum. Methods Phys. Res. B* **2005**, *237*, 525.
[137] J.-K. Chen, F.-H. Ko, F.-C. Chang, *Adv. Funct. Mater.* **2005**, *15*, 1147.
[138] S. Eve, J. Mohr, *Procedia Engineering* **2009**, *1*, 237.
[139] M. Fukuhara, A. Sampei, *J. Polym. Sci. Pt. B: Polym. Phys.* **1995**, *33*, 1847.
[140] Y. Kaimoto, K. Nozaki, S. Takechi, N. Abe, *Proc. SPIE* **1992**, *1672*, 66.
[141] Y.-J. Choi, J.-W. Kim, J.-Y. Kim, Y.-G. Yim, J. Kim, J.-C. Jung, M.-J. Min, C. K. Bok, K.-S. Shin, *Proc. SPIE* **2003**, *5039*, 781.
[142] Y. C. Bae, G. G. Barclay, P. J. Bolton, R. J. Kavanagh, L. Bu, T. Kobayashi, T. Adams, N. Pugliano, J. W. Thackeray, *Proc. SPIE* **2003**, *5039*, 665.
[143] K. Fukushima, S. Tanaka, N. Matsumoto, H. Ohno, N. Kawano, H. Yamane, N. Hatakeyama, K. Ito, *Proc. SPIE* **2008**, *6923*, 692335.
[144] S. Engelmann, R. L. Bruce, F. Weilnboeck, G. S. Oehrlein, D. Nest, D. B. Graves, C. Andes, E. A. Hudson, *Plasma Process. Polym.* **2009**, *6*, 484.
[145] R. C. Fort, P. V. Schleyer, *Chem. Rev.* **1964**, *64*, 277.
[146] H. C. Straub, B. G. Lindsay, K. A. Smith, R. F. Stebbings, *J. Chem. Phys.* **1996**, *105*, 4015.
[147] H. C. Straub, P. Renault, B. G. Lindsay, K. A. Smith, R. F. Stebbings, *Phys. Rev. A* **1996**, *54*, 2146.
[148] K. Becker, Personal Commun. **2010**.
[149] M. Bobeldijk, W. J. van der Zande, P. G. Kistemaker, *Chem. Phys.* **1994**, *179*, 125.
[150] H. Deutsch, K. Becker, S. Matt, T. D. Märk, *Int. J. Mass Spectrom.* **2000**, *197*, 37.
[151] V. Nelea, V. N. Vasilets, V. E. Skurat, F.-E. Truica-Marasescu, M. R. Wertheimer, *Plasma Process. Polym.* **2010**, *7*, 431.
[152] M. Suto, X. Wang, L. C. Lee, *J. Phys. Chem.* **1988**, *92*, 3764.
[153] H.-C. Lu, H.-K. Chen, B.-M. Cheng, *Anal. Chem.* **2004**, *76*, 5965.

[154] M. Schwell, H.-W. Jochims, H. Baumgärtel, F. Dulieu, S. Leach, *Planet. Space Sci.* **2006**, *54*, 1073.
[155] M. Nobre, A. Fernandes, F. F. da Silva, R. Antunes, D. Almeida, V. Kokhan, S. V. Hoffmann, N. J. Mason, S. Eden, P. Limão-Vieira, *Phys. Chem. Chem. Phys.* **2008**, *10*, 550.
[156] I. Mokbel, K. Růžička, V. Majer, V. Růžička, M. Ribeiro, J. Jose, M. Zábranský, *Fluid Phase Equilibr.* **2000**, *169*, 191.
[157] C. C. Cypcar, P. Camelio, V. Lazzeri, L. J. Mathias, B. Waegell, *Macromolecules* **1996**, *29*, 8954.
[158] A. Matsumoto, S. Tanaka, T. Otsu, *Macromolecules* **1991**, *24*, 4017.
[159] M. P. Scott, M. Rahman, C. S. Brazel, *Eur. Polym. J.* **2003**, *39*, 1947.
[160] A. Weber, P. Wasiliew, M. Kracht, *Sci. Signal.* **2010**, *3*, cm2.
[161] T. A. Baker, X. Liu, C. M. Friend, *Phys. Chem. Chem. Phys.* **2011**, *13*, 34.
[162] M. A. Golub, T. Wydeven, *Polym. Degrad. Stabil.* **1988**, *22*, 325.
[163] W. Jacob, *Thin Solid Films* **1998**, *326*, 1.
[164] E. Vietzke, V. Philipps, *Fusion Technol.* **1989**, *15*, 108.
[165] A. Erradi, R. Clergereaux, F. Gaboriau, *J. Appl. Phys.* **2010**, *107*, 093305.
[166] A. von Keudell, M. Meier, C. Hopf, *Diam. Relat. Mater.* **2002**, *11*, 969.
[167] R. C. Seid, W. M. Bone, L. R. Phillips, *Anal. Biochem.* **1986**, *155*, 168.
[168] J. W. Jones, S. A. Shaffer, R. K. Ernst, D. R. Goodlett, F. Tureček, *Proc. Natl. Acad. Sci. U.S.A.* **2008**, *105*, 12742.
[169] H. Yuan, D. R. Killelea, S. Tepavcevic, S. I. Kelber, S. J. Sibener, *J. Phys. Chem. A* **2011**, *115*, 3736.
[170] T.-Y. Chung, D. B. Graves, F. Weilnboeck, R. L. Bruce, G. S. Oehrlein, M. Li, E. A. Hudson, *Plasma Process. Polym.* **2011**, *8*, 1068.
[171] J. M. Gingell, N. J. Mason, H. Zhao, I. C. Walker, M. R. F. Siggel, *Chem. Phys.* **1997**, *220*, 191.
[172] R. H. Hansen, J. V. Pascale, T. De Benedictis, P. M. Rentzepis, *J. Polym. Sci. Part A: Polym. Chem.* **1965**, *3*, 2205.
[173] F. D. Egitto, *Pure Appl. Chem.* **1990**, *62*, 1699.
[174] L. Lianos, D. Parrat, T. Q. Hoc, T. M. Duc, *J. Vac. Sci. Technol. A* **1994**, *12*, 2491.
[175] T. K. Minton, J. Zhang, D. J. Garton, J. W. Seale, *High Perform. Polym.* **2000**, *12*, 27.
[176] D. M. Buczala, A. L. Brunsvold, T. K. Minton, *J. Spacecr. Rockets* **2006**, *43*, 421.
[177] E. Vietzke, K. Flaskamp, V. Philipps, G. Esser, P. Wienhold, J. Winter, *J. Nucl. Mater.* **1987**, *145*, 443.
[178] E. Vietzke, V. Philipps, K. Flaskamp, P. Koidl, C. Wild, *Surf. Coat. Technol.* **1991**, *47*, 156.
[179] A. Horn, A. Schenk, J. Biener, B. Winter, C. Lutterloh, M. Wittmann, J. Küppers, *Chem. Phys. Lett.* **1994**, *231*, 193.
[180] T. Zecho, B. D. Brandner, J. Biener, J. Küppers, *J. Phys. Chem. B* **2001**, *105*, 6194.
[181] M. Schlüter, C. Hopf, T. Schwarz-Selinger, W. Jacob, *J. Nucl. Mater.* **2008**, *376*, 33.
[182] G. S. Oehrlein, T. Schwarz-Selinger, K. Schmid, M. Schlüter, W. Jacob, *J. Appl. Phys.* **2010**, *108*, 043307.
[183] J. Y. Cheng, D. P. Sanders, H. D. Truong, S. Harrer, A. Friz, S. Holmes, M. Colburn, W. D. Hinsberg, *ACS Nano* **2010**, *4*, 4815.

[184] F. Martinon, A. Mayor, J. Tschopp, "*The Inflammasomes: Guardians of the Body*", in *Annu. Rev. Immunol.*, Annual Reviews, Palo Alto, **2009**, *27*, 229.
[185] G. Chen, M. H. Shaw, Y.-G. Kim, G. Nuñez, "*NOD-Like Receptors: Role in Innate Immunity and Inflammatory Disease*", in *Annu. Rev. Pathol. Mech. Dis.*, Annual Reviews, Palo Alto, **2009**, *4*, 365.
[186] N. Y. Babaeva, N. Ning, D. B. Graves, M. J. Kushner, *J. Phys. D: Appl. Phys.* **2012**, *45*, 115203.
[187] N. Laegreid, G. K. Wehner, *J. Appl. Phys.* **1961**, *32*, 365.
[188] D. McKeown, *Rev. Sci. Instrum.* **1961**, *32*, 133.
[189] N. Matsunami, Y. Yamamura, Y. Itikawa, N. Itoh, Y. Kazumata, S. Miyagawa, K. Morita, R. Shimizu, H. Tawara, *Atom. Data Nucl. Data* **1984**, *31*, 1.
[190] M. J. Traylor, M. J. Pavlovich, S. Karim, P. Hait, Y. Sakiyama, D. S. Clark, D. B. Graves, *J. Phys. D: Appl. Phys.* **2011**, *44*, 472001.
[191] Y. Sakiyama, D. B. Graves, H.-W. Chang, T. Shimizu, G. E. Morfill, *J. Phys. D: Appl. Phys.* **2012**, *45*, 425201.
[192] T. Shimizu, Y. Sakiyama, D. B. Graves, J. L. Zimmermann, G. E. Morfill, *New J. Phys.* **2012**, *14*, 103028.
[193] M. J. Pavlovich, H.-W. Chang, Y. Sakiyama, D. S. Clark, D. B. Graves, *(submitted).*
[194] V. N. Bochkov, N. Leitinger, *J. Mol. Med.* **2003**, *81*, 613.
[195] K. C. Huth, B. Saugel, F. M. Jakob, C. Cappello, M. Quirling, E. Paschos, K. Ern, R. Hickel, K. Brand, *J. Dent. Res.* **2007**, *86*, 451.